University of California
Santa Barbara

Large Scale Simulations and Stochastic Modeling of Interfacial Transport Processes

A dissertation submitted in partial satisfaction
of the requirements for the degree

Doctor of Philosophy
in
Mechanical Engineering

by

Pouria Akbari Mistani

Committee in charge:

Professor Frederic G. Gibou, Chair
Professor Linda Petzold
Professor Jeff Moehlis
Professor Paolo Luzzatto-Fegiz

December 2020

The Dissertation of Pouria Akbari Mistani is approved.

Professor Linda Petzold

Professor Jeff Moehlis

Professor Paolo Luzzatto-Fegiz

Professor Frederic G. Gibou, Committee Chair

December 2020

Large Scale Simulations and Stochastic Modeling of Interfacial Transport Processes

by

Pouria Akbari Mistani

To My Parents, Sina, & Samira

Acknowledgements

I was immensely fortunate to cross paths with so many wonderful people without whom I would have never been able to complete my research, and go this far into my doctorate studies. Foremost, I would like to thank my advisor, Prof. Frederic G. Gibou, for his continuous support, motivations, patience, and guidance throughout my research. I am eternally grateful for trusting me with a new opportunity to resume the dreams for which I came to this country. I wish to thank the members of my PhD committee: Linda Petzold, Jeff Moehlis, and Paolo Luzzatto-Fegiz, for generously offering their time, support and guidance throughout preparation and review of this document. I would also like to sincerely thank my loving wife, Samira, who patiently put up with my preoccupation with this research for the past years, and always provided me with her counsel and support. Samira, you have lit up my life with your compassion and love, and always showed me a better perspective on every problem both in research and in life. I wouldn't have been here was it not for all the sacrifices that my parents, Sharifeh and Hassanali, and my brother, Sina, have made throughout my life. Specially during the past seven years that I have dearly missed every second of their presence. Sina, you were the first to trigger my curiosity for knowledge and patiently taught me the principles of scientific thinking. I still treasure the memory of the multiplication chart you made for me in our childhood, this dissertation is indeed my reflection on seeds of scholarship that you planted in my mind. I would also like to thank all my dear friends who have always supported me in this endeavor. Specially I would like to sincerely thank Soroush and Elaina, who have always supported me with their incredible kindness. Mojtaba and Hadi, thank you for always patiently listening to me and being there for me. Saber, Hamed, Behzad and Ghazaleh, you guys have made Santa Barbara the highlight of my life.

Curriculum Vitæ

Pouria Akbari Mistani

Education

2020	Ph.D. in Mechanical Engineering (Expected), University of California, Santa Barbara, USA.
2014	M.S. in Physics, University of California, Riverside, USA.
2013	B.S. in Physics, Sharif University of Technology, Tehran, Iran.
2013	B.S. in Aerospace Engineering, Sharif University of Technology, Tehran, Iran.

Publications

- **Journal papers:**
  1. **P Mistani**, A Guittet, D Bochkov, J Schneider, D Margetis, C Ratsch, F Gibou The island dynamics model on parallel quadtree grids. Journal of Computational Physics, 2018 May 15; 361:150-166 [1].
  2. **P Mistani**, A Guittet, C Poignard and F Gibou. A parallel Voronoi-based approach for mesoscale simulations of cell aggregate electropermeabilization Journal of Computational Physics, 2019 Mar 1;380:48-64 [2].
  3. **P Mistani**, S Pakravan, F Gibou. A fractional stochastic theory for interfacial polarization of cell aggregates, arXiv preprint arXiv:2008.11819, 2020 (under review) [3].
  4. S Pakravan , **P Mistani** , MA Aragon-Calvo, F Gibou. Solving inverse-PDE problems with physics-aware neural networks, arXiv preprint arXiv:2001.03608, 2020 (under review) [4]
- **Book chapters:**
  1. **P Mistani**, S Pakravan, F Gibou. Towards a tensor network representation of complex systems, Sustainable Interdependent Networks II, Springer International Publishing 2019 [5].
  2. **P Mistani**, S Pakravan, F Gibou. Tensor network renormalization as an ultra-calculus for complex system dynamics, Sustainable Interdependent Networks II, Springer International Publishing 2019 [6].

Abstract

Large Scale Simulations and Stochastic Modeling of Interfacial Transport Processes

by

Pouria Akbari Mistani

Continuum formulation of interfacial transport phenomena views interfaces as sharp 2D surfaces separating contiguous 3D bulk phases. In this view, interfacial processes are described by phenomenological models for the underlying microscopic processes or in analogy to conservation/constitutive laws that regulate transport in surrounding bulk phases. Mathematically, these surfaces act as boundary conditions for the governing partial differential transport equations in the bulk and determine discontinuities in solution of the bulk phase as well as the solution gradient across the interfaces. From a computational perspective, accurate numerical solution of these equations poses several algorithmic and computational challenges that require application of advanced numerical algorithms as well as high performance computing techniques. In the first part of my dissertation I will present our design and implementation of two parallel simulation engines based on the level-set method and using finite difference and finite volume discretization techniques on adaptive Voronoi and Cartesian (Quad-/Oc-tree) grids. These simulations are capable to realize large enough computational domains at high resolutions that allow for realization of mound formation phenomenon in epitaxial growth of materials systems, as well as detailed membrane permeabilization statistics emerging in electroporation of multicellular systems. In the second part of my dissertation, I will derive a general reduced-order state-space mathematical model for dynamics of probability density of interfacial polarizations in heterogeneous systems and compare its predictions with that of my direct numerical simulations.

Contents

Chapter 1

Introduction

Transport processes across sharp interfaces occur in many physical systems such as colloids and multicellular systems. Interfacial transport phenomena are usually concerned with transport of momentum, mass, chemical species, energy, or electric current across interfaces that separate bulk phases. In this dissertation I will focus on numerical simulations of: (i) epitaxial growth as an example of transport of mass across atomic island boundaries in the growth of thin films; and (ii) electroporation of cell aggregates that is an example of transport of electric current across cell membranes.

An interesting aspect of these systems is the novel macroscopic properties that arise when a large enough number of these interfaces are in play. For example, in the electroporation experiments of large cell aggregates it has been experimentally observed that relaxation behavior of the aggregate after switching off an applied electric pulse does not follow the same exponential profile that is expected from the physics of individual cells. Another interesting example is in epitaxial growth of atomic systems, in which during atomic depositions novel morphological modalities such as mounds, step edges and terraces arise.

Besides their pure scientific attractions, these macroscopic behaviors offer new oppor-

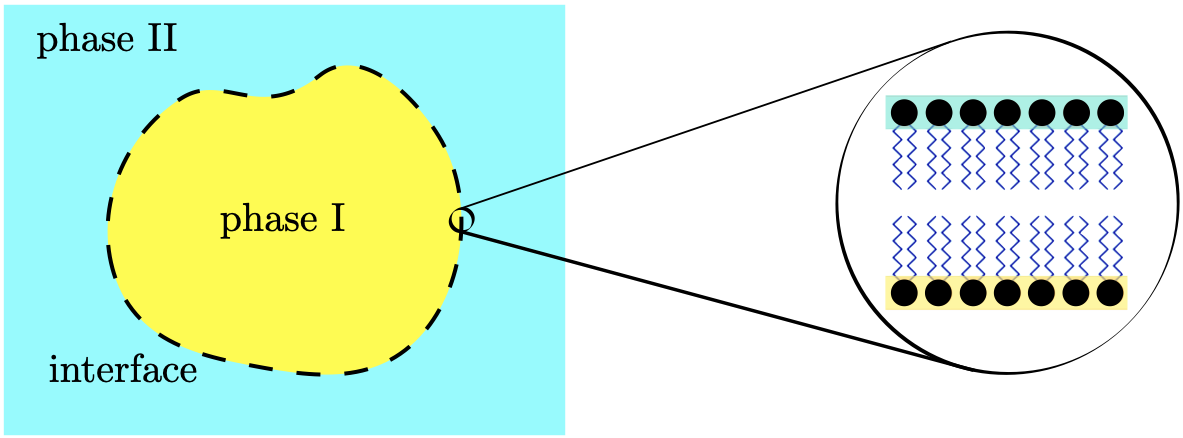

Figure 1.1: *Interfaces are modeled as 2D idealizations that separate different bulk phases. The subgrid physics is captured by multiscale continuum models that act as boundary conditions for the contiguous bulk phases.*

tunities for technological applications and medical treatments. For example, a curious observation has been made in the experiments with cell aggregate electroporation that showed the degree of deviation from an exponential relaxation correlates with healthy or unhealthy state of a tissue, besides its numerous applications in medicine such as electrochemotherapy, gene electro-transfer and DNA vaccination. Or in the case of epitaxial growth, it is the growth of mounds that degrades electric properties of many transformative devices such as transistors. On the other hand, these effects could enable new inventions and treatments, such as making quantum dots with leveraging these mounds, or the advent of electrochemotherapy as a novel treatment for cancer in sensitive organs where direct medical interference is prohibitively dangerous.

The common feature among these phenomena is the large spatiotemporal scales of the system, which incurs severe computational challenges. For example mound formation is a property of large substrates that only becomes relevant for manufacturing of optoelectronic devices when considered at lengthscales of a few microns, and timescales

of several seconds to minutes. Moreover, the anomalous relaxation is observed in large cell aggregates that are composed of tens of thousands of cells, indicating lengthscales of a few millimeters and timescales of a few microseconds. The challenge stems from the fact that underlying physical processes that drive these phenomena at large scales occur at much smaller spatiotemporal scales. For example, the atomistic random walks happen at few Angstroms and microseconds, or restructuring of the lipid bilayer also occurs over a few Angstroms and nano-seconds.

In this dissertation I will propose two computational frameworks for developing large scale numerical simulations that can realize relevant macroscopic features in interfacial transport problems. Here two main ingredients are employed to circumvent the computational challenges: (i) using multiscale mathematical models on one hand, and (ii) efficient numerical methods along with high performance computing algorithms on the other hand.

Multiscale models are incorporated throughout this thesis that view interfaces as idealized sharp surfaces across which discontinuities occur, and their role is to impose boundary conditions for the adjacent bulk phases which are described using continuum models, see figure 1. These boundary conditions are themselves multi-scale models for the underlying atomistic processes that in the case of epitaxial growth capture quantum mechanical effects at the boundary of atomic islands via Ehrlich-Schwoebel boundary condition whose parameters remain constant irrespective of the solution of the continuum model. However in the case of electroporation, cell membranes undergo internal restructuring whose effect is considered by a phenomenological model that depends on the instantaneous solution field at the aggregate level via a nonlinear model.

The numerical algorithms employed in this work are particularly suited for massively parallel simulations owing to their compact stencils, adaptive mesh refinement, proper grid partitioning using Z-ordering that ensures contiguous partitions on each processor

and subsequently keeps inter-processor communications at a minimum. These simulation frameworks benefit from state-of-the-art algorithms and high performance computing libraries that ensure scalability of our simulations well beyond thousands of processors on national supercomputers.

Unfortunately, it has been increasingly evident that developing large scale numerical simulations alone is not enough for gaining new understanding into complex physical systems. This is partly because the number of physical parameters and possible configurations of large scale complex systems is so vast that makes any attempt at sweeping the corresponding parameter space futile. Moreover, from a practical standpoint the computational costs needed for a single run of such a simulation could easily surpass Terabytes of data and tens of thousands of CPU-hours of computations even using the most advanced national supercomputers. Computational science poses a third style for scientific inquiry into complex physical systems with the utmost purpose of drawing new insights on the nature of complex systems. As such, it is inevitable that the task of a computational scientist is to carry over the reduction of models based on a reasonably small number of simulations in a principled fashion. In the author's opinion, the only justifiable reasoning behind developing such expensive numerical simulations is discovery of accurate enough but efficient enough reduced-order models at the level of a system of ordinary differential equations, or effective constituitve relations, that could describe macroscopic observables of interest in an extremely efficient fashion. It is in this spirit that in the last chapter of my dissertation I turn my focus on a general purpose modeling framework that is particularly suited for theorizing reduced-order models from large scale simulation data. I apply this framework to the case of cell aggregate electroporation and demonstrate its utility and efficiency for future simulation-based modelers who have access to detailed distributions of state variables of their system of interest.

1.1 Permissions and Attributions

1. The content of chapter 2 is the result of a collaboration with Arthur Guittet, Daniil Bochkov, Joshua Schneider, Dionisios Margetis, Christian Ratsch, and Frederic Gibou, and has previously appeared in the Journal of Computational Physics [1]. It is reproduced here with the permission of Elsevier: `https://www.sciencedirect.com/science/article/pii/S0021999118300767`.

2. The content of chapter 3 is the result of a collaboration with Arthur Guittet, Clair Poignard, and Frederic Gibou, and has previously appeared in the Journal of Computational Physics [2]. It is reproduced here with the permission of Elsevier: `https://www.sciencedirect.com/science/article/pii/S0021999118308052`.

3. The content of chapter 4 is the result of a collaboration with Samira Pakravan and Frederic Gibou, and has previously appeared on *arXiv*. It is reproduced here with the permission of *arXiv* [3]: `https://arxiv.org/abs/2008.11819`.

Chapter 2

Large scale simulations of epitaxial growth

2.1 abstract

We introduce an approach for simulating epitaxial growth by use of an island dynamics model on a forest of quadtree grids, and in a parallel environment. To this end, we use a parallel framework introduced in the context of the level-set method. This framework utilizes: discretizations that achieve a second-order accurate level-set method on non-graded adaptive Cartesian grids for solving the associated free boundary value problem for surface diffusion; and an established library for the partitioning of the grid. We consider the cases with: irreversible aggregation, which amounts to applying Dirichlet boundary conditions at the island boundary; and an asymmetric (Ehrlich-Schwoebel) energy barrier for attachment/detachment of atoms at the island boundary, which entails the use of a Robin boundary condition. We provide the scaling analyses performed on the Stampede supercomputer and numerical examples that illustrate the capability of our methodology to efficiently simulate different aspects of epitaxial growth. The combination

of adaptivity and parallelism in our approach enables simulations that are several orders of magnitude faster than those reported in the recent literature and, thus, provides a viable framework for the systematic study of mound formation on crystal surfaces.

2.2 Introduction

Epitaxial growth is a complex, multiscale process in which a material is deposited on top of another one and takes on the crystalline orientation of the substrate. The growth process results in the formation and evolution of islands and steps [7, 8], which accompany the fabrication of many modern opto-electronic devices below the roughening transition. Hence, epitaxial growth is of fundamental technological importance. Notable examples of related devices include transistors in microelectronics, quantum dots for photonic-crystal lasers, quantum dot-based enhancements in the energy sector, and devices for nonvolatile storage which is sought to replace hard drives, flash and RAM memories. Other applications of epitaxial growth include catalysts, which are used, e.g., in the energy sector, food processing, and environmental science.

In this paper, we introduce a computational approach for the simulation of island evolution in large epitaxial systems. Our main motivation is the need to make accurate predictions for the formation of crystal surface features, e.g. mounds, at large scales. We start with the island dynamics model (IDM) by Caflisch *et al.* [11, 12]. This description relies on the formulation of a free boundary value problem, in the spirit of the Burton-Cabrera-Frank (BCF) theory [13]. The model has the following main elements: (i) a diffusion-type equation for the density of adsorbed atoms (adatoms) in the region (terrace) between successive steps, which includes nucleation in a mean-field sense; (ii) Dirichlet or Robin boundary conditions for the adatom density at the island boundaries;

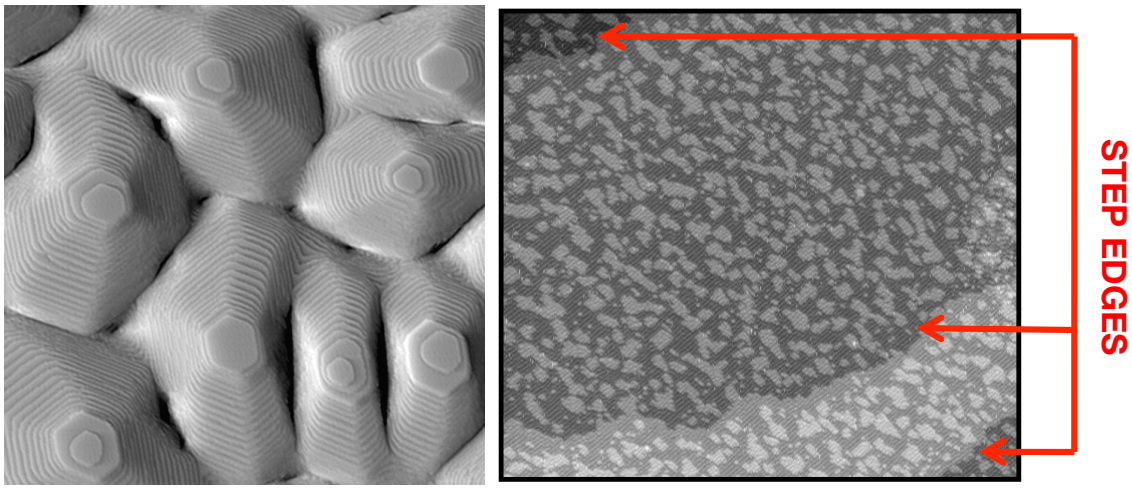

Figure 2.1: *Single-Tunneling-Microscope (STM) images of epitaxially grown thin films where macroscopic or mesoscale features may develop, e.g., mounds (left image from [9]) and step edges (right image from [10]).*

and (iii) a kinetic law for the normal velocity of each boundary by mass conservation. We numerically solve this system on a forest of quadtree grids, and in a parallel environment by using the framework introduced in the context of the level-set method by Mirzadeh *et al.* [14]. This framework utilizes the discretizations of Min and Gibou [15] for the associated free boundary value problem, and the `p4est` library of Burstedde *et al.* [16] for the partitioning of the grid. We apply our approach to the growth of mounds in *homoepitaxy*, where the deposited material is the same as the substrate.

From a physical viewpoint, basic processes that occur during epitaxial growth include the nucleation, growth, and coalescence of two-dimensional islands. Close to thermodynamic equilibrium, homoepitaxial growth proceeds atomic layer by atomic layer. However, growth is far from equilibrium for many homoepitaxial systems, and, therefore, the observed surface morphology is a result of kinetic limitations. In particular, multilayer growth may become unstable and, hence, mounds may form. This phenomenon has been observed experimentally for many epitaxial systems such as surfaces of Cu [17, 18], Fe [19], Ag [20] or Pt [21].

The microscopic process that usually underlies mound formation is an additional (Ehrlich-Schwoebel, ES) energy barrier characterizing the attachment/detachment of atoms at island boundaries or edges of steps [22, 23]. For some applications, these mounds can seriously degrade the performance of the device being grown; for example, in the case of metallic films the electric connections between layers can be hampered [24]. In contrast, in some other cases these mounds can be regarded as almost zero-dimensional defects with novel properties that can be exploited in the laboratory setting [25]. An example of such mounds which form for growth of Pt on Pt(111) is shown in Figure 2.1 [left panel]. In the suitable kinetic regime of these systems, step edges with interesting dynamics are evident (see Figure 2.1 [right panel]).

Hence, the understanding and control of crystal surface instabilities that lead to mound formation are significant goals in materials science. Accordingly, the development of computational methods that accurately and efficiently describe the growth of thin films has been the focus of intensive research [26, 27, 28, 29]. Computational challenges in this direction are primarily due to the multiscale nature of epitaxial growth: On the one hand, growth of islands and the flow of steps is determined by the diffusion (and attachment) of individual adatoms, which sets time and length scales of the order of 10^{-6} sec and Ångstroms. On the other hand, typical devices can be microns in lateral size (and hundreds of layers thick), and are grown at timescales that are seconds or minutes.

To develop a computational approach faithful to the multiscale character of epitaxial growth, we use the IDM and a level-set method for its simulation [11, 30, 31, 32, 33, 34, 12]. The model has the mesoscale features of the BCF theory for steps [13], namely, coarse-graining of the atomistic dynamics in the lateral (parallel to a fixed reference plane) directions and retainment of atomistic detail in the growth direction; thus, the model is particularly well-suited for simulating epitaxial growth. Yet, this model has so far only used uniform grids on sequential machines.

In the present paper, we overcome this limitation via an approach that uses adaptive mesh refinement techniques and parallel strategies to significantly increase the size of systems that can be considered, as well as to offer a significant simulation speedup. To validate our computational approach, we carry out a series of numerical experiments associated with mound formation. In these examples, we invoke irreversible aggregation, which corresponds to a Dirichlet condition in the IDM; and an ES barrier which is modeled through a Robin condition at the step edge.

Section 2.3 provides an overview of the IDM (Section 2.3.1), and describes the multi-level-set representation for the motion of island boundaries (Section 2.3.2). Section 3.4 details the parallel strategy and the discretization algorithms for the simulation of multi-layer growth and dynamics of step edges. In Section 3.5 we present numerical examples that serve the validation of our computational approach. Section 3.7 concludes our paper with a summary of our framework and an outline of related, open problems.

2.3 Island dynamics model and multi-level-set representation

In this section, we review the basic elements of the IDM, which forms an extension of the BCF theory [13]; see also [35, 7]. Furthermore, we describe a level-set approach that simultaneously keeps track of the motion of many island boundaries.

2.3.1 Island dynamics model

The IDM [11, 30, 31, 32, 33, 34, 12] treats the evolution of islands and steps as a free boundary problem: each boundary moves by mass conservation, in the spirit of the BCF

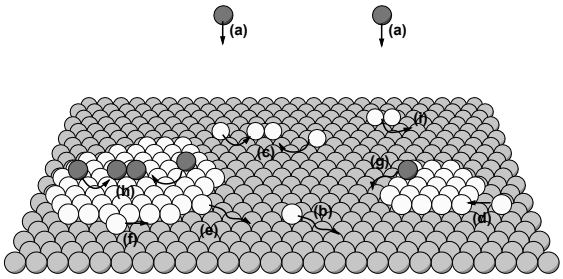

Figure 2.2: *Schematic of atomistic processes during epitaxial growth. Atoms are deposited onto the surface [(a)]; diffuse on the surface with atomistic (hopping) rate D [(b)]; attach to [(d)], or detach from [(e)] an island boundary or a step edge ; or diffuse along an island edge [(f)]. In addition to these processes, two atoms may coalesce and form a dimer [(c), (h)], which might be stable and grow, or break up [(i)].*

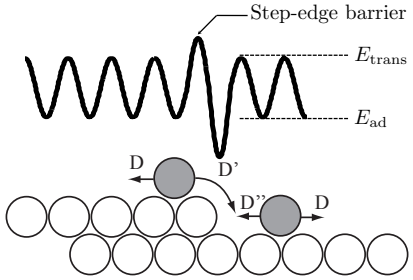

Figure 2.3: *Schematic of an asymmetric (ES) step-edge barrier. The lower panel shows the atomistic configuration of a step edge, to which an adatom attaches with rate D' (D'') from the upper (lower) terrace. The upper panel depicts the corresponding energy landscape in one spatial coordinate.*

model [13]. Island boundaries and step edges have an atomic height, a, thus retaining the lattice discreteness in the vertical direction. In contrast, the diffusion of adatoms on each terrace is considered as a continuous process by coarse-graining of the atom hopping. Hence, adatom diffusion is studied via the dynamics of the adatom density, $\rho(\mathbf{x}, t)$, a continuous variable.

Specifically, $\rho(\mathbf{x}, t)$ evolves through the equation

$$\frac{\partial \rho}{\partial t} = F + \nabla \cdot (\mathcal{D} \nabla \rho) - 2\frac{dN}{dt} \ , \tag{2.1}$$

which accounts for adatom diffusion with diffusivity $\mathcal{D} = Da^2$ (where D is the hopping rate), external material deposition with flux F, and nucleation of islands with rate dN/dt where $N(t)$ is the island density (see Figure 2.2). In the following analysis, we set the lattice spacing, a, or step height, equal to unity, $a = 1$; thus, we replace $\mathcal{D}$ by D.

By use of a mean-field approximation, the nucleation rate dN/dt is defined by

$$\frac{dN}{dt} = \sigma_1 D \langle \rho^2(\mathbf{x}) \rangle \ , \tag{2.2}$$

where σ_1 is a capture number [36, 37] and $\langle \cdot \rangle$ denotes the average taken over all lattice sites. Note that the capture number, σ_1, is a phenomenological, effective parameter that expresses how effectively an island of given size in a given environment (i.e., with a given capture area) competes for the available monomers on the crystal surface [36]. Stochastic elements for island nucleation have been added to the IDM, and validated by comparison to an (atomistic) kinetic Monte Carlo (KMC) model [31].

A few additional comments on (2.2) are in order. This equation dictates when the adatom density is large enough to seed a new island. The location of nucleation takes into account the stochasticity inherent to atomistic dynamics, as described in [31]. From a computational/algorithmic perspective, this description of nucleation can be split into the following stages:

1. Compute ρ^2 at each grid point (label them $i = 1, \cdots, n$), weighted by its surrounding computational cell area $w(\boldsymbol{x}_k)$.

2. Compute the sum over all these values, keeping partial sums $Q_k = \sum_{i=1}^{k} w(\boldsymbol{x}_k) \times \rho^2(\boldsymbol{x}_k)$.

3. Generate a random number, r in $[0, Q_n]$.

4. Find the first index k such that $r >= Q_k$.

5. Seed a circular island of size 2 Δx at $\boldsymbol{x}_k$.

The diffusion equation (2.1) for the adatom density, ρ, must be supplemented with boundary conditions at island boundaries or step edges. The boundary conditions for ρ reflect important atomistic processes and, thus, have a crucial impact on the ability of the IDM to make physical predictions. In general, a Robin condition for ρ at the island boundary has been extensively invoked in epitaxial systems [35, 38, 7]. In regard to the upper terrace (see Figure 2.3), this condition assumes the form

$$\nabla\rho \cdot \boldsymbol{n} + \frac{D'}{D - D'}\rho = \frac{D'}{D - D'}\rho_{\text{eq}} \ , \tag{2.3}$$

where ρ and $\nabla\rho$ are restricted to the island boundary, the atomistic rate D' expresses the energy barrier for adatom diffusion over a step edge or island boundary, ρ_{eq} is an equilibrium adatom density, and $\boldsymbol{n}$ is the outward normal to the island boundary.

Boundary condition (2.3) describes the effect of the ES barrier (for $D' \neq D$), and has been formally derived from atomistic dynamics [39]. Note that an ES barrier causes any atom located next to the step edge to be more likely to diffuse to the adjacent site on the same terrace (with rate D) than diffuse downwards (with rate D'). Similarly, an additional energy barrier, expressed by rate D'', may be present on the lower terrace (see Figure 2.2 [right panel]). Physically, this additional step-edge barrier causes an uphill current and the formation of mounds, as shown both by continuum models [38] and KMC simulations [40].

As $D' \to D$, equation (2.3) reduces to the Dirichlet condition $\rho(\mathbf{x}) = \rho_{\text{eq}}$ [13, 8, 39]. Notably, in [41], an expression for ρ_{eq} is derived with no step-edge (ES) barrier; while in [42], the authors derive and implement an expression for ρ_{eq} under a step-edge barrier. In principle, this ρ_{eq} depends on the microscopic rates for detachment and edge diffusion [11].

Equations (2.1)–(2.3) need to be complemented with a velocity law for the motion of the free boundary. Specifically, the normal velocity field, $\boldsymbol{v}$, that characterizes the motion of the island boundary is computed by adatom mass conservation according to the equation

$$\boldsymbol{v} = \left(D^{-} \frac{\partial \rho^{-}}{\partial \boldsymbol{n}} - D^{+} \frac{\partial \rho^{+}}{\partial \boldsymbol{n}} \right) \boldsymbol{n} \ , \tag{2.4}$$

which accounts for the total mass flux toward the boundary from the upper (+) and lower (−) terrace. This equation can be enriched with a term that expresses step-edge diffusion [43]. This extension lies beyond our present scope. Equations (2.1)–(2.4) form the core of the IDM.

2.3.2 Multi level-set representation of island dynamics

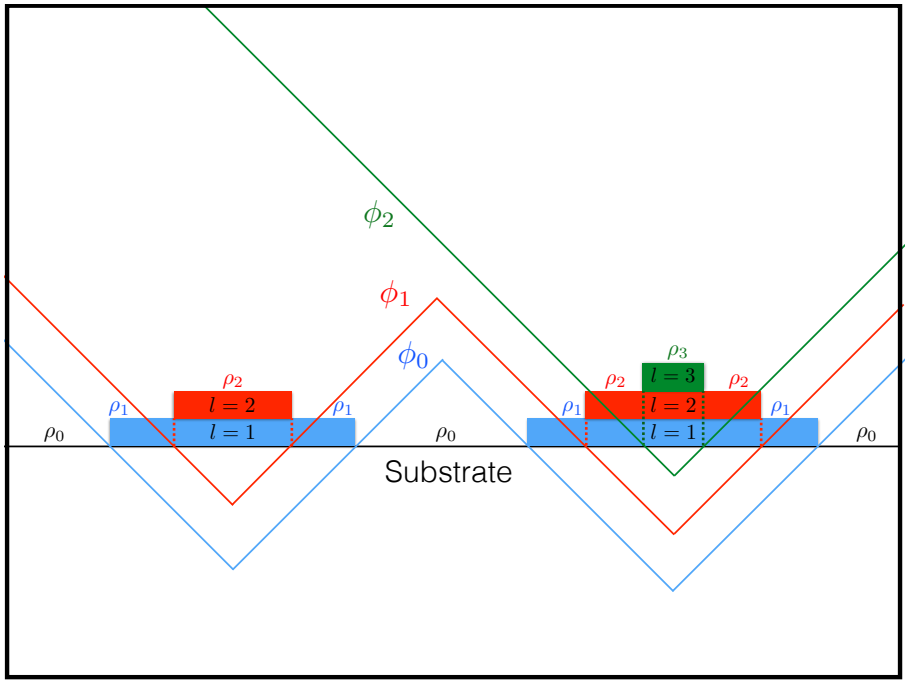

Figure 2.4: *Level-set representation of the IDM in the present framework. The zero-level set of ϕ_l represents the boundary of islands of height l onto which the adatom density is described by ρ_l.*

Next, we describe a multi-level-set representation of the IDM that is best suited to our main purpose of simulating the evolution of large epitaxial systems in this paper. The desired representation exploits the free-boundary approach inherent to the IDM (Section 2.3.1), as explained below.

First, we emphasize that the IDM is numerically resolved by use of the level-set method, introduced in [44], to keep track of the motion of the island boundaries. The level-set method represents an arbitrary contour as $\Gamma = \{\boldsymbol{x} \in \mathbb{R}^n \,|\, \phi(\boldsymbol{x}) = 0\}$, where $\phi(\boldsymbol{x})$ is a Lipschitz continuous function. The region enclosed in Γ and the region outside Γ are defined as $\{\boldsymbol{x} \in \mathbb{R}^n \,|\, \phi(\boldsymbol{x}) < 0\}$ and $\{\boldsymbol{x} \in \mathbb{R}^n \,|\, \phi(\boldsymbol{x}) > 0\}$, respectively. In the IDM described in [11, 30, 12], the boundary of islands of height l is described as $\Gamma_l = \{\mathbf{x} : \phi(\mathbf{x}) = l\}$. In the present work, the boundary of islands of height l is described by the *zero* level-set of a level-set function ϕ_l as depicted in Figure 2.4, i.e. we use as many level-set functions as the number of atomic layers, with each level-set function ϕ_l "recycled" when it represents a complete layer.

The rationale for applying this formalism and, thus, for choosing not to represent all the layers with a single level-set function, can be outlined as follows: (i) Our choice enables the reinitialization of the level-set functions, which in turn increases mass conservation [45, 46, 15]; and (ii) the motion of the boundaries at different islands' height can be processed independently, which increases computational efficiency. Specifically, in this multi-level-set framework, the region occupied by the island of height l is defined as $\Omega_l = \{\boldsymbol{x} \mid \phi_l(\boldsymbol{x}) > 0 \text{ and } \phi_{l-1}(\boldsymbol{x}) < 0\}$. If an island is the top most, then $\Omega_l = \{\boldsymbol{x} \mid \phi_{l-1}(\boldsymbol{x}) < 0\}$. The substrate is defined as $\Omega_0 = \{\boldsymbol{x} \mid \phi_0(\boldsymbol{x}) > 0\}$.

In this vein, the variable ρ_l describes the adatom density on islands of height l (see Figure 2.4). Accordingly, boundary conditions for ρ_l in the form of (2.3) are imposed on the set where $\phi_l = 0$ and also $\phi_{l-1} = 0$ if $l > 0$. Once the velocity field $\boldsymbol{v}_l$ describing the

dynamics of the islands of height l is computed, ϕ_l evolves according to the equation

$$\frac{\partial \phi_l}{\partial t} + \boldsymbol{v}_l \cdot \nabla \phi_l = 0 \ ; \tag{2.5}$$

cf. step velocity law (2.4). In order to transform an arbitrary level-set function ϕ_l^0 into a signed distance function ϕ_l, we solve the reinitialization equation [45]

$$\frac{\partial \phi_l}{\partial \tau} + \mathtt{sign}(\phi_l^0)\,(|\nabla \phi_l| - 1) = 0 \ , \tag{2.6}$$

where τ is a fictitious time and `sign` refers to the signum function.

2.4 Parallel strategy on adaptive Quadtree grids

The numerical implementation of the IDM has so far only considered uniform grids. This approach causes limitations in applications to systems with many islands and steps. Specifically, in the case where one aims to simulate multi-layer growth or examine the dynamics of step edges, uniform grids are limited in their ability to consider large systems because of memory constraints and/or slow speed of simulations. In this section, we introduce a parallel strategy on adaptive grids that enables efficient simulations of the IDM and resolve island dynamics in large epitaxial systems. This strategy makes use of recent computational advances in adaptive mesh refinement.

We add a few comments on these advances. In particular, Chen *et al.* [47] introduced discretizations for solving the diffusion equation in irregular domains by using Quadtree grids. Min and Gibou [15] introduced discretizations on Quadtree grids for free boundary problems using the level-set method. These two approaches were combined to solve the Stefan problem in [48]. Using this framework and the work of Papac *et al.* [42] (see also [49]), Papac *et al.* [50] derived a scheme to solve the Stefan problem with Robin boundary

conditions on Quadtree grids and briefly considered the application of this scheme to the IDM. In [14], Mirzadeh *et al.* developed the level-set technology on Quadtree/Octree grids in the context of distributed computations using the discretizations of Min and Gibou [15] and the `p4est` library of Burstedde *et al.* [16].

In the remainder of this section, we will describe the computational framework (sections 2.4.1 - 2.4.3) and how it can be used for the two cases where we have a Dirichlet boundary condition (which corresponds to the case without a step-edge barrier); and when we have a Robin boundary condition, which is needed when a step-edge barrier is present (sections 2.4.4-2.4.6).

2.4.1 Quadtree data structure and refinement criterion

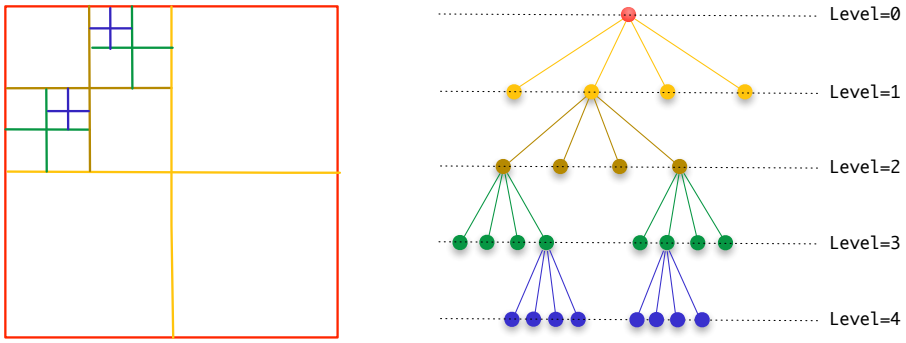

Figure 2.5: *(Color online) Discretization of a two-dimensional domain (left) and its quadtree representation (right). The entire domain corresponds to the root of the tree (level 0). Each cell can then be recursively subdivided further into four children. In this example, the tree is non-graded, since the difference of level between some adjacent cells exceeds one.*

Quadtrees are standard data structures that have been first introduced in the context of computer graphics. The interested reader is referred to the excellent books by Samet for more details [51, 52]. Referring to Figure 2.5, we associate the entire computational cell with the root of a quadtree structure. Subsequently, cells are recursively split into

four children of equal size according to a refinement criterion and until the limits set for the smallest and largest cells are reached. We define the level of the root cell to be 0 and increment it by 1 for its children. In particular, we will call a $(l_{\min}, l_{\max})$-grid, an adaptive grid sampling a computational domain of size $L \times L$ for which the smallest cells have size $L \times 2^{-l_{\max}}$ and the largest cells have size $L \times 2^{-l_{\min}}$.

The two main equations of the IDM are parabolic equation (2.1), which describes the evolution of the adatom density, ρ, and level-set equations (2.5) and (2.6) which are used to represent the evolution of the island boundaries. In both cases, the information near the island boundaries is what drives the accuracy of the simulation. Indeed, the diffusion equation for the adatom density, ρ, is a parabolic equation and therefore produces smooth solutions in the entire domain, except near the boundary of each island. Specifically, boundary conditions applied on each side of the island boundary (upper and lower terraces) produce discontinuous solutions, ρ, and/or its gradient. Likewise, the evolution of the level-set functions ϕ_l is directly linked to the resolution near the island boundaries or step edges [15].

Hence, we use a refinement criterion that automatically sets the finest resolution near the zero-level set of each ϕ_l, i.e. we split a computational cell $\mathcal{C}$ if

$$\min_{v \in \text{vertices}(\mathcal{C})} |\phi_l(v)| \leq \text{Lip}(\phi_l) \cdot \text{diag-size}(\mathcal{C}) \ , \tag{2.7}$$

where diag-size($\mathcal{C}$) refers to the length of the diagonal of $\mathcal{C}$ and v refers to its vertex. Likewise, we merge with its parent cell, any cell $\mathcal{C}$ for which the following condition holds:

$$\min_{v \in \text{vertices}(\mathcal{C})} |\phi(v)| > \text{Lip}(\phi) \cdot \text{diag-size}(\mathcal{C}) \ . \tag{2.8}$$

The 'parameter' Lip(ϕ) in equations (3.6) and (2.8) controls how drastic the size difference between adjacent cells can be. In the present work, we take a value of Lip(ϕ) ≈ 1.1 to generate the grids depicted in Section 3.5.

2.4.2 Parallel framework

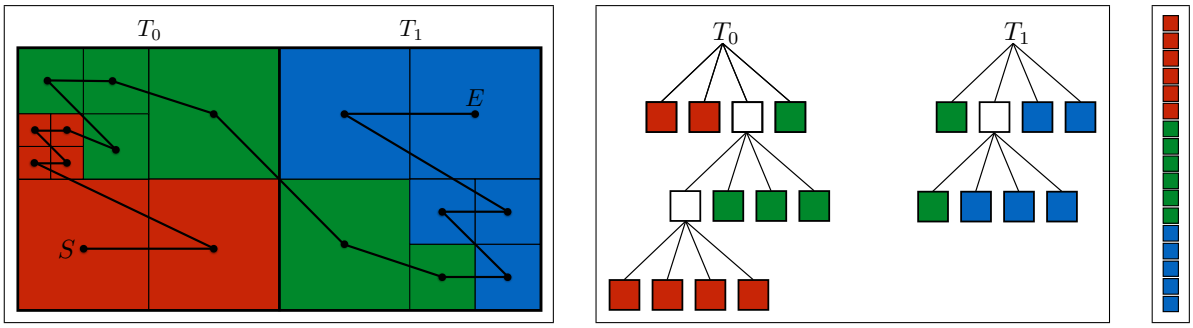

Figure 2.6: *Two trees, T_0 and T_1, constitute the 'forest'. The Z-ordering (left) of the Quadtree's leaves (center) is used to partition the data among the available processes (right). In this figure, the different colors correspond to different processor ranks. S represents the starting cell and E the last cell visited. In the* `p4est` *library, only the one-dimension array (right) is stored among the available processes.*

Next, we outline the main idea of the parallelism in our approach. The parallel framework that we use is the one introduced by Mirzadeh *et al.* [14]. This framework employs the `p4est` library for the partitioning of the grid and an algorithm that constructs local trees that enable the discretizations detailed in Sections 2.4.4 and 2.4.5. Additional parallel algorithms are constructed to number the islands on the surface in order to compute important statistics, as described in Section 2.4.3.

When considering parallel computation, where the communication of data between processes is orders of magnitude more time consuming than the computation itself, the main focus of algorithm design is to reduce the number of computations and/or hide the cost of communication by intertwining them with computation. Reducing communication

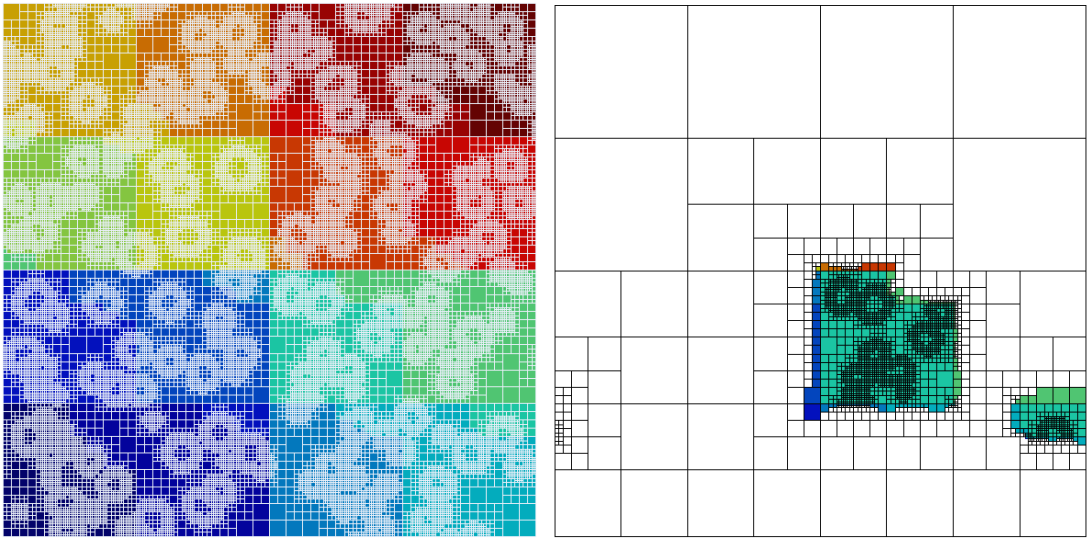

Figure 2.7: *Left (global forest refined close to the interface): an example of a computational grid partitioned among 16 processes (color-coded) and the global forest refined close to the interface. Right (quadtree local to the cyan processor): the local tree to one process refined to match local islands. Note the surrounding ghost layer from neighboring processes with different colors.*

is achieved by grouping, or partitioning, the data in the local memory of each process. The strategy of Burstedde *et al.* [16] is illustrated in Figure 2.6: (1) a macromesh of uniform cells is created and replicated on each process; (2) a forest of Quadtrees is created recursively using all processes and partitioned among them. The partitioning uses a Z-ordering of the Quadtree leaves, which are recorded in a one-dimensional array before being split equally among the available processes. The application of the Z-ordering clusters the data contiguously, as depicted in Figure 2.6, and thus subsequently minimizes the amount of communication during the discretization phase.

Since the `p4est` library only stores the one-dimensional array of the forest's leaves, an algorithm for constructing the local Quadtree on each process is used in order to apply the discretizations described below. The procedure introduced by Mirzadeh *et al.* [14] is to create a local tree in such a way that the levels of its leaves correspond to that of the one-dimensional array locally. Globally, the available processes represent the global

grid but only store their local portion plus data at points surrounding each processor, i.e. ghost layer, that is necessary to discretize the equations. The result of this process is illustrated in Figure 2.7. The adaptivity of the Quadtree to the formation of new islands is illustrated in Figure 2.8; it is refined close to the islands and coarsen elsewhere according to the refinement criteria.

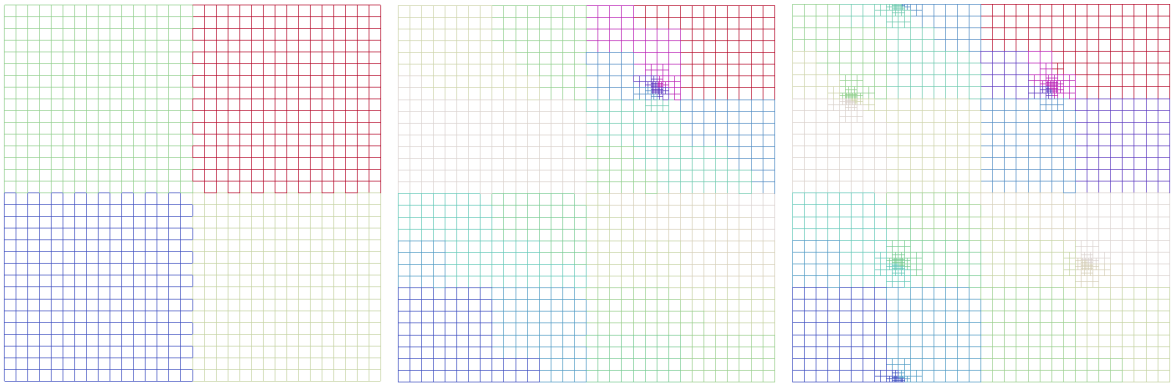

Figure 2.8: *Example of adaptive grids and partitioning at different computational times. Processors' rank are in color. Left: initial uniform grid. Middle: first seeding with adaptive grid. Right: five islands with adaptive grid.*

2.4.3 Numbering the islands

We now introduce an algorithm to compute the number of islands for a given level. This task is non-trivial because the islands can span multiple processes, as depicted in Figure 2.9.

The first step of our algorithm is for each process to number its local islands, with an offset. For the purpose of demonstration, we choose an offset equal to 10 (we choose an offset of 10^6 in practice), so that the islands of process p can be numbered from $10p$ to $10(p+1)-1$. In practice, any number greater than the maximum number of islands that a single process can have is suitable. The local island numbering is carried out by going through the local nodes. Such that for each non-numbered node with $\phi_l < 0$, assigning

a number to it and recursively assigning the same number to all the neighboring nodes that are part of the same island, i.e. that also have a negative ϕ_l value.

The next step is to construct a graph where each node represents a local island and two nodes are connected if the local islands are connected through the ghost layer that connects two processes. In order to build this graph, we must first communicate the number of local islands for each process and the island numbers of the points in the ghost layer. With this information, each process can build a graph containing all the global nodes and with the edges involving its local islands.

Finally, we gather the graph across all the processes, thus providing each process with the global graph connecting all the local islands across all the processes. Each process can then count the number of connected components of the graph and assign a unique global number to each component, which is the global island number.

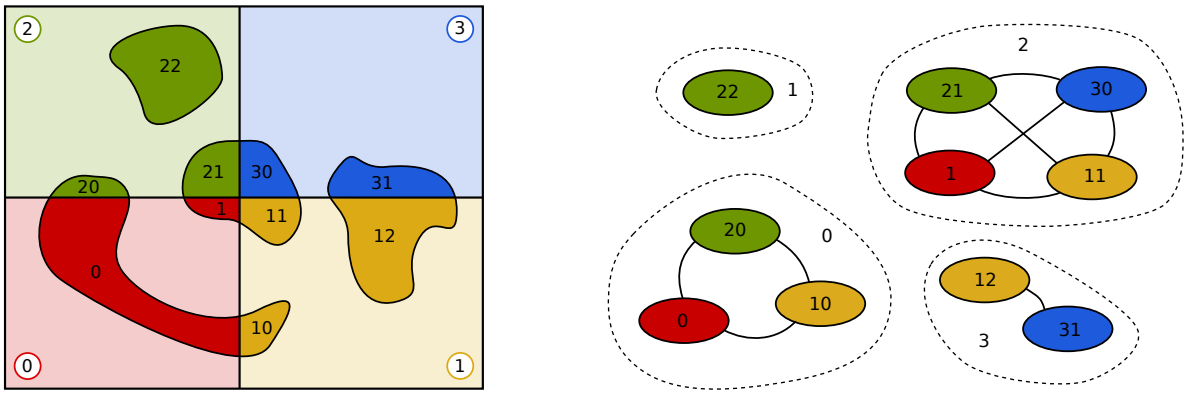

Figure 2.9: *Left: Four islands spread across four processes. Each process p has assigned a number to its local islands, with an offset equal to* $10p$*. Right: the global graph connecting the local islands. Each component of this graph is a unique global island.*

2.4.4 Solving for the adatom density

The adatom density ρ_l has to be solved on the corresponding terrace Ω_l with appropriate boundary conditions applied on the boundary of the terrace. By (2.1), on an

island of height l, the adatom density satisfies the equation

$$\frac{\partial \rho_l}{\partial t} = F + \nabla \cdot (D \nabla \rho_l) - 2\frac{dN}{dt} \ .$$

To solve this equation, we use a Crank-Nicholson scheme in time, writing

$$\frac{\rho^{n+1} - \rho^n}{\Delta t} = F + \frac{1}{2}\nabla \cdot (D \nabla \rho^{n+1}) + \frac{1}{2}\nabla \cdot (D \nabla \rho^n) - 2\frac{dN}{dt} \ , \tag{2.9}$$

where we have omitted the subscript l (i.e. $\rho = \rho_l$ in this section) and $\dfrac{dN}{dt} = \sigma_1 D \langle \rho^2(\mathbf{x}) \rangle$ is taken at time $t = t^n$; cf. (2.2). The discretizations of the terms of the form $\nabla \cdot (D \nabla \rho)$ depend on whether we consider a grid node adjacent to the interface or not, as illustrated in Figure 2.10.

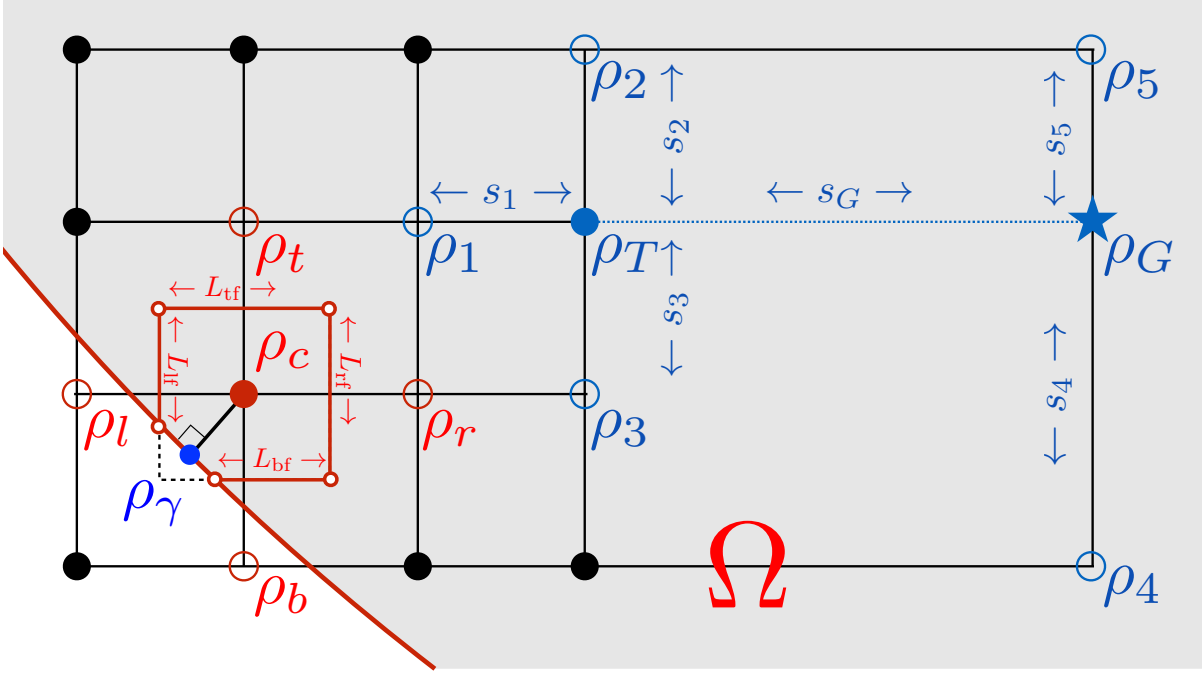

Figure 2.10: *Stencils used in the discretization of the adatom density. We use a finite volume approach for nodes that are adjacent to the islands' boundary* Γ *(where the grid is locally uniform) and a finite difference approach for the other nodes.*

Discretization far from the island boundaries

The difficulty in discretizing $\nabla \cdot (D\nabla\rho)$ at a grid node that is not near the island boundary comes from the potential presence of a T-junction configuration, i.e. the case where one grid node is missing in one of the Cartesian directions. In that case, Min *et al.* [53] derive a third-order accurate definition of a ghost value, ρ_G:

$$\rho_G = \frac{\rho_4 s_5 + \rho_4 s_4}{s_4 + s_5} - \frac{s_4 s_5}{s_2 + s_3}\left(\frac{\rho_2 - \rho_0}{s_2} + \frac{\rho_3 - \rho_0}{s_3}\right) ,$$

where s_i is the size of the segments depicted in Figure 2.10. This definition provides a way to discretize the Poisson operator, at the grid node T, as

$$\nabla \cdot (D\nabla\rho)_T = \frac{2}{s_G + s_1}\left(\frac{\rho_G - \rho_T}{s_G} - \frac{\rho_T - \rho_1}{s_1}\right).$$

From this definition, we fill the corresponding row of the linear system for the grid node T.

Discretization near the island boundaries

For grid nodes that are adjacent to the interface, the discretization must account for the boundary condition given by equation (2.3). Following Papac *et al.* [42], we consider the integration of the time discretization (2.9) in the dual cell $\mathcal{C}$ centered at the local grid node c (see figure 2.10), viz.,

$$\int_{\mathcal{C}\cap\Omega} \rho^{n+1} - \frac{\Delta t}{2}\nabla \cdot (D\nabla\rho^{n+1})\, d\Omega = \int_{\mathcal{C}\cap\Omega} \rho^n + \frac{\Delta t}{2}\nabla \cdot (D\nabla\rho^n) + \Delta t F - 2\Delta t \frac{dN}{dt}\, d\Omega ,$$

where Ω is the domain defined by the island of height l. By applying the divergence theorem on the diffusion terms, we obtain

$$\begin{aligned}\int_{\mathcal{C}\cap\Omega} \rho^{n+1}\, d\Omega - \frac{D\Delta t}{2}\int_{\partial(\mathcal{C}\cap\Omega)} \nabla\rho^{n+1}\cdot\boldsymbol{n}\, d\Gamma &= \int_{\mathcal{C}\cap\Omega} \rho^{n} + \Delta t\left(F - 2\frac{dN}{dt}\right) d\Omega \\ &+ \frac{D\Delta t}{2}\int_{\partial(\mathcal{C}\cap\Omega)} \nabla\rho^{n}\cdot\boldsymbol{n}\, d\Gamma\ ,\end{aligned}$$

where $\partial\left(\mathcal{C}\cap\Omega\right)$ refers to the boundary of $(\mathcal{C}\cap\Omega)$, i.e. the part of the computational cell that belongs to the island of height l. The boundary integrals are further split into two parts: the boundary of the computational cell $\mathcal{C}$ that belongs to the island of height l and the part of the island boundary that is located in $\mathcal{C}$:

$$\int_{\partial(\mathcal{C}\cap\Omega)} \nabla\rho^{n+1}\cdot\boldsymbol{n}\, d\Gamma = \int_{\partial\mathcal{C}\cap\Omega} \nabla\rho^{n+1}\cdot\boldsymbol{n}\, d\Gamma + \int_{\mathcal{C}\cap\partial\Omega}\left(\frac{D'}{D-D'}\rho_{eq} - \frac{D'}{D-D'}\rho\right) d\Gamma \quad (2.10)$$

In the above equation, we invoked Robin boundary condition (2.3) in the last term.

Next, we discuss the computation of the integrals on the right-hand side of (2.10). The integral of the unknown function ρ over the boundary $\mathcal{C}\cap\partial\Omega$ is approximated by the value of ρ at the point γ on the boundary (see figure 2.10) multiplied by the length of the boundary $\mathcal{C}\cap\partial\Omega$, i.e.

$$\int_{\mathcal{C}\cap\partial\Omega} \rho\, d\Gamma \approx \rho_\gamma \int_{\mathcal{C}\cap\partial\Omega} d\Gamma\ .$$

The point γ is defined as the intersection of the boundary and a straight line orthogonal to the boundary at γ and passing through the grid point c under consideration. At γ, the adatom density satisfies the Robin boundary condition (2.3). Moreover, ρ_c and ρ_γ

are related through a Taylor expansion for ρ at γ in the normal direction as

$$\rho_c = \rho_\gamma - d\frac{\partial \rho}{\partial \boldsymbol{n}} + \mathcal{O}(d^2) \tag{2.11}$$

where d is the signed distance between the grid point c and point γ. Combining (2.3) and (2.11) we get the following estimation for ρ_γ

$$\rho_\gamma = d\ \frac{\rho_c + d\,\dfrac{D'}{D-D'}\,\rho_{\text{eq}}}{1 + d\,\dfrac{D'}{D-D'}}.$$

Furthermore, we approximate the first integral on the right-hand side of (2.10) as (see Figure 2.10)

$$\int_{\partial\mathcal{C}\cap\Omega} \nabla\rho^{n+1}\cdot\boldsymbol{n}\,d\Gamma \;=\; \frac{\rho_r-\rho_c}{s_r}L_{rf} - \frac{\rho_c-\rho_l}{s_r}L_{lf} + \frac{\rho_t-\rho_c}{s_r}L_{tf} - \frac{\rho_c-\rho_b}{s_r}L_{bf}\ ,$$

where L_{rf} (L_{lf}, L_{tf} and L_{bf}, respectively) is the length fraction of the right (left, top and bottom, respectively) face that is in Ω. Finally, we approximate the integral of a quantity Q over $\mathcal{C}\cap\Omega$ as

$$\int_{\mathcal{C}\cap\Omega} Q\,d\Omega = Q_c\int_{\mathcal{C}\cap\Omega} d\Omega\ ,$$

where Q_c denotes the value of Q at the center of cell $\mathcal{C}$. The integrations are performed by the algorithms introduced in [54]. These approximations define the coefficients in the linear system associated with grid node c.

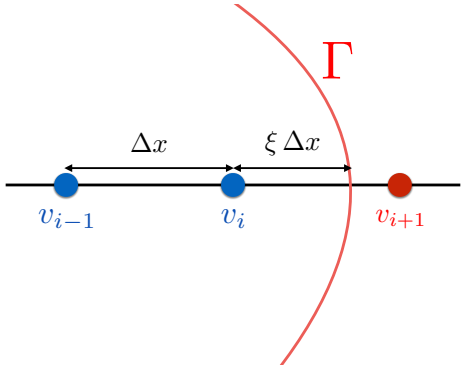

Figure 2.11: *Boundary condition for irreversible aggregation. The grid nodes on each side of the island boundary,* Γ*, belong to different islands' height.*

Case with irreversible aggregation

Irreversible aggregation is the regime in which $D' \to D$, i.e. when the Robin condition (2.3) reduces to the Dirichlet condition $\rho(\mathbf{x}) = 0$, taking $\rho_{\text{eq}} = 0$. This case deserves special attention: Numerically, the method described in Section 2.4.4 is prone to numerical errors in this case. To address this particular situation, we directly impose the condition $\rho(\mathbf{x}) = \rho_{\text{eq}}$ of Chen *et al.* [55], which is based on the Ghost-Fluid approach of Gibou *et al.* [56] and the Shortley-Wheller technique [57]. The discretization of the operator $\nabla \cdot (D\nabla\rho)$ in equation (2.1) follows a dimension-by-dimension approach, i.e. one treats the x-component of $\nabla \cdot (D\nabla\rho)$ with the Dirichlet condition in the x-direction only: The discretization in the x-direction at the grid node v_i is given by the scheme (see Figure 2.11)

$$\frac{\partial}{\partial x}\left(D\frac{\partial \rho}{\partial x}\right)(v_i) \approx \frac{D_{i+\frac{1}{2}}\dfrac{\rho_G - \rho_i}{\xi\Delta x} - D_{i-\frac{1}{2}}\dfrac{\rho_i - \rho_{i-1}}{\Delta x}}{(1+\xi)\Delta x}\,.$$

In this scheme, the ghost value, ρ_G, for ρ is provided by a quadratic extrapolation. Specifically, we construct a quadratic approximation, $\tilde{\rho}(x) = ax^2 + bx + c$, of ρ with $\tilde{\rho}(-\Delta x) = \rho_{i-1}$, $\tilde{\rho}(0) = \rho_i$, and $\tilde{\rho}(\xi\Delta x) = \rho_\Gamma$. Then, we define $\rho_G = \tilde{\rho}(\Delta x)$.

The linear systems resulting from the discretization of the adatom density, ρ, are solved by use of the combination of the biconjugate gradient stabilized iterative solver preconditioned with successive over-relaxation provided by the PETSc library. This computational approach is applied to the case with the Ehrlich-Schwoebel barrier and the case with irreversible aggregation.

Note that the quantity ρ_l is solved only for grid nodes that lie in the region Ω_l. To simplify subsequent calculations of the island boundary velocity, the values of ρ_l are extrapolated into a narrow band around the region Ω_l using the PDE-based approach of [15], so that valid values of ρ_l are available in some neighborhood of this region.

2.4.5 Motion of island boundaries

Next, we discuss the discrete scheme for updating the position of each island boundary. The normal velocity of the boundary of an island with height l is given by

$$\boldsymbol{v}_l = (D_{l-1}\nabla\rho_{l-1} \cdot \boldsymbol{n} - D_l\nabla\rho_l \cdot \boldsymbol{n})\boldsymbol{n} \ .$$

In this equation D_l stands for diffusion coefficient on terrace height l and $\boldsymbol{n}$ stands for normal direction to the island boundary pointing outwards.

Since the quantities ρ_l and ρ_{l-1} are available in some neighborhood of the island boundary (which is defined as the zero-level-set of ϕ_l), the gradients of ρ_l and ρ_{l-1} on the island boundary are obtained using standard finite-difference formulas. By the second-

order accurate formula of Chen *et al.* [47], we have

$$\begin{aligned}\frac{\partial \rho}{\partial x} =& \frac{\rho_g - \rho_T}{s_g} \cdot \frac{s_5}{s_g + s_5} + \frac{\rho_T - \rho_5}{s_5} \cdot \frac{s_g}{s_g + s_5} \\ & - \frac{s_3 s_4 s_5}{2 s_g (s_5 + s_g)} \left(\frac{\rho_1 - \rho_T}{s_1} + \frac{\rho_2 - \rho_T}{s_2} \right) \cdot \frac{2}{s_2 + s_1} \ , \qquad (2.12) \\ \frac{\partial \rho}{\partial y} =& \frac{\rho_1 - \rho_T}{s_1} \cdot \frac{s_2}{s_2 + s_1} + \frac{\rho_T - \rho_2}{s_2} \cdot \frac{s_1}{s_2 + s_1} \ . \qquad (2.13)\end{aligned}$$

Once the velocity, $\boldsymbol{v}_l$, of each island boundary is computed, the level-set function, ϕ_l, is evolved according to equation (2.5). In this work, we use a semi-Lagrangian scheme, i.e. for any grid point $\mathbf{x}^{n+1}$, we write $\phi_l^{n+1}(\mathbf{x}^{n+1}) = \phi_l^n(\mathbf{x_d})$ where $\boldsymbol{x_d}$ is computed by

$$\begin{aligned}\hat{\mathbf{x}} &= \mathbf{x}^{n+1} - \frac{\Delta t}{2} \cdot \boldsymbol{v}_l^n(\mathbf{x}^{n+1}) \ , \\ \mathbf{x_d} &= \mathbf{x}^{n+1} - \Delta t \cdot \boldsymbol{v}_l^{n+\frac{1}{2}}(\hat{\mathbf{x}}) \ .\end{aligned}$$

The velocity field $\boldsymbol{v}_l^{n+\frac{1}{2}}$ at the mid-time step, $t^{n+\frac{1}{2}}$, is defined linearly from the previous velocity fields by $\boldsymbol{v}_l^{n+\frac{1}{2}} = \frac{3}{2}\boldsymbol{v}_l^n - \frac{1}{2}\boldsymbol{v}_l^{n-1}$. Finally, quantities at the locations $\mathbf{x_d}$ and $\hat{\mathbf{x}}$ are approximated using non-oscillatory interpolation procedures; see [15] for details.

2.4.6 Transfer of data between grids

As the island boundaries evolve, the computational grid is automatically adapted so as to keep the smallest resolution near the boundary. Therefore, one needs to interpolate the data from the grid at time t^n to the grid at time t^{n+1}. Defining the data on a coarser grid from a finer one is trivial for a node-based approach since the values at the nodes of the coarser grid are simply those that existed on the finer grid. The reciprocal definition is carried out by the non-oscillatory quadratic interpolation scheme of [15]: for a unit

cell $\mathcal{C} = [0,1]^2$, the interpolated value of the adatom density, ρ, at the point (x, y) is

$$\begin{aligned}\rho(x,y) = {} & \rho(0,0)(1-x)(1-y) \\ & + \rho(0,1)(1-x)(\quad y) \\ & + \rho(1,0)(\quad x)(1-y) \\ & + \rho(1,1)(\quad x)(\quad y) - \frac{\partial^2\rho}{\partial x^2}\frac{x(1-x)}{2} - \frac{\partial^2\rho}{\partial y^2}\frac{y(1-y)}{2} ,\end{aligned} \tag{2.14}$$

where

$$\frac{\partial^2\rho}{\partial x^2} = \underset{v\in\text{vertices}(\mathcal{C})}{\text{minmod}}\,(D^0_{xx}\rho(v)) \qquad \text{and} \qquad \frac{\partial^2\rho}{\partial y^2} = \underset{v\in\text{vertices}(\mathcal{C})}{\text{minmod}}\,(D^0_{yy}\rho(v)) .$$

In the last two formulas, `minmod` denotes the standard slope limiter operator [58, 59]; and the second-order derivative, D^0_{xx}, in the x-direction at node v_T is approximated with central differencing, viz.,[1]

$$D^0_{xx}\rho_T = \frac{\rho_G - \rho_T}{s_G}\cdot\frac{2}{s_1+s_G} - \frac{\rho_T-\rho_1}{s_1}\cdot\frac{2}{s_1+s_G} .$$

2.5 Numerical Results

In this section we will present numerical results of our implementation of the IDM. In section 2.5.1 we will discuss how the parallelization and the adaptive mesh refinement affect the efficiency of our code. In section 2.5.2 we will present results that can be compared to previously published results obtained with a Dirichlet boundary condition to demonstrate that we do indeed include the same physical information as in previous work. Finally, in section 2.5.3 we show some initial results that illustrate how this approach allows us to efficiently reach growth regimes that were previously difficult or impossible to reach with existing approaches.

[1] The second-order derivative in the y-direction is approximated similarly.

2.5.1 Computational efficiency of the new approach

One of the key components of our revised approach and new implementation of the IDM is the parallelization of our code. The efficiency of this parallelization is shown in Fig. 2.12. Clearly, for the system size and parameters chosen for this example, we get almost perfect linear speedup of our code for using up to 512 processors. We get very similar results for other simulations with different physical parameters. The speedup slows down (and eventually is reversed) when we use more than 512 processors. The reason is that the extra cost associated with communication between processors becomes dominant compared to the amount of local computations. We have verified that this turning point in the scaling occurs when fewer (more) processors are used for systems with fewer (more) grid points in the simulations (data not shown).

The other major component of this approach is the adaptive mesh refinement using Quadtree grids. The efficiency of using adaptive grids and the speedup that can be achieved is shown in Fig. 2.13 for two different maximum grid resolutions ($l_{\max} = 8$ and $l_{\max} = 10$). Taking the coarsest grid resolution (i.e. the tree level $l_{\min}$) to be lower than the finest grid resolution (i.e. the tree level $l_{\max}$) leads to a significant reduction in the number of degrees of freedom, and thus in the computational cost by a factor of about 7 for $(5, 8)$-tree instead of a uniform $(8, 8)$-grid.

2.5.2 Results with the Dirichlet boundary condition for irreversible aggregation

We now discuss the validation of our implementation of the IMD, and focus on the case of irreversible aggregation, i.e. the case where $\rho = 0$ at the islands' boundary. For this case the IDM has been thoroughly validated against KMC simulations in [12]. We

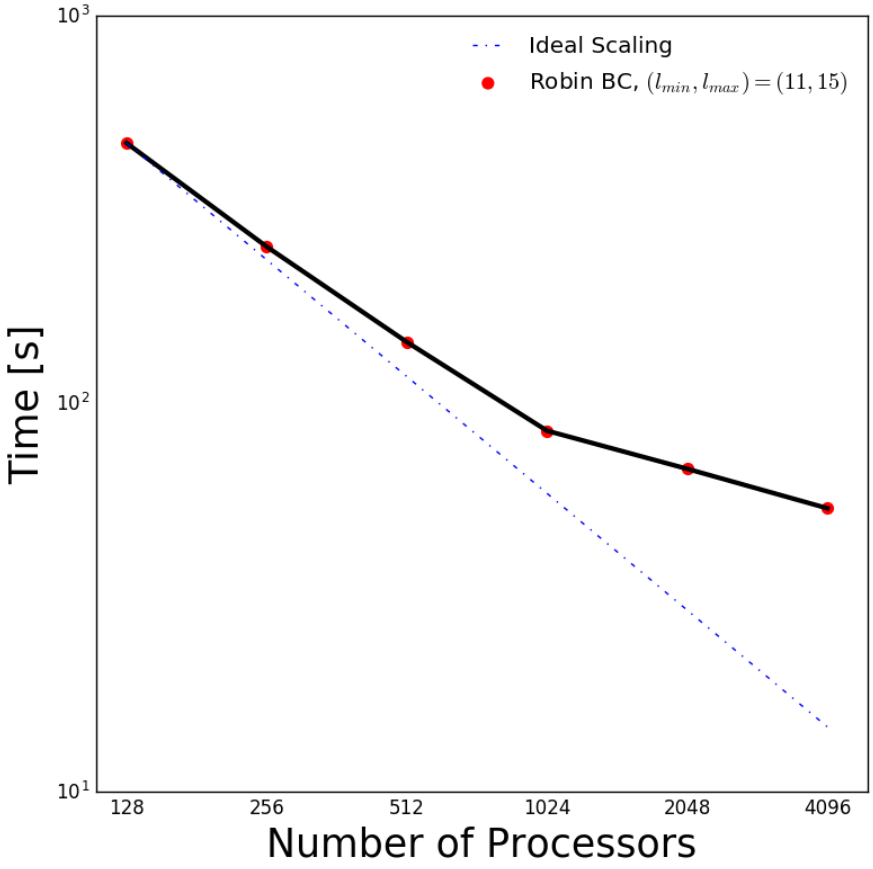

Figure 2.12: *Scaling of the computational time as a function of the number of processors. This scaling is performed on a lattice of size* $L = 180$ *on resolution levels* $(11, 15)$*. The boundary condition is of Robin type with a barrier size of* 0.2 *and the final coverage is* $\approx 0.9\%$ *(i.e.* 140 *iterations in all cases).*

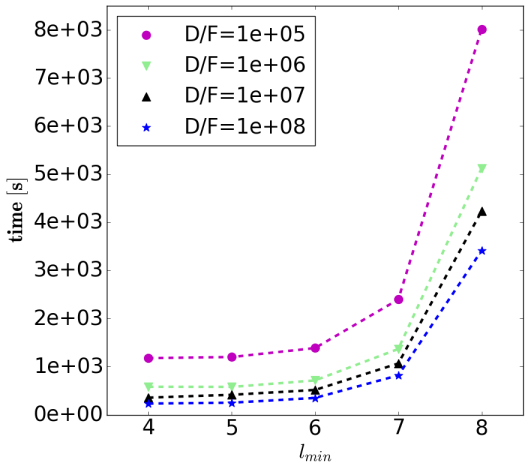

Figure 2.13: *Speedup from varying the adaptivity levels of the grid for different D/F values on a range of grid configurations. For all cases we use Robin boundary condition with a step edge barrier of size* 0.2 *and the final coverage is* 20% *covering only one layer (submonolayer growth). All simulations are run on a single processor.*

consider a lattice of size $L = 180^2$ and adaptive grids with levels $(7, 11)$, on a 2×2 macro grid and $D/F = 10^5$, 10^6 and 10^7. In the simulations discussed here the lattice size is chosen as $L = 180$ and the final coverage is 20%. Figure 2.14 shows the adatom density and the island density as a function of coverage for different values of D/F. The results agree qualitatively and quantitatively with the results presented in [12].

In addition to densities we also check for the proper spatial distribution of the islands on the surface. The scaled island size distribution for the different values of D/F is shown in Fig. 2.15. These results also agree with the scaled island size distribution functions that were published in [12] (and that were validated against KMC simulations). Thus, we have checked that densities and morphologies that are obtained for irreversible aggregation (in the absence of a step edge barrier) are the ones that we expect for this model.

Figure 2.16 depicts the result of a simulation on a large lattice and with a high level

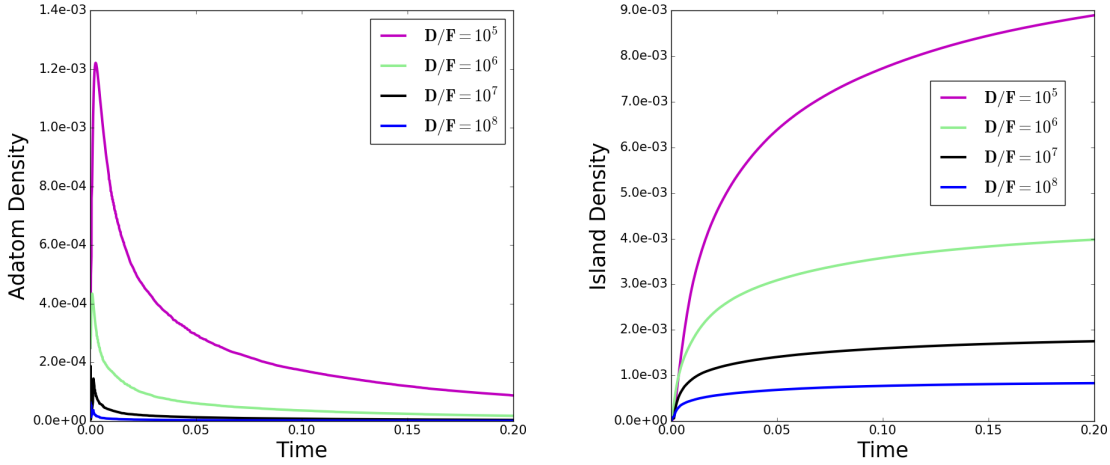

Figure 2.14: *[$<\rho>$ for different D/F.], [N for different D/F.], The adatom density (left) and island density (right) for different values of D/F in the case of the boundary condition $\rho = 0$ (irreversible aggregation).*

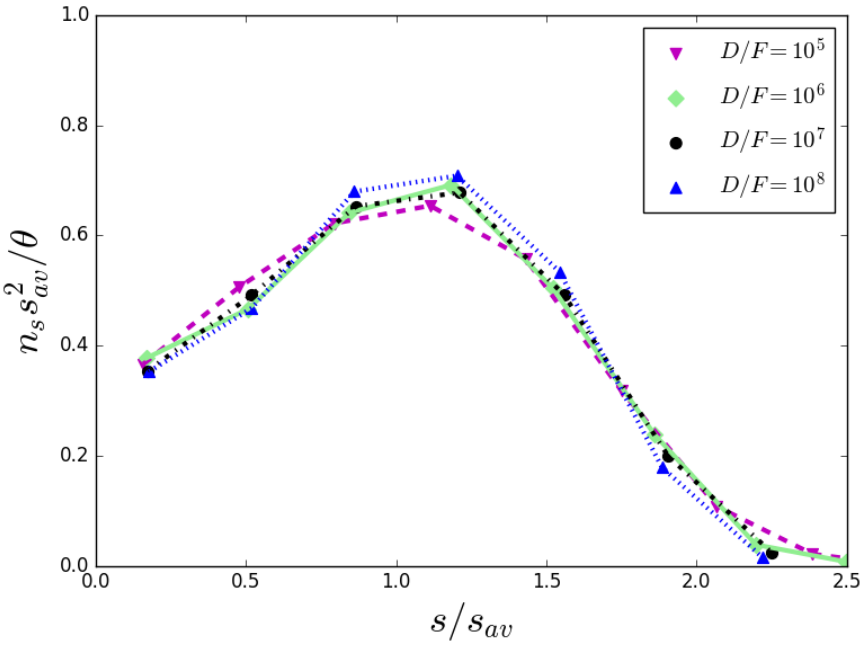

Figure 2.15: *Cluster size distribution in the case of the boundary condition $\rho = 0$ (irreversible aggregation). Each curve consists of 50 simulations with a lattice size of $L = 180$ on a 2×2 macro grid. Each simulation has a final coverage of 20%.*

of refinement. The zooms illustrate that small islands can be highly resolved, while at the same time large domains are considered. In particular, Figure 2.5.2 shows that an island of size 2 is highly resolved.

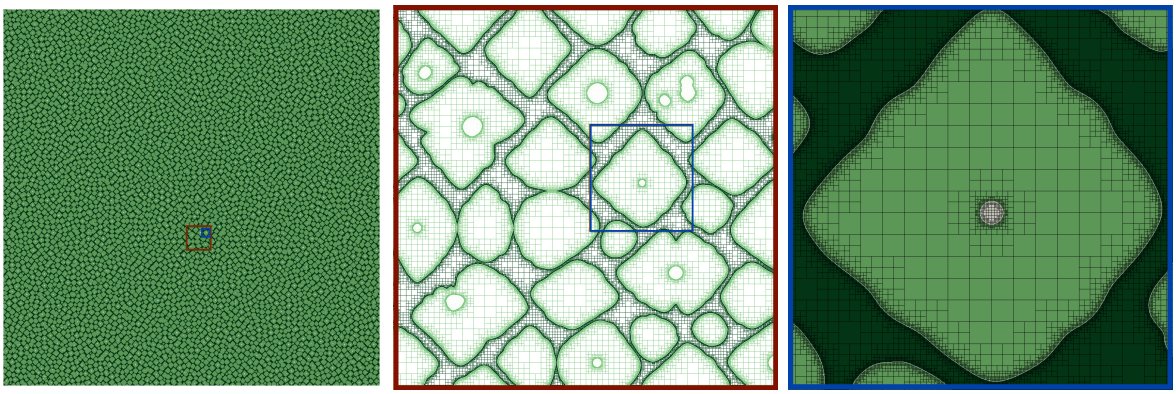

Figure 2.16: *The lattice has size $L = 1000$. Dirichlet boundary condition. This simulation uses a 2×2 macro grid with a (6, 13) Quadtree and 256 processors. The simulation took 48 hours. Left: islands in the computational domain. Middle: zoom on an island. Right: double Zoom showing a dimer in the center.*

2.5.3 Results with the Robin boundary condition to simulate the formation of mounds

We now turn our attention to simulations that use the Robin boundary condition that is needed to simulate the effect of an ES barrier. The results shown in Figure 2.5.3 show the surface morphology and adatom density after the deposition of 7 layers for a simulation with an ES barrier defined by $D'/D = 0.1$ (i.e., for the case where an adatom at the edge of a terrace is 10 times more likely to stay on the terrace than it is to diffuse downward) and $D'' = 0.95D$. Clearly, even after just a few layers are grown we see the onset of mound formation. We note that these mounds are rather steep, and that in fact the typical terrace width in the middle of each side facet has a width that is of the order of one lattice constant (or even less). The reason that we do not see slope selection

is that we do not include any mechanism for downward transport (such as downward funneling [60, 61]. Nevertheless, close inspection of Figure 2.5.3 illustrates that even for such small (narrow) terraces our adaptive scheme is able to resolve a meaningful adatom concentration on each terrace. For most mounds, the adatom concentration is rather low for lower layers (as these layers exhibit the most narrow terraces). The adatom concentration is larger for the topmost layer (or a few layers at the top), as these layers are not quite as narrow, and allow for a larger buildup of adatoms. This is better illustrated in Figure 2.18 where a few mounds are formed.

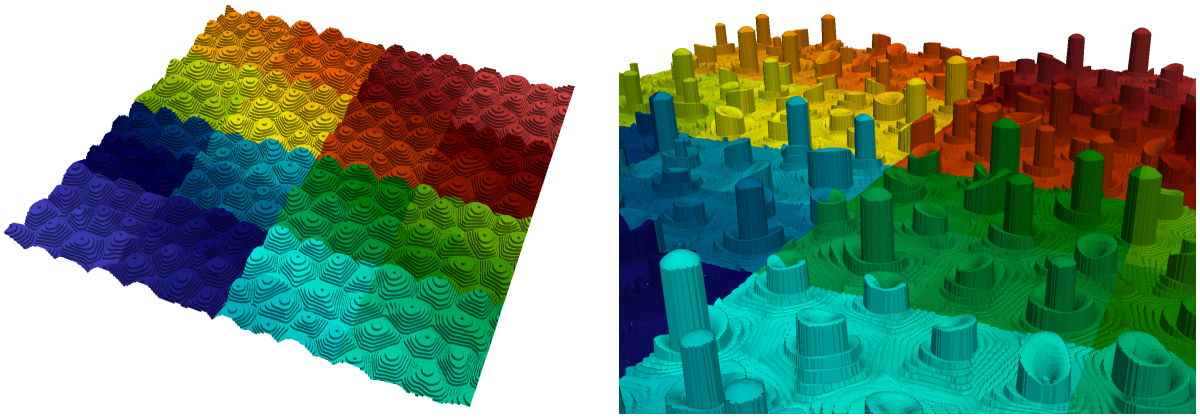

Figure 2.17: *Ehrlich-Schwoebel barrier and the formation of mounds in a deterministic seeding. The colors represent the processors' rank. This simulation uses a* 2×2 *macro grid with a (5, 9) Quadtree and took 24 hours on 192 processors with up to 1M nodes. The physical parameters are* $L = 180$, $D/F = 10^5$ *and* $D'/D = 0.1$. *1,429 islands were nucleated, 7 layers grown with 93.0% coverage at the end, 40,000 time iterations. Left: a view on mounds in computational domain. Right: adatom density.*

Finally, Figure 2.19 shows how the strength of the step edge barrier affects the formation of mounds. When $D'/D = 0.01$, we see clearly the formation of well defined mounds that are shaped like a "wedding cake" with 10 exposed terraces after the deposition of 11 layers. As D'/D increases (and the relative strength of the ES barrier weakens), mounds are less pronounced, and the morphology is very close to so-called layer-by-layer growth

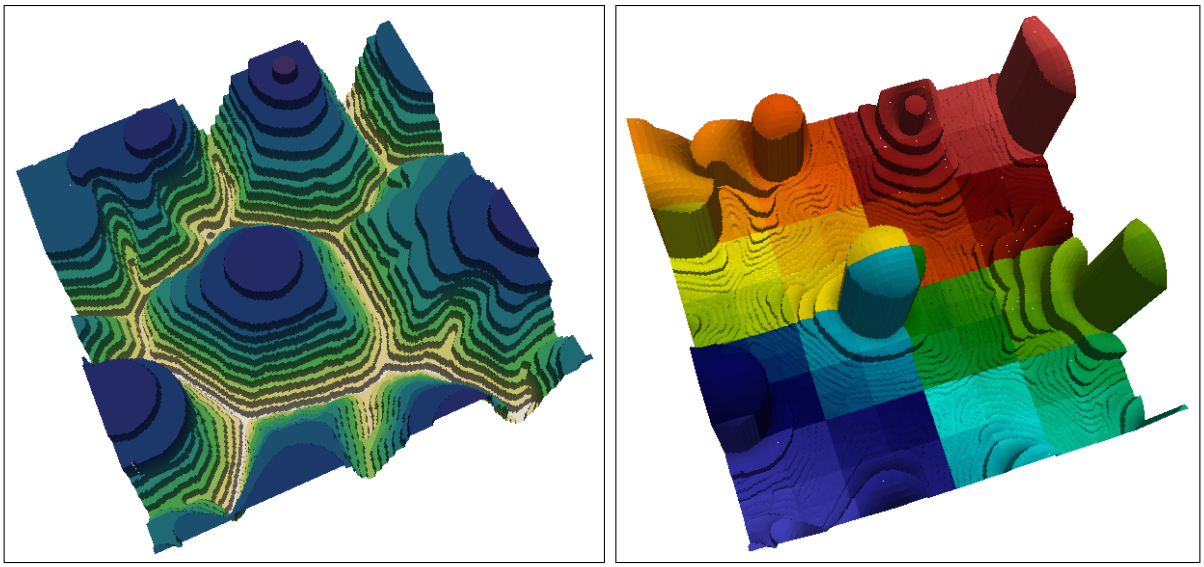

Figure 2.18: *Ehrlich-Schwoebel barrier and the formation of a single mound in a stochastic seeding. The lattice has size* $L = 30$ *and the* $D/F = 10^5$*. This simulation uses a* 2×2 *macro grid with a (5, 7) Quadtree and 256 processors. The left panel shows different layers (up to 11 layers) deposited and the right panel is a representation of the density field color coded by processor ranks. A closer look demonstrates the density is higher at the topmost layer of the island. Left: different layers. Right: adatom density.*

when $D'/D = 0.95$

2.6 Conclusion

In this paper, we developed a computational method for simulating epitaxial growth on a forest of Octrees by use of the level set technique for the IDM. In our formulation, we considered both Dirichlet and Robin boundary conditions for the adatom density at the island boundaries. These boundary conditions correspond to the cases without a step edge barrier (Dirichlet condition) and with a step edge barrier (Robin condition). In addition, we described the implementation of a parallel framework for our code. Our simulation results are in qualitative and quantitative agreement with previously known

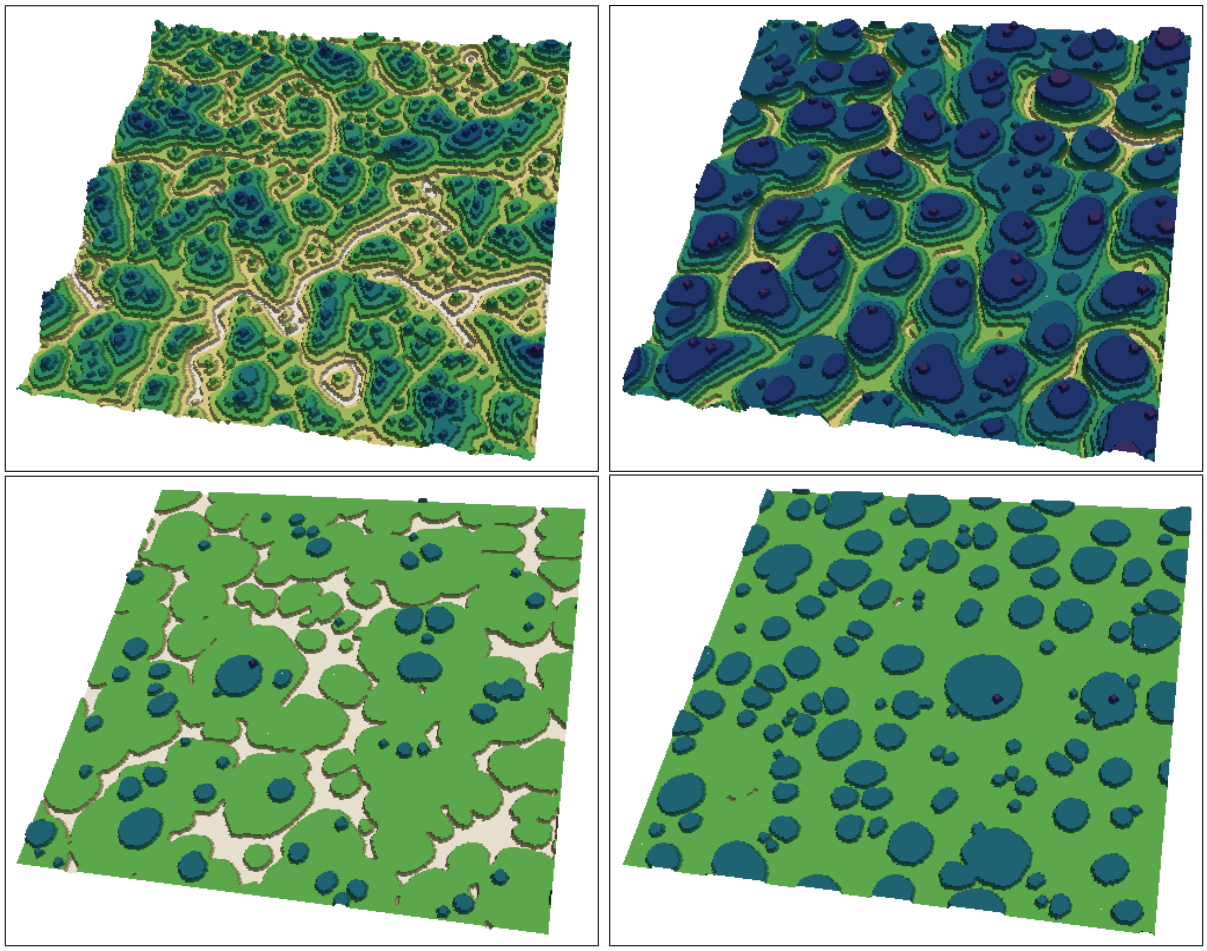

Figure 2.19: *Robin boundary condition and formation of mounds. The lattice has size* $L = 180$ *and the* $D/F = 10^6$*. This simulation uses a* 2×2 *macro grid with a (4, 7) Quadtree and 256 processors. The colors represent the islands heights with levels illustrated in each figure. All snapshots are at the same level. Top left:* $D'/D = 0.01$*. Top right:* $D'/D = 0.1$*. Bottom left:* $D'/D = 0.3$*. Bottom right:* $D'/D = 0.95$*.*

results. This comparison offers a validation of our method in the physical context of the IDM.

One of the most significant aspects of our work is the fact that the efficiency of the implementation is orders of magnitude better than previous implementations of the IDM. Specifically, the parallel implementation of our code yields good scaling of the computational time versus the number of processors used; we have considered approximately 1000 processors and typical parameter choices. The Octree implementation allows us to use coarse grids away from islands that are much coarser than the fine grid near the boundaries. For some cases the coarse grid that we used was 128 coarser than the fine grid in each spatial direction, resulting in a large speedup without a noticeable decrease of accuracy.

This fast and efficient implementation allows us to study regimes of epitaxial growth that could not be reached in the past because of limitations of previous methods. We are currently working towards implementing the effect of 'downward funneling', a mechanism by which slope selection may occur in epitaxial growth. Our goal is to efficiently study the formation of mounds, and the selection of slopes as a competition between a step edge barrier and downward funneling. We also plan to implement the effect of step-step interactions, which is expected to compete with downward funneling for slope selection. Our ultimate, practical goal is to model and simulate the formation of quantum dots in the presence of strain on crystal surfaces.

Acknowlegment

The research of P. Mistani, D. Bochkov, A. Guittet and F. Gibou was supported by NSF DMS-1412695. The research of D. Margetis was supported by NSF DMS-1412769. The research of J. Schneider and C. Ratsch was supported by NSF DMS 1412392 and

DMS 1440415. This work used the Extreme Science and Engineering Discovery Environment (XSEDE), which is supported by National Science Foundation grant number ACI-1053575. The authors acknowledge the Texas Advanced Computing Center (TACC) at The University of Texas at Austin for providing HPC and visualization resources that have contributed to the research results reported within this paper.

Chapter 3

Mesoscale simulations of cell aggregate electroporation

3.1 Abstract

We introduce an approach for simulating mesoscale electropermeabilization of an aggregate of cells. We employ a forest of Octree grids along with a Voronoi mesh in a parallel environment and in the context of the level-set method that exhibits excellent scalability. We exploit the electric interactions between the cells through a nonlinear phenomenological model that is generalized to account for the permeability of the cell membranes. We use the Voronoi Interface Method (VIM) to accurately capture the sharp jump in the electric potential on the cell boundaries. The case study simulation covers a volume of $(1\ mm)^3$ with more than $27,000$ well-resolved cells with a heterogeneous mix of morphologies that are randomly distributed throughout a spheroid region with a volume fraction of 13%. This framework enables unprecedented direct numerical studies of the electropermeabilization effects at the meso-scale. Our simulations qualitatively replicate the shadowing effect observed in experiments and reproduce the time evolution

of the impedance of the cell sample in agreement with the trends observed in experiments. This approach sets the scene for performing homogenization studies for understanding the effect of tissue environment on the efficiency of electropermeabilization.

3.2 Introduction

Electropermeabilization (also called electroporation) is a significant increase in the electrical conductivity and permeability of the cells' membrane that occur when pulses of large amplitude (a few hundred volts per centimeter) are applied. The physical basis of this phenomenon lies in the fact that, since membranes are mainly composed of phospholipids and proteins, they behave like a capacitor in parallel with a resistor. The applied electric field is then dramatically enhanced in the vicinity of the membrane, leading to a jump of the electric potential. This locally varying transmembrane potential difference (TMP) can prevail over the cell membrane barrier in regions where this difference surpasses the electroporation threshold.

This phenomenon has attracted increasing attention due to its capacity to facilitate targeted drug delivery of non-permeant cytotoxic molecules such as bleomycin or cisplatin [62]. DNA vaccination and gene therapy are other promising applications for electropermeabilization, which enables non-viral gene transfection [63].

However, despite extensive scrutiny of this phenomenon, no substantial evidence of the elementary mechanism of electropermealization has been obtained. Nevertheless, the most accepted theory speculates the creation of pores in the membrane as a consequence of a large transmembrane voltage. However these pores have not yet been observed. One important reason behind this inability is that, in the absence of cell imaging techniques in the nanometer scale, almost all experiments that have studied the electroporation effect have used tissue scale samples to infer the underlying molecular level processes.

Such inferences have led to the advent of different theoretical models, with membrane pore density approaches being among the most popular mechanisms. Developments in this avenue have been carried out in the work of Debruin and Krassowska [64] and have been augmented in [65] and [66] to incorporate the spatio-temporal evolution of the speculated pore radii. Other attempts have been made to model the tissue scale behavior of electropermeabilization [67].

Recently, Leguebe *et al.* [68] have proposed a phenomenological approach to model this effect at single-cell scale in terms of a nonlinear partial differential equation. Their description determines the local behavior of each cell membrane under the influence of its surrounding electric potential in a continuous manner. Remarkably, this representation qualifies for a multi-scale characterization of electropermeabilization. However, we note that in practice these models embody calibrations of free parameters that are tuned by experimenting on populations of cells and extending these measurements to single-cell scale, oversighting the multi-scale nature of electropermeabilization in the experiments. Such approximations are inevitable in the absence of numerical tools to adjust these models in accordance with experiments. However, recent attempts have been made in the work of Voyer *et al.* [69] to theoretically extend this model to tissue scale.

We emphasize the predictability of any such model at the cell aggregate regime to corroborate these results. However, such comparisons with available experimental results were prohibitive in the case of electropermeabilization, partially due to the enormous computational costs of such ventures as well as the complexity of the molecular events involved in membrane electropermeabilization. To facilitate the accurate modeling of molecular processes that regulate electropermeabilization, there has been emerging incentive to overcome the hindering computational difficulties.

In the wake of the aforementioned arguments, the advent of "direct" tissue scale simulations seems necessary. Such simulations not only commission better understanding

of the involved molecular processes, but also will aid developing semi-analytic models of the overall permeabilization of the tissue under different circumstances. Such endeavors require a complete characterization of the relevant physical parameters from cell scale physics to tissue scale configurations.

Quite recently, significant progress has been made in this venue by Guittet *et al.* [70]. They have proposed a novel Voronoi Interface Method (VIM) to capture the irregular cell interface and accurately impose the sharp TMP jump. The VIM utilizes a Voronoi mesh to capture the irregular interface before applying the dimension-by-dimension Ghost Fluid Method [71, 72, 73]. This is aimed to direct the fluxes normal to the interface where there is a discontinuity. This reframing the mesh around the interface guarantees the convergence of the solution's gradients. Also, only the right hand side is affected by the TMP jump which simplifies the computational treatment.

We also note that an alternative framework would be using adaptive Chimera grids as proposed by English *et al.* [74]. In their proposed method, English *et al.* used multiple Cartesian grids in different regions of the domain that are coupled on their boundaries by generating a Voronoi mesh. In the case of electroporation, one could also use finer Cartesian grids near the cell membrane that are coupled on the cell boundary with a Voronoi extension.

Guittet *et al.* [70] have derived a finite volume discretization for this phenomenon and implemented it in a serial framework. Their numerical results are in agreement with experimental expectations. However, the computational costs of solving the involved discretization prohibited the consideration of tissue scale simulations.

Here, we build on the method proposed by Guittet *et al.* [70] and generalize their approach to a parallel environment. This parallelization empowers simulations of the single-cell model of Leguèbe and Poignard *et al.* [68] at the tissue scale, hence providing a framework to validate or improve the understanding of cell electroporation.

The structure of this paper is as follows. We introduce the mathematical model for our simulations in section 3.3 and the computational strategy that we develop in section 3.4. Then we present performance of our implementation as well as some preliminary demonstrations of the numerical results in sections 3.5. In section 3.6 we illustrate the emergence of macro-level properties in the cell aggregate. We conclude with a summary of our main results in section 3.7.

3.3 Cell membrane model

3.3.1 Geometric representation

The cell cytoplasm Ω^c and the extracellular matrix Ω^e are separated by a thin and resistive membrane denoted by Γ. The outward normal to Ω^c is denoted by $\mathbf{n}$. Figure 3.1 illustrates the geometry in the case where a single cell is considered. The entire domain is denoted by $\Omega = \Omega^e \cup \Gamma \cup \Omega^c$. We denote the conductivities of the materials by σ^c and σ^e for the cell and the extracellular matrix respectively.

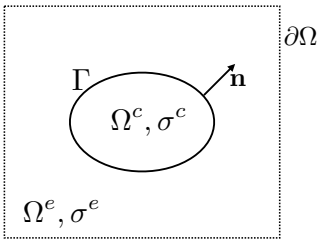

Figure 3.1: *Illustration of a single cell immersed in the extracellular matrix. The conductivity of the materials is denoted by* σ.

3.3.2 Electrical model

For simulating the electropermeabilization process, we solve the following boundary value problem defined in equations (4.6a)–(4.6e). The electric potential field u in the computational domain is governed by the Laplace equation:

$$\Delta u = 0,\ \boldsymbol{x} \in (\Omega_c \cup \Omega_e), \tag{3.1a}$$

with the appropriate boundary conditions:

$$[\sigma \partial_{\boldsymbol{n}} u]_\Gamma = 0,\ \boldsymbol{x} \in \Gamma, \tag{3.1b}$$

$$C_m \partial_t [u]_\Gamma + S(t, [u])\,[u] = \sigma \partial_{\boldsymbol{n}} u|_\Gamma,\ \boldsymbol{x} \in \Gamma, \tag{3.1c}$$

$$u(t, \boldsymbol{x}) = g(t, \boldsymbol{x}),\ \boldsymbol{x} \in \partial\Omega, \tag{3.1d}$$

and the homogeneous initial condition:

$$u(0, \boldsymbol{x}) = 0,\ \boldsymbol{x} \in \Omega, \tag{3.1e}$$

where we used the $[\cdot]$ notation for describing the jump operator across Γ.

Equation (4.6b) imposes the continuity of the electric flux across the membrane, (4.6c) captures the capacitor and resistor effect of the membrane and (4.6d) is the external voltage applied on the boundaries of the domain. In these equations, C_m and S are the capacitance and conductance of the membrane material respectively. The source term corresponding to the applied voltage is denoted by $g(t, \boldsymbol{x})$. The effect of the electroporation current is modeled by the $S(t, [u])\,[u]$ term in equation (4.6c). We adopt a nonlinear description of the conducting membrane [68] in the next subsection.

3.3.3 Membrane electropermeabilization model

The long-term permeabilization of the membrane is modeled by formulating the surface membrane conductivity. Leguébe, Poignard *et al.* [68] modeled the surface conductivity of the membrane as follows:

$$S_m(t,s) = S_0 + S_{ep}(t,s) = S_0 + X_1(t,s) \times S_1 + X_2(t,s) \times S_2, \quad \forall t > 0, s \in \Gamma \tag{3.2}$$

In this equation S_0, S_1 and S_2 are the surface conductance of the membrane in the resting, porated and permeabilized states, respectively. The level of poration and permeabilization of the membrane are captured in the functions X_1 and X_2. These are computed as a function of the transmembrane potential difference and are valued in the range $[0,1]$ by definition. The ordinary differential equations determining X_1 and X_2 read:

$$\frac{\partial X_1(t,s)}{\partial t} = \frac{\beta_0(s) - X_1}{\tau_{ep}}, \quad X_1(t,s) = 0, \tag{3.3a}$$

$$\frac{\partial X_2(t,X_1)}{\partial t} = max\left(\frac{\beta_1(X_1) - X_2}{\tau_{perm}}, \frac{\beta_1(X_1) - X_2}{\tau_{res}}\right), \quad X_2(t,s) = 0. \tag{3.3b}$$

The parameters τ_{ep}, τ_{perm} and τ_{res} are the time scales for poration, permeabilization and resealing, respectively. Furthermore, in the above equations β_0 and β_1 are regularized step-functions defined by:

$$\beta_0(s) = e^{-\frac{V_{ep}^2}{s^2}}, \quad \forall s \in \mathbb{R}, , \tag{3.4a}$$

$$\beta_1(X) = e^{-\frac{X_{ep}^2}{X^2}}, \quad \forall X \in \mathbb{R}, , \tag{3.4b}$$

where V_{ep} and X_{ep} are the membrane voltage and the poration thresholds respectively.

3.4 Computational strategy

3.4.1 Level-set representation

As presented by Guittet *et al.* [70], we describe the cells in our simulations using the level-set method as first introduced by [75] (see [76] for a recent review) and in particular the technology on Octree Cartesian grid by Min and Gibou [15]. To this end, we construct a spatial signed-distance function ϕ relative to the irregular interface Γ such that:

$$\phi(\boldsymbol{x}) = \begin{cases} d(\boldsymbol{x}, \Gamma) > 0, \ \boldsymbol{x} \in \mathcal{O}_e \\ d(\boldsymbol{x}, \Gamma) = 0, \ \boldsymbol{x} \in \Gamma \\ -d(\boldsymbol{x}, \Gamma) < 0, \ \boldsymbol{x} \in \mathcal{O}_c \end{cases}, \boldsymbol{x} \in \mathbb{R}^3, \tag{3.5}$$

where $d(\boldsymbol{x}, \Gamma)$ is the Euclidean distance from a given point in the domain to the 0-th level-set hyperspace:

$$d(\boldsymbol{x}, \Gamma) = \inf_{\boldsymbol{y} \in \Gamma} d(\boldsymbol{x}, \boldsymbol{y}),$$

Figures 3.4.1 and 3.4.1 give an example of such interface representation and a sample level-set function, respectively.

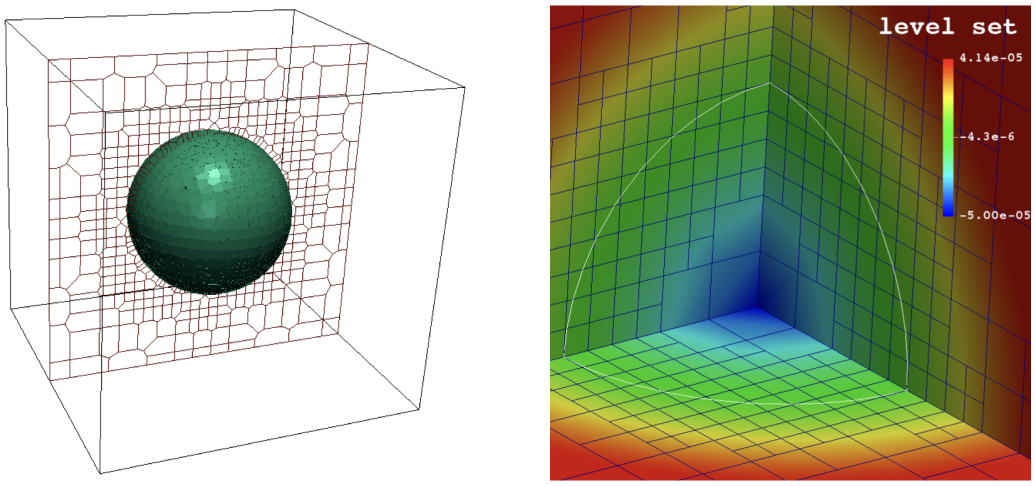

Figure 3.2: *(left) A Voronoi mesh is fitted to the surface of a membrane in 3D. (right) The level-set representation of a single cell on the dual adaptive Cartesian grid at levels* $(4, 6)$*. The membrane is resolved at the highest resolution while farther regions are at lower resolution. Also, the level-set function* ϕ *is negative inside the cell (cooler colors) and positive outside the cell (warmer colors).*

3.4.2 Octree data structure and refinement criterion

Simulating a large number of biological cells in three spatial dimensions requires minimizing the total number of degree of freedom without loss of accuracy. As the physical variations in the solution occur close to the membrane, one needs more nodes to capture the physics at the vicinity of the biological cells compared to farther regions. We utilize the adaptive Cartesian grid based on Quad-/Oc-trees [77, 78]. A "Quad-/Oc-tree" is a recursive tree data structure where each node is either a leaf node or a parent to 4/8 children nodes. The Octree is constructed by setting the root of the Octree to the entire computational domain. Then higher resolutions are achieved by recursively dividing each cell into 8 subcells (or 4 subcells in the case of Quadtrees). We use the following refinement criteria introduced by [79] and extended by [80] to orchestrate this partitioning of space:

Refinement/coarsening criterion: Split a cell ($\mathcal{C}$) if the following inequality ap-

plies (otherwise merge it to its parent cell):

$$\min_{v \in \text{vertices}(\mathcal{C})} |\phi(v)| \leq \text{Lip}(\phi) \cdot \text{diag-size}(\mathcal{C}), \tag{3.6}$$

where we choose a Lipschitz constant of $\text{Lip}(\phi) \approx 1.2$ for the level-set ϕ. Furthermore, diag-size($\mathcal{C}$) stands for the length of the diagonal of $\mathcal{C}$ and v refers to its vertices. Intuitively, the use of the signed-distance function in equation (3.6) translates into a refinement based on distance from the interface. This process is depicted in figure 3.4.2. An Octree is then characterized by its minimum/maximum levels of refinement. Figure 3.4.2 illustrates an example of a levels (3,8) tree meaning the minimum and maximum number of cells in each dimension are $2^3 = 8$ and $2^8 = 256$ respectively.

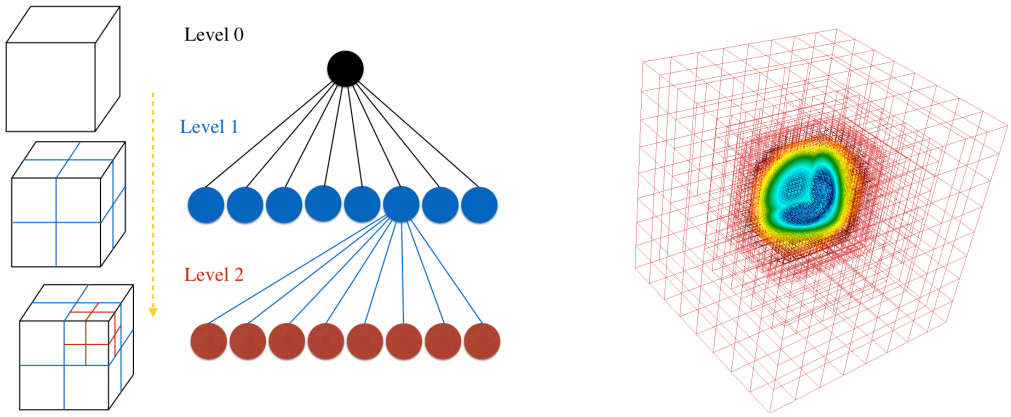

Figure 3.3: *Illustration of an Octree mesh and its data structure. (left) Two levels of refinement are illustrated. (right) A portrait of 8 levels of refinement in practice. Note that each dimension is divided into at most* $2^8 = 256$ *cells.*

Note that if larger macromesh is used these numbers will be multiplied by the macromesh number; *e.g.* if one sets $n_x = 2$ for levels $(3, 8)$ then the number of cells in x-direction will be twice as before, *i.e.*, bound between 16 and 512 instead. This is the case in all of the simulations in this work.

3.4.3 Parallel framework

We utilize the parallelism scheme introduced by Mirzadeh *et al.* [81]. This scheme is built upon the `p4est` software library [82]. `p4est` is a suite of scalable algorithms for parallel adaptive mesh refinement/coarsening (AMR) and partitioning of the computational domain to a forest of connected Quad-/Oc-trees. The partitioning strategy used in `p4est` is illustrated in figure 3.4. This process is [82]:

- A uniform macromesh is created;
- A forest of Octrees is recursively constructed using all processes;
- The produced tree is partitioned among all processes using a Z-ordering; *i.e.*, a contiguous traversal of all the leaves covering all the octrees.

The Z-ordering is then stored in a one dimensional array and is equally divided between the processes. This contiguous partitioning optimizes the communication overhead compared to the computation costs when solving equations in parallel. To perform the discretizations derived for this problem, we need to construct the local Octrees from the one dimensional array of leaves. To this end, following the method suggested by Mirzadeh *et al.* [81], we construct a local tree on each process such that the levels of its leaves matches that of the leaves produced by the `p4est` refinement. This is because `p4est` does not provide the vertical structure, and we need to be able to find a cell containing a point quickly, in $\mathcal{O}(\log(N))$. Each process stores only its local grid plus a surrounding layer of points from other processes, *i.e.*, a ghost layer.

3.4.4 Quasi-random cell distribution

To computationally capture the effects of a large aggregate of cells under the influence of an external electric stimulant, first we need to efficiently mimic the randomness in the

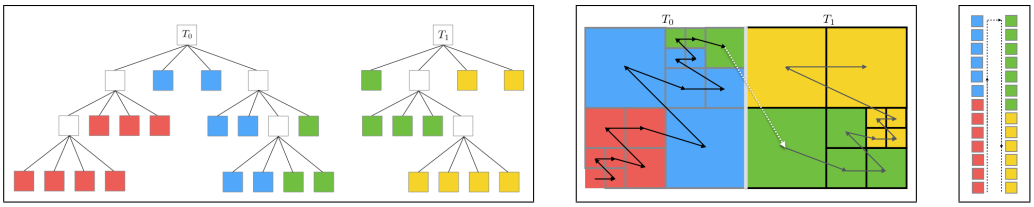

Figure 3.4: *A "forest" composed of two Quadtrees T_0 and T_1 (left) partitioning the whole geometric domain following a Z-ordering of all the octants in the domain (center). The partitioning is performed such that each process receives equal (± 1) number of contiguous octants traversing the leaves from left to right (right). Here there are four different processes depicted by four different colors.*

distribution of the cells while simultaneously constraining the minimum distance among the cells. In fact, for the purposes of this work we need to simulate tens to hundreds of thousands of cells in a relatively small computational domain if we are to observe the relevant aspects of electropermeabilization at the tissue scale.

To this end, we distribute the cells using the quasi-random numbers generated by the Halton Quasi Monte Carlo (HQMC) sequence [83, 84, 85, 86]. Quasi-random sequences are more uniformly distributed than the well-known pseudo-random sequences as illustrated in figure 3.5. As seen in this figure, while uniform pseudo-random numbers suffer from local clustering and voids, the HQMC sequence spans the space more uniformly. Mathematically, the uniformity of a sequence is measured by its "discrepancy" which is measured by comparing the number of points in a given region of space with the number of points expected from an ideal uniform distribution [83]. The quasi-random sequences are also called *low* discrepancy sequences as they exhibit a more uniform spatial coverage. Remarkably, the low discrepancy characteristic is inherently built in the HQMC algorithm, as opposed to a pseudo-random number generator that would require further processing.

In our approach, we locate each cell at the next element in a three dimensional HQMC sequence while skipping the elements that violate the minimum distance criterion to the

previously located cells. In contrast to a pseudo-random based technique, such rejections are very rare due to the intrinsic low discrepancy of the HQMC sequence, and hence the efficiency of our technique. As the number of cells increases in our simulations, it becomes computationally prohibitive to generate such a non-overlapping pseudo-random distribution of cells at high densities. Our experiments with HQMC demonstrate that a moderately dense non-overlapping cluster of cells can be generated at least hundreds of times faster than a pseudo-random number based technique. Notably, initializing higher cluster volume fractions (a volume fraction of $\mathrm{n} = \dfrac{\text{volume of the cells}}{\text{volume of the spheroid}} \approx \mathcal{O}(10^{-1})$) seems completely impossible using pseudo-random number generators.

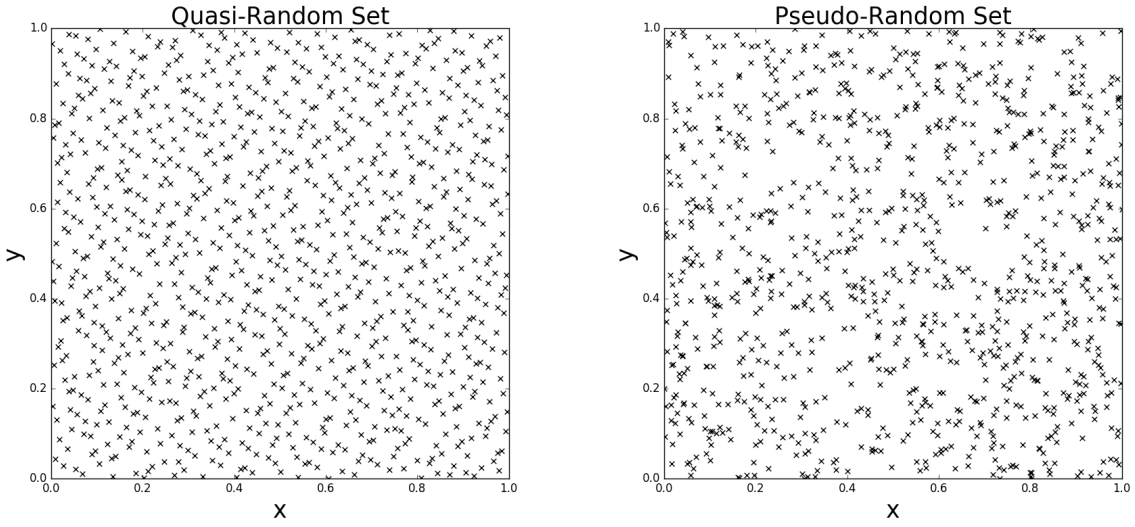

Figure 3.5: *(left) Quasi-random number distribution versus (right) pseudo-random number distribution. The quasi-random sequence immediately exhibits a much more uniform distribution of points.*

3.4.5 Discretization of the equations - the Voronoi Interface Method

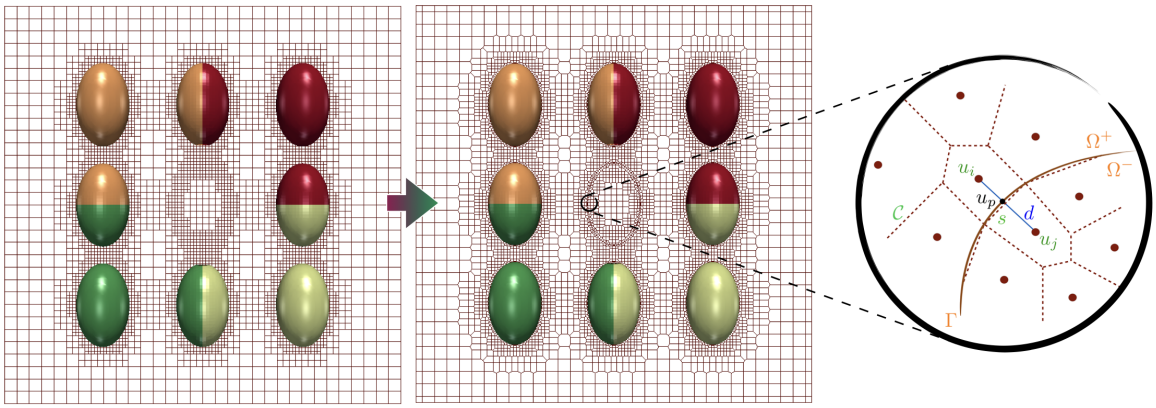

Figure 3.6: *(left to middle) An Octree is converted into an adaptive Voronoi mesh such that Voronoi faces are fitted to the interface. In our framework the computational domain is partitioned among different processors as demonstrated by different cell colors. (right) In our discretization, u_p corresponds to the normal projection of nodes i and j on the interface (Γ). This point is equidistant to nodes i and j. s is the common length (or area in 3D) of the interface between cells i and j. d is the distance between i and j.*

The main difficulty in solving the equations of section 3.3.2 is related to the non-trivial boundary conditions and discontinuities across the cells' surface. Guittet *et al.* [87] introduced the Voronoi Interface Method (VIM) to solve elliptic problems with discontinuities on irregular interfaces. Their proposed method exhibits second order accuracy by solving the problem on a Voronoi mesh instead of the given Cartesian grid. Also, Guittet *et al.* [70] extended the VIM to the case of the electropermeabilization problem including the aforementioned non-trivial boundary condition in the discretization. In this work, we implement their modified approach in parallel. In this section we briefly highlight this technique.

The solver presented by Guittet *et al.* [87] is based on building a Voronoi mesh using

the freely available library `Voro++` [88]. The Poisson equation is then solved on a Voronoi mesh that coincides with the irregular interface. This introduces additional degrees of freedom close to the interface and on either side that are equidistant to the interface by design. Briefly, the procedure for converting an initial adaptive Cartesian mesh to a conforming Voronoi mesh starts by adopting the Cartesian nodes as cell centers, *i.e.* known as Voronoi seeds, for a Voronoi mesh covering the computational domain. Next, if a Voronoi cell crosses the interface we replace the corresponding degree of freedom with a pair of equidistant points on either sides of the interface. This procedure provides a conforming Voronoi tessellation of the domain such that interfaces are tiled with collections of faces from adjacent Voronoi cells. For more details on generating the Voronoi mesh we refer the interested reader to [87]. Here, we present the numerical scheme of Guittet *et al.* [70] for completeness using the nomenclature given in Figure 3.6.

First we discretize the boundary condition (4.6c) using a standard Backward Euler scheme:

$$C_m \frac{[u]^{n+1} - [u]^n}{\Delta t} + S^n [u]^{n+1} = (\sigma \partial_n u^{n+1})_\Gamma, \tag{3.7}$$

which can be rearranged to get the membrane voltage jump:

$$[u]^{n+1} = \frac{C_m [u]^n + \Delta t (\sigma \partial_n u^{n+1})_\Gamma}{C_m + \Delta t S^n}, \tag{3.8}$$

In the second step, we discretize the continuity in the electric flux boundary condition (4.6b):

$$\sigma^e \frac{u_p^e - u_i^e}{d/2} = \sigma^c \frac{u_j^c - u_p^c}{d/2}, \tag{3.9}$$

Replacing u_p^c by its definition $u_p^e - [u]^{n+1}$ in the above expression, coupling it with equation

(3.8) and rearranging the terms, the final expression of u_p^e reads:

$$u_p^e = \left(\sigma^e u_i^e + \sigma^c u_j^c + \frac{\sigma^c C_m \left[u\right]^n}{C_m + \Delta t S^n} + \frac{\sigma^c \sigma^e \Delta t}{(C_m + \Delta t S^n) d/2} u_i^e \right) / \left(\sigma^c + \sigma^e + \frac{\sigma^c \sigma^e \Delta t}{C_m + \Delta t S^n) d/2} \right), \tag{3.10}$$

This equation for u_p^e is then included in the discretization of the Laplace equation on the Voronoi cells. Finally, we get the following expression for the potential around the interface:

$$\sum_{k \in \{\partial \mathcal{C} \backslash \Gamma\}} s_k \sigma^e \frac{u_k^e - u_i^e}{d_k} + s\hat{\sigma} \frac{u_j - u_i}{d/2} = \text{sign}(\phi_i) s\hat{\sigma} \frac{C_m \left[u\right]^n}{(C_m + \Delta t S^n) d/2}, \tag{3.11}$$

where

$$\hat{\sigma} = \frac{\sigma^c \sigma^e}{\sigma^e + \sigma^c + \frac{\sigma^e \sigma^c \Delta t}{(C_m + \Delta t S^n) d/2}}, \tag{3.12}$$

and "sign" refers to the signum function. This discretization leads to a positive definite linear system as all coefficients are positive and the jump appears only on the right-hand side of this system. We emphasize that the points far from the interface are discretized according to a standard finite volume discretization on the Voronoi grid. Integrations are performed with the geometric approach of Min and Gibou [**?**]. Note that finite volume discretizations are flexible with respect to spatial variations of the Voronoi mesh topology as they only utilize values on adjacent Voronoi cell centers, as well as values of the jump on the faces midway between pairs of Voronoi cells around the interface. Despite finite difference discretizations, this aspect circumvents challenges that arise when treating the faces between coarser and finer grids.

3.5 Numerical Results

3.5.1 Qualitative results

First, we present numerical results illustrating the capabilities of our approach in capturing the interaction between the cell membrane and the applied electric field. Electric fields provide a feedback channel for the cell membranes to interact over long distances and leads to environmental dependence of electropermeabilization within the aggregate environment.

Second, to demonstrate this effect on a biologically relevant construct and to showcase the computational capabilities of our approach, we consider the case of a spherical aggregate of cells confined in the center of a computational box of size $1mm$ on each side. The volume fraction of cells is set to $n = 0.13$ corresponding to $27,440$ well-resolved cells. The minimum distance between each pair of cells is set to $3 \times R_0$ where R_0 is the average radius of a cell. At present, we only intend to randomly distribute the spheroids with varying eccentricities and orientations. Therefore, this minimum threshold was adopted conservatively to avoid overlap between cells. A denser configuration would require to account for the orientation of each neighboring cell to be able to fill the free space more compactly.

The different parameters defining the geometry and properties of the cells are tabulated in table 3.1. The computational configuration used to run this simulation is tabulated in table 3.2. The resulting cell aggregate is illustrated in figure 3.7, with figure 3.5.1 depicting the electric potential (the aforementioned u field) across the domain and figure 3.5.1 showing the partitioning between the 2048 processors (identified with different colors - for visualization purposes, every adjacent 8 processors are displayed with same color). Figure 3.8 provides a cross section of the domain as well as a zoom that demonstrates that the cells are well-resolved.

Property	Symbol	Value	Units
Average cell radius	R_0	7	μm
Cell geometric parameters range			
Cell radii	r_0	0.57-1.43 $\times R_0$	μm
semi-axes	a, b, c	0.8-1.2 $\times R_0$	μm
Membrane electric parameters			
Capacitance	C	9.5×10^{-3}	F/m^2
Extracellular conductivity	σ^e	15	S/m
Intracellular conductivity	σ^c	1	S/m
Voltage threshold for poration	V_{ep}	258×10^{-3}	V
Membrane surface conductivity	S_0	1.9	S/m
Porated membrane conductance	S_1	1.1×10^6	S/m^2
Permeabilized membrane conductance	S_2	10^4	S/m^2
Poration timescale	τ_{ep}	10^{-6}	s
Permeabilization timescale	τ_{perm}	80×10^{-6}	s
Resealing timescale	τ_{res}	60	s
Threshold for poration	X_{ep}	0.5	-
Imposed electric pulse			
Electric field magnitude	$\lvert\boldsymbol{E}\rvert$	40	kV/m

Table 3.1: *Parameters of our simulation.*

Property	Value
Macromesh in x,y & z directions $n_x \times n_y \times n_z$	$2 \times 2 \times 2$
Minimum/Maximum levels of refinement (l_{min}, l_{max})	2×9
Total number of voronoi cells	$224,218,754$
Total number of nodes	$194,666,253$
Number of processors	2048
Total time of simulation	≈ 9 hours
Number of timesteps	44
Total physical time of the simulation	2.25 (μs)

Table 3.2: *Computational aspects of our simulation.*

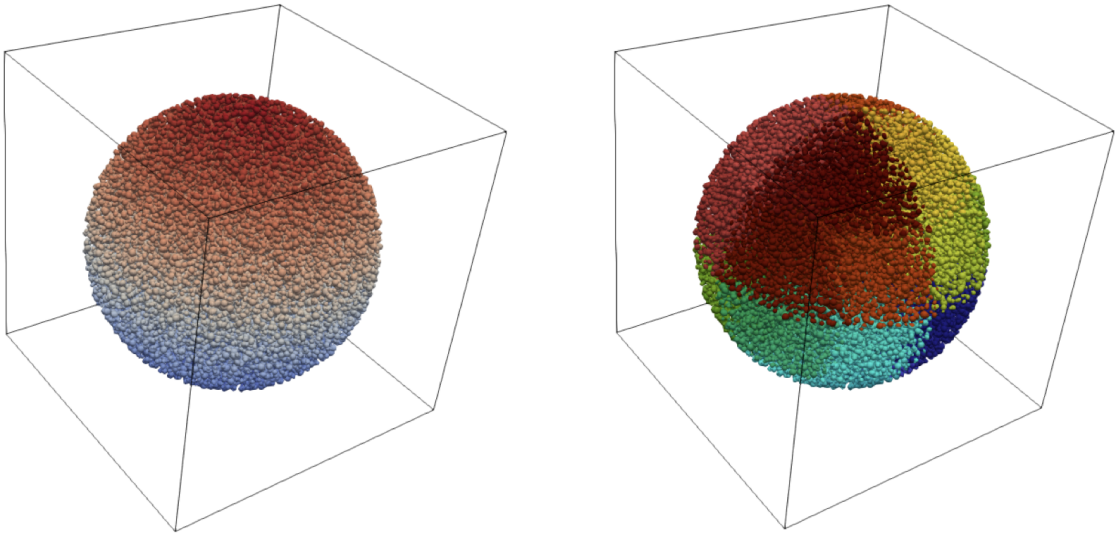

Figure 3.7: *Illustration of a cell aggregate immersed in an external electric field. (left) colors represent the electric potential of the membranes with red being higher intensities and blue lower intensities. We note that we have set the absolute value of the bottom potential to "0" (ground state) while the top electrode is at our desired potential difference. (right) partitions used in this simulation. Each color represents a group of 8 processors used in this simulation.*

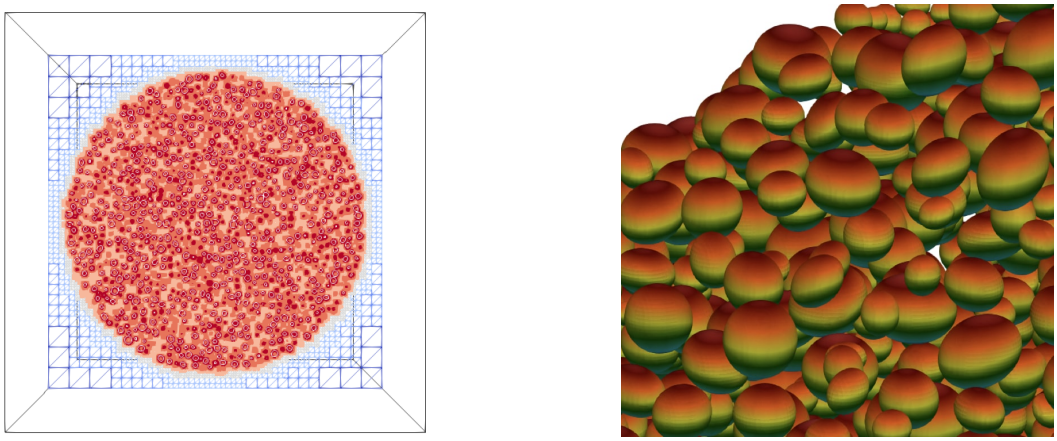

Figure 3.8: *Zoom into the simulation results. (left) A cross section of the simulation box. The cells are distributed uniformly throughout the cell aggregate. The color corresponds to the leaf-levels in the Octree data structure. (right) A zoom into the simulation box, cells are colored by their transmembrane potential difference.*

3.5.2 Convergence test and mesh independence

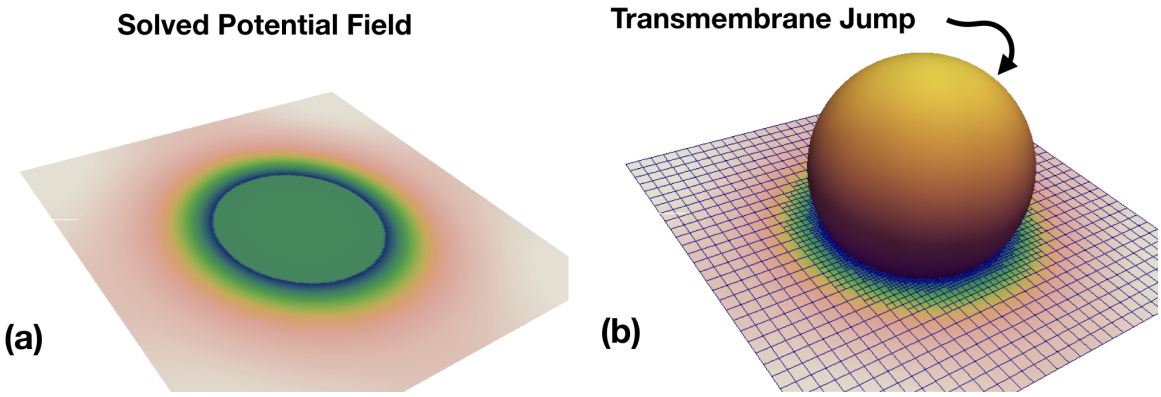

Figure 3.9: *The configuration used for convergence tests. (a) A circular cross section of the cell demonstrates how the electric potential field experiences a jump when passing through the interface. (b) The jump is measured on the Octree mesh by first extrapolating solutions on each side to the opposite side and then subtracting the extrapolated values on the nodes around the interface.*

To validate the numerical reliability of our implementation, we investigate the spatio-temporal convergence of the transmembrane potential jump, which is the key variable that couples the electropermeabilization equations. For this purpose, we consider a single spherical cell and track the evolution of the transmembrane potential jump $[u]$ at a $\pi/4$ radian distance from the cell's equator over time. Figure 3.9 illustrates the setup used for this purpose, as well as the refined mesh used. We use the dynamic linear case with $S = S_L$, for which the transmembrane jump, $[u]$, satisfies:

$$C\frac{\partial [u]}{\partial t} + S_L[u] = \sigma_c \frac{\partial u}{\partial \boldsymbol{n}}. \tag{3.13}$$

In this case, the exact solution is available for our validations and reads:

$$[u](t,\theta) = \frac{A}{S_L - B} g \left(1 - e^{-\frac{S_L - B}{C} t}\right) \cos(\theta), \tag{3.14}$$

where $g = ER_2$ and θ is the polar angle measured from the north pole. Also, A and B are given by:

$$K^{-1} = R_1^3(\sigma_e - \sigma_c) + R_2^3(2\sigma_e + \sigma_c), \tag{3.15a}$$

$$A = 3\sigma_c \sigma_e R_2^2 K, \tag{3.15b}$$

$$B = -\sigma_c \sigma_e (R_1^2 + \frac{2R_2^3}{R_1} K). \tag{3.15c}$$

In our tests, we use $R_1 = 50\mu m$ and $R_2 = 600\mu m$.

We perform the spatial and temporal refinements separately. First, we compare the results from simulations with different timesteps at a fixed resolution level of $(\mathrm{l_{min}}, \mathrm{l_{max}}) = (3, 7)$. In figure 3.5.3 we show how the jump converges as we decrease the time step by a factor of 2 each time. We performed our simulations with time steps of $\Delta t =$

1×10^{-8} $(s), 2 \times 10^{-8}$ $(s), 4 \times 10^{-8}, 8 \times 10^{-8}$ (s) and only for the linear case also with 1.6×10^{-7} (s). This is because in the nonlinear case the latter time step is too big to capture the width of the peak in the jump profile. Also, in figure 3.5.3 we increase the maximum refinement level while keeping the minimum refinement level fixed at $\mathrm{l_{min}} = 3$ and the time step constant at $\Delta t = 2 \times 10^{-8}$ (s); these are plotted with solid lines. Additionally, we perform identical simulations while simultaneously increasing both the minimum and maximum levels of refinements; these are shown with dashed lines. This is motivated by the observation that the solid lines in figure 3.5.3, corresponding to a fixed $\mathrm{l_{min}} = 3$, converge to the exact solution at slower rate than the dashed lines. Maintaining low $\mathrm{l_{min}}$ while enhancing resolutions at the interface does not improve accuracy because errors produced at coarser grids far from interface become dominant in the simulation box, making further refinements useless when considering the error in the maximum norm. Even though both cases demonstrate convergence, increasing both the minimum and maximum refinement levels naturally exhibits a better convergence behavior.

We also demonstrate that for the full nonlinear dynamic case, the convergence of our numerical results is achieved both in time and space in figures 3.5.3 and 3.5.3 respectively. In the nonlinear case, we choose a constant electric field intensity of $E = 40kV/m$ across the domain in the z-direction. The size of the domain is $400\mu m$ in each spatial dimension. For the temporal convergence, we performed our simulations at fixed resolution levels of $(3, 7)$ and for the spatial convergence we picked a fixed timestep of $\Delta t = 2 \times 10^{-8}(s)$ while varying the maximum refinement level.

In the nonlinear case, convergence in time seems more problematic. As noted in [70], this is expected due to the highly nonlinear temporal nature of the equations, while the equations are spatially well-behaved. This implies that smaller timesteps are preferable over finer spatial resolutions for decreasing the numerical errors. Hence, we observe the system's response converges both in linear and nonlinear cases. We also note that in real

case simulations that we perform the timestep is determined after setting the mesh at the desired resolution levels. Then in each simulation, the time-step is determined from $\Delta t = \Delta \boldsymbol{x}_{min}/dt_{scaling}$.

3.5.3 Performance and scalability of the approach

We show a simple test of the performance of the parallel approach for real applications of interest. We solve the same cell aggregate problem introduced in section 3.5 on different numbers of processors while keeping all other parameters fixed. This test captures the full problem complexity and hence enables a reasonable assessment of the computational efficiency and scalability of the approach. Constructing the Voronoi mesh at each time step and solving the linear system arising from the discretization introduced in section 3.4.5 constitute the bulk of the computational expense of our approach. Figure 3.11 demonstrates that our approach tackles these tasks excellently up to 4096 processors, which is the upper limit to our current account on the "Stampede2" supercomputer.

In figure 3.11, we also show the scaling test for a smaller cell density in order to demonstrate the capabilities of our implementation at lower problem sizes, where communication overhead easily exceeds that of computational time. Interestingly, we find that our approach exhibits excellent scalability even for quite small problems.

We should emphasize that parallelization is only one avenue to simulating larger problems in our methodology. Another significant aspect is the use of adaptive mesh refinement using Octree grids. This introduces a significant reduction in the size of the grid from $\approx 2^{30}$ nodes to $194,666,253$ nodes in this example. We refer the interested reader to [1] for a quantitative study of this enhancement. This consequently advances the limits of the possible simulation scales with the current state-of-the-art available resources.

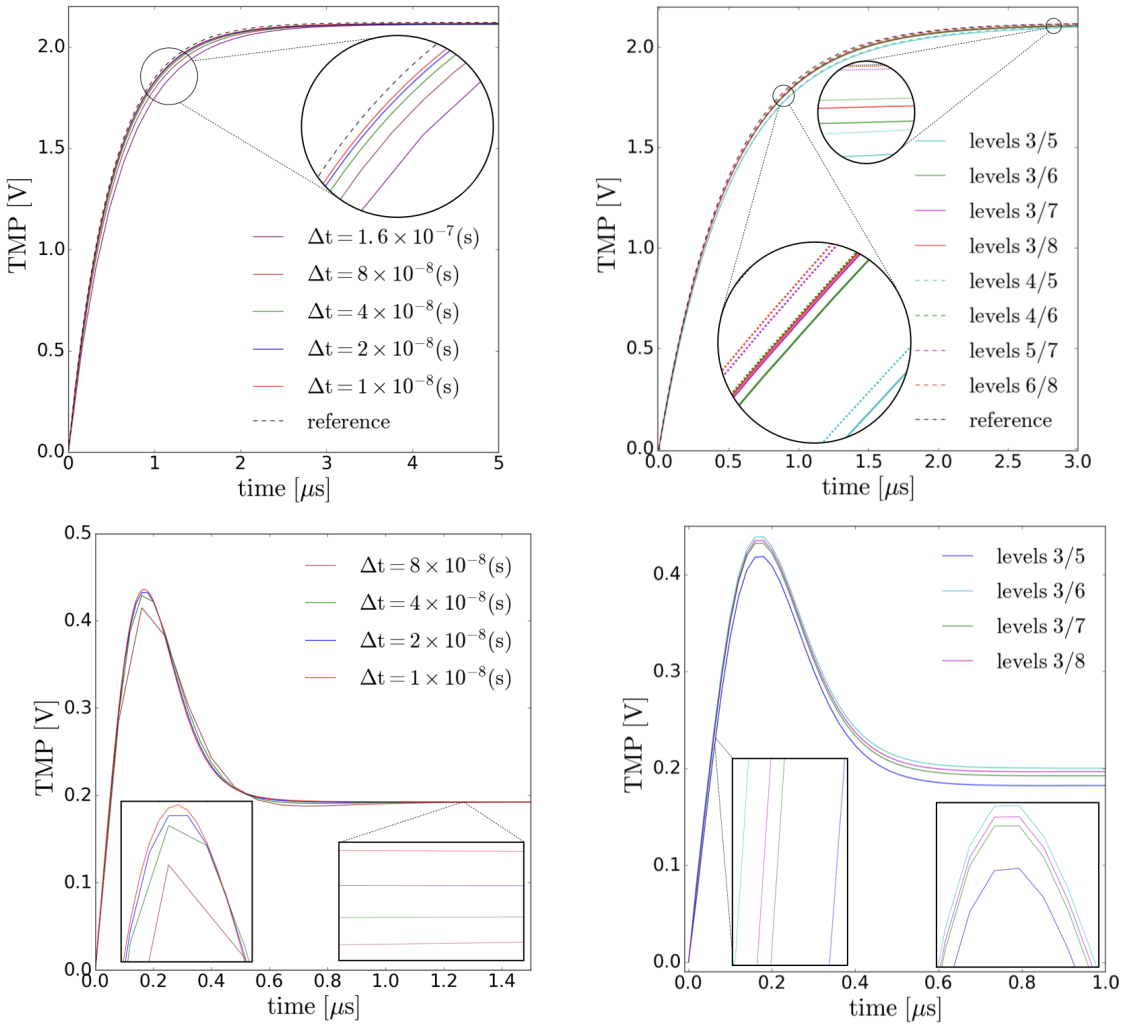

Figure 3.10: *Convergence analysis of section 3.5.2. Figure (a) illustrates the temporal convergence of the TMP for five different time steps at a fixed grid size. Figure (b) demonstrate convergence in space consistent with the exact solution. Figures (c,d) are the temporal and spatial convergence for the full nonlinear case, respectively. Zoom-in figures are included in each plot for clarity.*

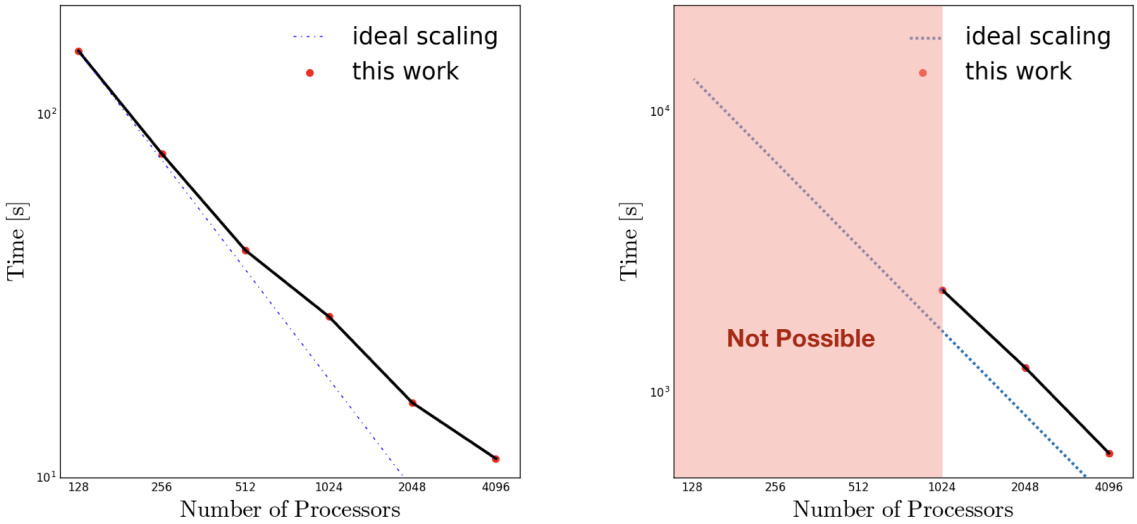

Figure 3.11: *Scaling of the wall-clock time when increasing the number of processing cores. In both cases, the size of the problem is fixed and only the number of processors varies. The ideal scaling is shown with the dashed blue line. Our algorithms scale well for both small and large simulations. (left) A small simulation with* $2,837,427$ *nodes at levels (2,9) containing 313 biological cells. (right) Large aggregate with over* $228,000,000$ *nodes containing* $31,320$ *biological cells. In this case it is not possible to simulate large aggregates on small number of processors due to memory limitations, which we refer to as "Not Possible".*

3.6 Mesoscale Phenomenology

Cell aggregates are complex systems composed of many cells that each follow a set of principles and collectively reach an equilibrium state with their environment. Cell aggregates exhibit emergent phenomena [89], *i.e.* "novel and robust behaviors of a system that appear at the limit of some parameter in the system" [90, 91]. In our case, a weak form of emergence appears at some finite limit of system size. These novel features are robust against certain details at the smaller scales of the aggregate; viz. in the sense that via the process of coarse-graining the renormalized parameters describing theories at different scales *always* converge to certain fixed values in natural systems (cf. [92]). This generic feature of complex systems is recognized as a fundamental principle of nature

[93]. Recently the descriptive framework that arises by relying on this aspect of complex systems has been discussed by [5, 6].

In the study of complex systems, computational strategies provide powerful or in some specific cases the *only* method to exploit the so called "weak emergent" phenomena, first described by Bedau 2002 [94]. Weak emergence is attributed to those physical aspects of complex systems that, in practice, only appear through computer simulations. This is due to the nonlinearity of the micro-level equations and the complex interactions between its constituent parts. For a comprehensive review of this topic we refer the interested reader to Fulmer *et al.* [95].

As in most large-scale numerical simulations, our main purpose is to study the non-local effects that are not already encoded *locally* in the governing partial differential equations, but are encrypted in the spatial domain as a whole and influence the overall behavior via feedback processes among elements. In the case of electroporation, such influences are in part due to the heterogeneous cell topologies, long range electrostatic interactions, and the overall shape of the aggregate among other factors. In this section, we aim to show that macro-level features of cell aggregates are recovered in our methodology. We first demonstrate the influence of cell shape on the macro-level properties of the aggregate, and will present first results for a tumor-like aggregate.

3.6.1 Effect of biological cell shape

Biological cells come in different shapes. We place three simple types of cells in the same experimental setup and compare their bioelectric behavior. To this end, we choose to place oblate, spherical and prolate cells with identical volume on a $7 \times 7 \times 7$ regular lattice. Figure 3.12 shows the configurations used in our experiments, and the effect of cell shape is compared in figure 3.13. One can observe that cells with prolate topology

exhibit higher levels of permeabilization, spheres fall in between and oblate spheroids are the least electroporated. This is consistent with previous reports of [70], and may be due to higher effective cross section area exposed to the influx of the electric field.

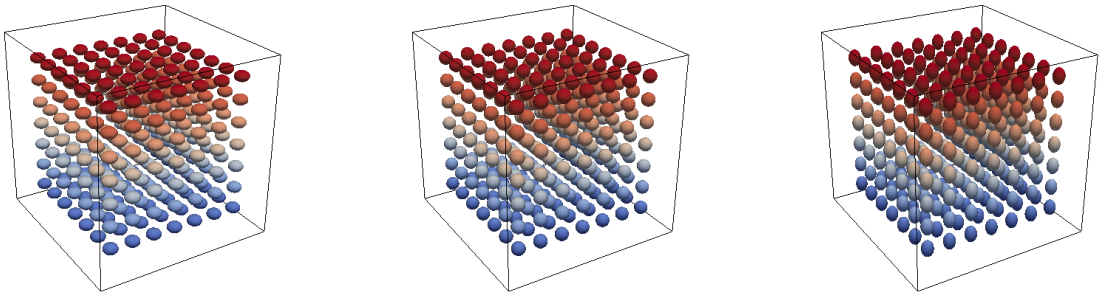

Figure 3.12: *Arrays of cells used in section 3.6.1. (left) oblates, (middle) spheres, and (right) prolates with equal volumes.*

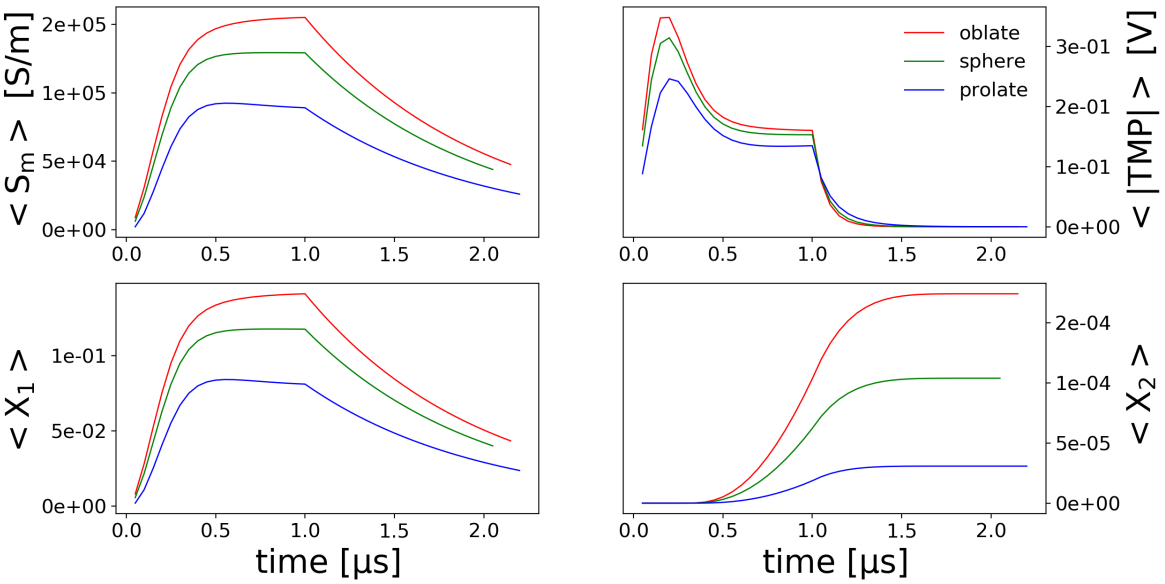

Figure 3.13: *Effect of cell shape on the parameters of the electroporation model.*

3.6.2 Shadowing effect

Shadowing refers to the adverse effect of upstream cells to the permeabilization levels exhibited by their downstream counterparts. We performed experiments on a controlled sample of 125 spherical cells in a cubic lattice centered in a bounding box with twice the size of the lattice. We place cells symmetrically in a $5 \times 5 \times 5$ array as depicted in figure 3.6.2. We compare the surface average of X_2 parameter over the surface of all cells in the top, center, and bottom rows. The results are given in figure 3.6.2.

As expected the middle row is less permeabilized, and cells closer to the electrodes (in this specific configuration) exhibit higher levels of permeabilization. In particular, this observation is in accordance with the experimental data of spheroid electroporation of Rols *et al.* [96]. Note that owing to the reflection symmetry, top and bottom slices are in identical environments, this is also reflected by the overlapping measurements for their permeabilization curves as in figure 3.6.2.

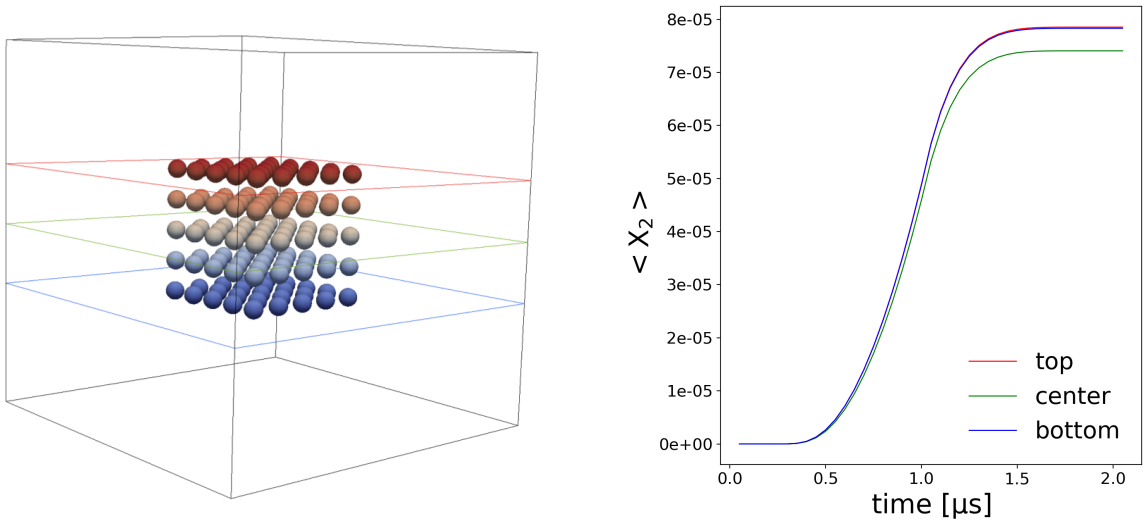

Figure 3.14: *Shadowing effect.*

So far we have only considered regular lattice configurations, in the remaining of this

work, we focus on the tumor-like demonstration case that is depicted in figure 3.7. To date, studying computationally this relevant biological structure is only possible with the computational approach introduced in this manuscript.

3.6.3 Electroporation fraction

In experiments, one can measure the fraction of cells that are electropermeabilized more than a detectable threshold. In order to compare our numerical results with experiments, we set the minimum detectable threshold for electropermeabilization to different values:

$$\mathrm{S_m} \geq (100 \text{ or } 1,000 \text{ or } 10,000 \text{ or } 100,000)\mathrm{S_L}.$$

Then, we measure the fraction of total electropermeabilized surface area of all cells normalized by the total surface area of the cells.

Figure 3.15 depicts the permeabilization pattern throughout a dense suspension (volume fraction of 13%), and figure 3.16 quantifies the evolution of the membrane electropermeabilization fraction. Remarkably, we observe that the maximum value of this fraction under a short $40kV/m$ electric pulse reaches $\approx$ 70%, 65%, 50% and 5% for the given thresholds respectively. This is in qualitative agreement with the experimental results of Pucihar *et al.* [97].

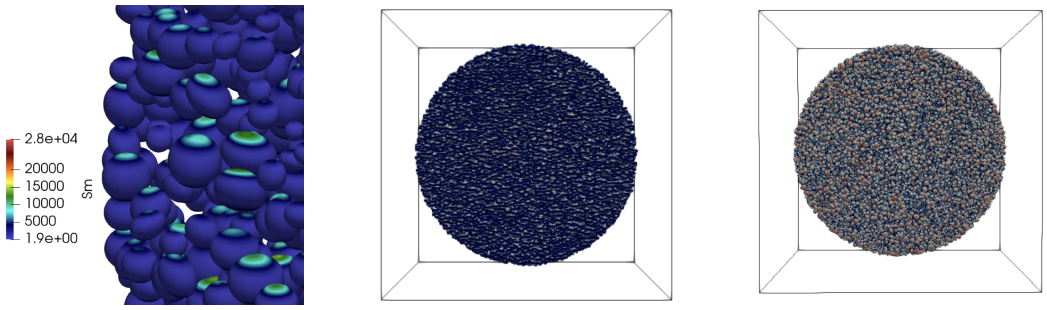

Figure 3.15: *Permeabilization pattern in a heterogenous aggregate. (a) Cells are mostly permeabilized along their vertical (z-) axis, (b) is a side view of the aggregate, and (c) is a top-view of the cell aggregate. Hotter colors represent higher values of cell membrane conductance.*

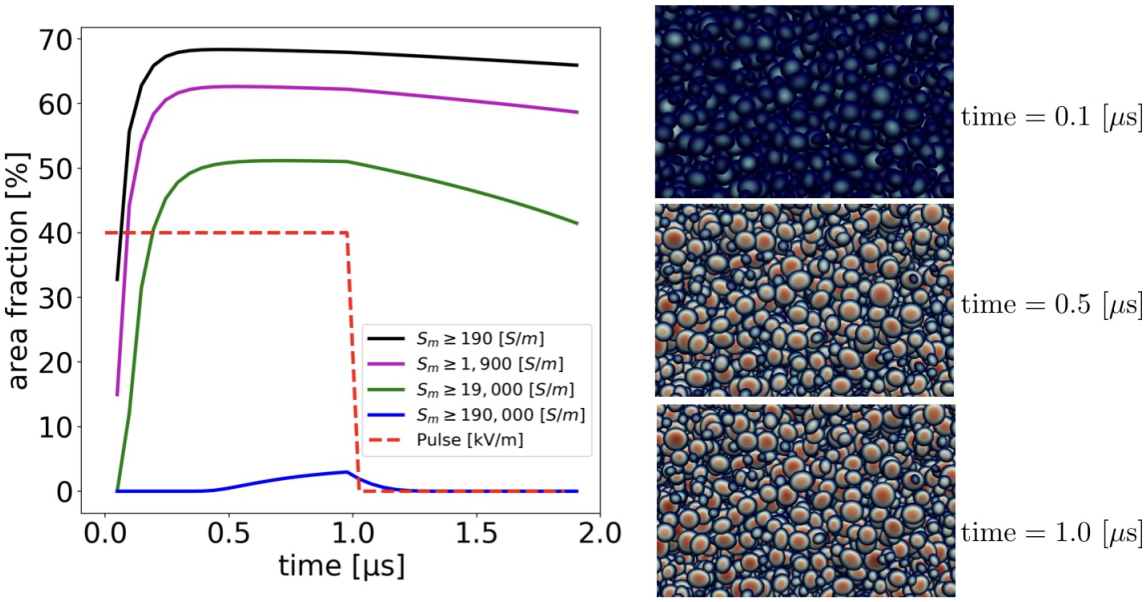

Figure 3.16: *Electropermeabilization fraction over time for a $1\mu s$ square pulse of $40kV/m$. Figures on the right panel are color coded by conductance, with hotter colors encoding higher conductance levels.*

The evolution of the relevant electropermeabilization parameters including membrane conductance (S_m), level of membrane poration (X_1), level of membrane permeabilization (X_2) and absolute value of the transmembrane potential (TMP) are shown in figure 3.17 for reference. One observation is that the transmembrane voltage does not vanish

spontaneously after the external pulse is turned off; this is due to the capacitive nature of the cell membranes that maintain a slowly vanishing electric field in the environment.

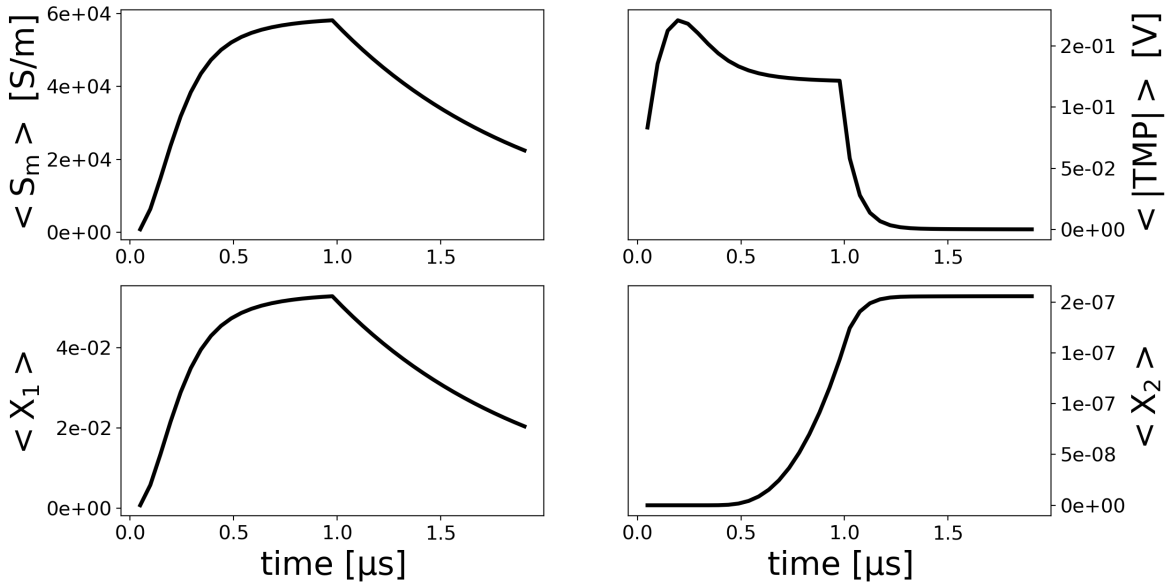

Figure 3.17: *Time evolution of relevant parameters averaged over the membranes of the* $27,440$ *cells in our simulations. The applied pulse is turned off at* $1\mu s$.

The signature of the nonlinear model underlying the evolution of the transmembrane voltage is also evident in these figures. We present three snapshots of the transmembrane potential in the aggregate in figure 3.18. These snapshots capture the initial overshoot in the transmembrane voltage (cf. figure 3.17) and then the saturation phase that follows. These snapshots are color coded according to the transmembrane potential.

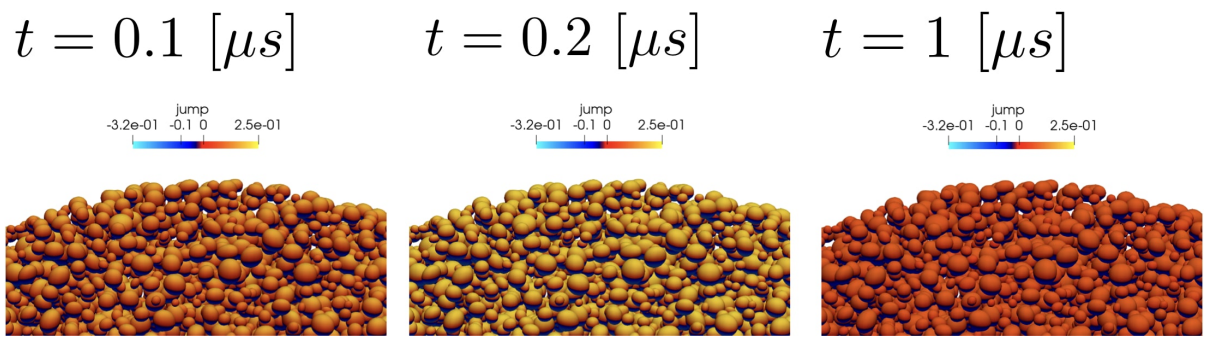

Figure 3.18: *Time evolution of the transmembrane potential in a cell aggregate. Hotter colors correspond to higher values of transmembrane voltage.*

3.6.4 Impedance of the aggregate

In these simulations we apply a constant and uniform potential difference between the electrodes. The electric field will adapt to the geometrical configuration of the domain as well as the cells, while the cell membranes also distort the field. The distortions in the observed electric field close to the boundaries, where the electrodes are located, produce a different profile for the "needle potential" that the cell aggregate experiences. Needle intensity is defined as:

$$I(t) = \int_{\mathcal{E}_1} \sigma^e \partial_{\boldsymbol{n}} V(t,x) \cdot \boldsymbol{n} ds, \tag{3.16}$$

where $\mathcal{E}$ is one of the electrodes where the voltage is imposed. The evolution of the needle intensity for the tumor-like aggregate is shown in figure 3.6.4.

Furthermore, one can measure the overall permeability within the environment by measuring the impedance of the sample detected at the electrodes. We define the impedance of the cell aggregate as:

$$Z(t) = \frac{\int_{\mathcal{E}_{1-2}} V(t,x) ds / \int_{\mathcal{E}_1} ds}{\int_{\mathcal{E}_1} \sigma \partial_{\boldsymbol{n}} V(t,x) \cdot \boldsymbol{n}\, ds}, \tag{3.17}$$

where $\mathcal{E}_1$ and $\mathcal{E}_2$ are either the top or the bottom electrode, and $\mathcal{E}_{1-2}$ is the difference of the integral between $\mathcal{E}_1$ and $\mathcal{E}_2$ electrodes. Note that the exact choice of labels does not change the result due to continuity of current through the medium.

The time evolution of the impedance of the aggregate is shown in figure 3.6.4. Comparison with figure 3.17 suggests a strong negative correlation between impedance and the overall degree of permeability. We find that even though permeabilized cells have a huge increase of their membrane conductance (from 1 to 10^4 S/m^2), as illustrated in figure 3.17, the relative impedance of the aggregate drops about $\approx 0.15\%$ after $1\mu s$ of a constant external electric pulse.

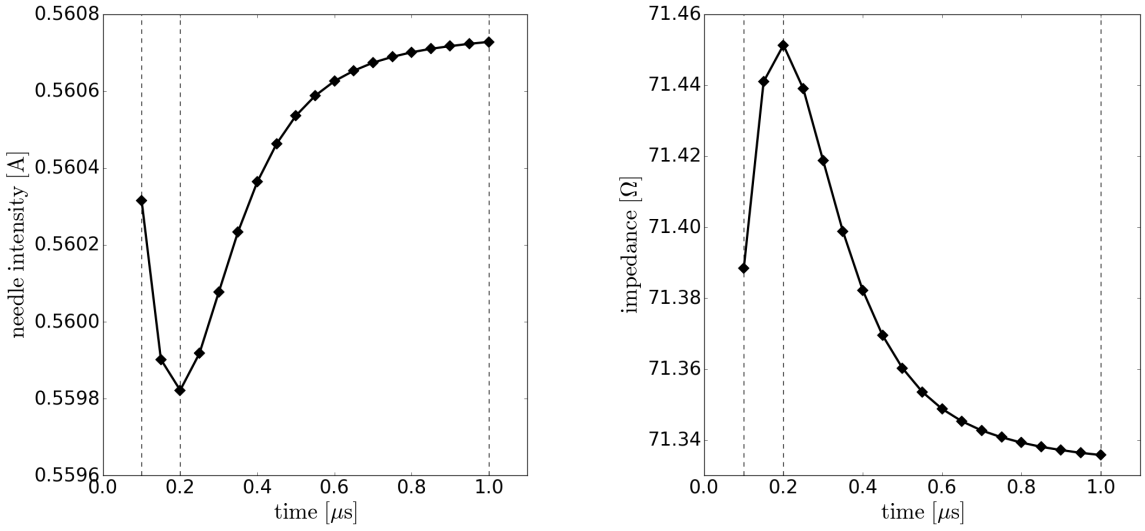

Figure 3.19: *(left) time evolution of the needle intensity, as well as (right) the resulting aggregate impedance under a constant external potential difference. Vertical dashed lines mark the times $t = 0.1$ $[\mu s]$, $t = 0.2$ $[\mu s]$ and $t = 1$ $[\mu s]$ for which the corresponding transmembrane voltages are visualized in figure 3.18.*

3.7 Conclusion

We have presented a computational framework for parallel simulations of cell aggregate electropermeabilization at the mesoscale. We used an adaptive Octree/Voronoi

mesh along with a numerical treatment that preserves the jump in the electric potential across each cell's membrane. The core aspects of our methodology are its efficiency and excellent scalability, making it possible to consider meaningful simulations of tumor-like spheroids, as opposed to previous serial approaches that were not able to go beyond micro-scale simulations. We have presented preliminary numerical results on cell aggregate electropermeabilization that are in qualitative agreement with experimental observations. This work thus paves the way for a wide range of comparisons with biological experiments, as it makes possible the multiscale understanding of electroporation from the cell to the tissue.

Acknowledgement

The research of P. Mistani, A. Guittet and F. Gibou was supported by NSF DMS-1620471 and ARO W911NF-16-1-0136. C. Poignard research is supported by Plan Cancer DYNAMO (ref. PC201515) and Plan Cancer NUMEP (ref. PC201615). P. Mistani would like to thank Daniil Bochkov in the CASL group for fruitful discussions that have contributed to this research. This work used the Extreme Science and Engineering Discovery Environment (XSEDE), which is supported by National Science Foundation grant number ACI-1053575. The authors acknowledge the Texas Advanced Computing Center (TACC) at The University of Texas at Austin for providing HPC and visualization resources that have contributed to the research results reported within this paper. This research was performed in part within the scope of the Inria associate team NUM4SEP, between the CASL group at UCSB and the Inria team MONC. C.P.'s research is partly performed within the scope of the European Associated Laboratory EBAM on electroporation, granted by CNRS.

Chapter 4

On the interfacial polarization of heterogeneous systems

4.1 abstract

We present a theoretical framework to model the electric response of cell aggregates. We establish a coarse representation for each cell as a combination of membrane and cytoplasm dipole moments. Then we compute the effective conductivity of the resulting system, and thereafter derive a Fokker-Planck partial differential equation that captures the time-dependent evolution of the distribution of induced cellular polarizations in an ensemble of cells. Our model predicts that the polarization density parallel to an applied pulse follows a skewed t-distribution, while the transverse polarization density follows a symmetric t-distribution, which are in accordance with our direct numerical simulations. Furthermore, we report a reduced order model described by a coupled pair of ordinary differential equations that reproduces the average and the variance of induced dipole moments in the aggregate. We extend our proposed formulation by considering fractional order time derivatives that we find necessary to explain anomalous relaxation phenomena

observed in experiments as well as our direct numerical simulations. Owing to its time-domain formulation, our framework can be easily used to consider nonlinear membrane effects or intercellular couplings that arise in several scientific, medical and technological applications.

4.2 Introduction

Effects of external electric fields on heterogeneous systems have been of great scientific and technological importance throughout the past century. These systems include composite materials, colloidal suspensions, and biological cells. In the case of biological cells, electric fields have found several applications for cell fusion [98, 99], electrorotation [100, 101], dielectrophoresis [102, 103] and cancer cell separation [104, 105], electroporation [106], levitation [107] and cell deformation [108]. For an early review of its applications in biotechnology and medicine we refer to Markx and Davey (1999) [109]. More recently, transmembrane potential (TMP) patterns that emerge in multicellular living organisms have gained extra attention due to discovery of their regulatory role in development and regeneration; we refer to the review of Levin *et al.* (2017) for a comprehensive overview on developmental bioelectricity [110]. Even though modern research on TMP manipulations are focused on molecular based treatments, it has been long known that TMP patterns altered by external electric fields could influence development [111], embryogenesis [112, 113] or wound healing [114]. Therefore, developing a predictive and generalizable mathematical model to understand the effects of different cellular mechanisms on the tissue level bioelectric patterns poses promising opportunities in bioengineering.

In all of these applications, it is essential to have a precise knowledge of the TMP induced over cell membranes, especially in cell aggregates that are composed of tens

of thousands of cells with a heterogeneous mix of morphologies and electrical properties. Even though much is known about single cell electric interactions, a theory that predicts a detailed distribution of transmembrane potentials within cell aggregates has been missing. In this work, we present a novel theoretical framework based on a Fokker-Planck description, for tracing the time evolution of the probability density of multicellular polarizations in response to arbitrary electric stimulations. We further introduce a moment-based analytic reduced-order model of the proposed Fokker-Planck equation that provides statistics of transmembrane potentials with minimal computational expense. Importantly, besides multicellular systems, our theory is applicable to a broad range of systems such as shelled colloidal particles, emulsions and composite materials [115]. Moreover, it can be extended to include the effects of membrane nonlinearities [3] or intercellular couplings [116], counterion polarizations, and eventually real-time pulse optimization, which is of great benefit to emerging biomedical treatments using electric fields such as electrochemotherapy.

4.2.1 Physical bioelectric processes

Electrical properties of biological tissues have been extensively investigated for the last two centuries since the discovery of Ohm's law. A comprehensive historical overview of different aspects of biological dielectric response (including basic concepts, tabulated data, underlying molecular processes and effective cellular interactions) is covered in the surveys of Schwan (1957) [117], Stuchly and Stuchly (1980) [118], Pethig (1984) [119], Pethig and Kell (1987) [120], Foster and Schwan (1989) [121], McAdams and Jossinet (1995) [122], Gabriel (1996) [123], Kuang and Nelson (1998) [124], with more recent reviews on its different applications such as electroporation provided by Kotnik *et al.* (2019) [125].

Early research on the electric response of bulk biological materials revealed that tissues exhibit resistive and capacitive behaviors. Experiments showed an early peak in current in response to a step voltage, which could be attributed to an increasing tissue resistance, or from an induced counter-potential polarization. Furthermore, with the advent of high frequency apparatus it was possible to examine the high frequency response of tissues, which led to the recognition that tissues exhibit low resistance at higher frequencies and the dielectric response of tissues was determined by different physical processes at each frequency regime. Bulk electric properties are mainly determined by cell membranes and cellular structures. At the cellular level, three main physical processes, namely interfacial polarization, ionic diffusion and dipolar orientation of polar molecules, are identified to play key roles in dielectric dispersions at different frequency regimes [117]. While the origin of α- and γ-dispersions are relaxation processes in the bulk phases of the material, β-dispersions originate from internal boundary conditions imposed by interfaces separating different phases; this is the focus of the current work. Below, we briefly review these mechanisms.

• α-dispersion: The main factor that contributes to the *α-dispersion* (at audio or sub-KHz frequencies) is the ionic diffusion in the electric double layer in the immediate vicinity of charged surfaces as well as in the bulk. α-dispersion is characterized with high dielectric constants at low frequencies. Schwan first observed this mode of polarization at low frequencies in biological tissues [117] and later, Schwan and co-workers showed that this effect is also observed in non-biological colloids [126]. Schwarz (1962) [127] was the first to develop a theory that took into account the counterion polarization around colloidal particles suspended within electrolytes. Schwarz showed these displacements could be modeled by an additional "apparent" dielectric constant that reach high values at low frequencies. Schwarz's method did not consider diffusion in the double layer itself, and was later extended by Einolf and Carstensen (1971) [128, 129] to include diffusion

on both sides of the membranes. Dukhin and Shilov (1974) [130] proposed a more accurate treatment by considering ionic diffusion in the bulk, rather than just the thin layers around charged particles (see also the review by Mandel and Odijk [131]). A simplified formulation of Dukhin's model that admits analytical solution was given by Grosse and Foster [132], which helped to show that the corresponding Cole-Cole plot is broader than the Debye's model, indicating that counter-ion polarization is partly responsible for the observed anomalous relaxation of biological matter. In short, counter-ion polarization theories explain α-dispersion and predict high permittivities at low frequencies that exhibit broad relaxation behaviors.

• β-dispersion: Interfacial polarization dominates the dielectric properties of tissues at *β-dispersion* (radio frequencies from tens of KHz to tens of MHz range, timescales determined by membrane resistance and capacitance) as well as the dielectric properties of colloids and emulsions. Biological mixtures of interest to us have a *triphasic* dielectric structure with conductive parts composed of a cytoplasm covered by a membrane immersed in a continuous medium. Historically, dielectric theories of interfacial polarization began by considering *diphasic suspensions* in the seminal treatise of Maxwell (1873) [133] and later Wagner (1914) [134]. In 1925, Fricke [135] developed a dielectric theory for spherical particles surrounded by nonconductive membranes and extended it to membrane-covered ellipsoidal particles in 1953 [136]. Maxwell-Wagner theory has the following limitations: (i) it is only valid at very low concentrations and assumed that the local electric field was equal to the external electric field, (ii) the interior of particles were assumed to be at constant potential, and (iii) the external field was modeled as if the particle was a perfect insulator. Hanai (1960) [137] developed an interfacial polarization theory that was valid at high concentrations, by assuming Wagner's relation holds during successive additions of infinitesimally small quantities of the disperse phase. Hanai and co-workers (1979) [138] later generalized their approach to the case of suspensions

of shelled spheres and Zhang *et al.* (1983-1984) [139, 140] showed that the theory could explain experiments with polystyrene microcapsules. This strategy was applied to three-phase structures in 1993 [141]. We shall emphasize that even though Hanai's approach is advantageous over Wagner's theory as it holds its validity to high concentrations, it is still based on the non-conductive assumption for membranes and, more importantly, it is not clear how to consider nonlinear variations in the membrane conductance during the application of electric pulses similar to the case of electroporation. Our theory builds on this line of work and aims to address these shortcomings by constructing a time-domain model for interfacial polarization in cell aggregates. Unlike the aforementioned works that are limited to modeling average properties at the aggregate level, our approach captures detailed information about the distribution of induced polarizations as well as their time-dependent evolution.

• γ-dispersion: The third mechanism that is responsible for the γ-*dispersion* (microwave frequencies from MHz to GHz range) is the dipolar orientations of permanent polar molecules, *e.g.* water molecules and other macromolecules. Under an applied electric torque and opposed by thermal agitations in the medium, polar molecules undergo rapid reorientations towards thermal equilibrium and exhibit dielectric relaxation. This phenomenon is described by Debye's theory (1929) [142], which is inherently a Fokker-Planck equation that describes the evolution of the probability density of dipolar orientations under an applied pulse. Our theory presented here is inspired by this strategy.

4.2.2 Equations of interfacial polarization

In its general form, Maxwell's equations in matter read

$$\nabla \cdot \mathbf{D} = \rho_f \tag{4.1}$$

$$\nabla \cdot \mathbf{B} = 0 \tag{4.2}$$

$$\nabla \times \mathbf{E} = -\partial_t \mathbf{B} \tag{4.3}$$

$$\nabla \times \mathbf{H} = \mathbf{J}_f + \partial_t \mathbf{D} \tag{4.4}$$

where E and B are the electric and magnetic fields, respectively, $\mathbf{D} = \epsilon\mathbf{E}$, $\mathbf{H} = \mu\mathbf{B}$ and the total current is defined by $\mathbf{J} = \mathbf{J}_\mathrm{f} + \partial_\mathrm{t}\mathbf{D}$. However, electric interactions within a multicellular system can be modeled under the *quasi-electrostatic* assumption, *i.e.* when the wavelength of the stimulating electric pulse is larger than the cell size. Under the quasi-electrostatic assumption, the induced magnetic fields are negligible and therefore the electric field is curl free and we may define the electric potential u by the relation $\mathbf{E} = -\nabla\mathrm{u}$. Also, computing the divergence of (4.4) and using (4.1), we have that $\nabla \cdot (\sigma\nabla\mathrm{u}) = \dfrac{\partial\rho_\mathrm{f}}{\partial\mathrm{t}}$, where in the absence of a net free charge density ρ_f, when only interfacial polarization is present, the electric field is given by the solution of the Laplace equation $\nabla \cdot (\sigma\nabla\mathrm{u}) = 0$, and we can neglect the permittivity of the cytoplasm and of the extra-cellular medium.

As for cells, we consider a shelled particle model with two concentric surfaces $\Gamma^{\pm}$ forming a membrane with thickness h (see figure 4.1). The boundary conditions impose that the electric potential must be continuous across the interfaces

$$u_c(\mathbf{x}^-) = u_m(\mathbf{x}^-), \qquad u_m(\mathbf{x}^+) = u_e(\mathbf{x}^+),$$

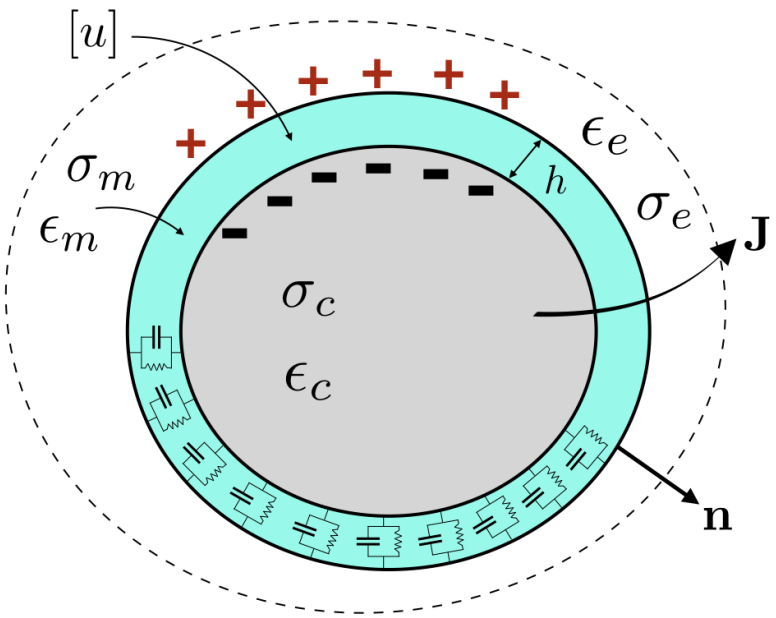

Figure 4.1: *Cell membranes are modeled with an array of parallel resistors and capacitors in a thin layer surrounding the cytoplasm. Here we consider a sharp interface.*

with $\mathbf{x}^{\pm} \in \Gamma^{\pm}$ and that the normal component of the total current $\mathbf{J}_{\mathrm{k}} = (\sigma_{\mathrm{k}} + \mathrm{j}\omega\epsilon_0\epsilon_{\mathrm{k}})\mathbf{E}_{\mathrm{k}} = \Lambda^*_{\mathrm{k}}\mathbf{E}_{\mathrm{k}}$ (with $\mathrm{k} = \mathrm{e}, \mathrm{m}$ and c referring to the extra-cellular medium, the membrane and the cytoplasm, respectively) must be continuous across the boundaries:

$$\Lambda^*_c \partial_n u_c(\mathbf{x}) = \Lambda^*_m \partial_n u_m(\mathbf{x}), \qquad \mathbf{x} \in \Gamma^-,$$
$$\Lambda^*_m \partial_n u_m(\mathbf{x}) = \Lambda^*_e \partial_n u_e(\mathbf{x}), \qquad \mathbf{x} \in \Gamma^+.$$

Note that $\mathbf{E}_{\mathrm{m}} \cdot \mathbf{n} = -[\mathrm{u}]/\mathrm{h}$. This set of equations have been considered by Miles and Robertson (1932) [143] for a single sphere. We further assume a thin membrane by setting $\mathrm{h}/\mathrm{R}_1 \to 0$. The exact response of the TMP to a step pulse for an isolated sphere with constant membrane conductance has been studied by many authors [144, 145, 146, 147, 148]. Even though these equations are not solved for arbitrary cell geometries, Kotnik & Miklavćić [149] provide analytical solutions for the TMP over oblate and prolate cells

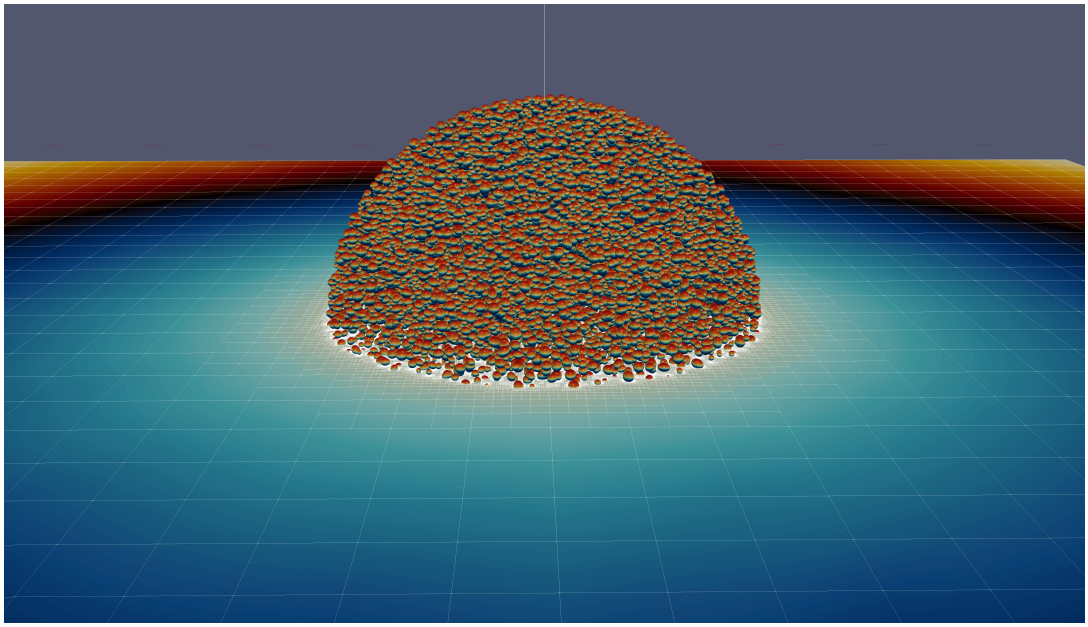

Figure 4.2: *A snapshot of the* 3D *spherical tumour composed of* $\sim 30,000$ *random cells considered in this work. Cells are colored according to their TMP values, with redder colors indicating higher positive TMP while bluer colors indicate lower negative TMP. The Octree data structure is shown on an equatorial slice to emphasize the enhanced resolutions close to cell membranes.*

in the special case where the cell's axes of symmetry is parallel to the applied field. Qualitatively, they have shown that the maximum TMP increases with the equatorial radius of spheroids, *i.e.* the radius perpendicular to the applied field. The authors considered an insulating membrane to simplify the analysis; however it was shown in experiments that this is not a valid assumption [150] and one has to consider changes in membrane poration and permeabilization under an applied pulse. This re-structuring of cells membrane under an electric field can be considered, for example, by adopting a nonlinear phenomenological model for the membrane conductance [68]:

$$S_m(t,[u]) = S_L + S_1 X_1(t,[u]) + S_2 X_2(t,[u]), \tag{4.5}$$

where S_0, S_1 and S_2 are the conductance values of the membrane in the resting, po-

rated and permeabilized states, respectively. In this model, the level of poration and permeabilization of the membrane are captured in the functions X_1 and X_2, which are calculated as a function of the TMP by solving a set of nonlinear ordinary differential equations. Overall, we therefore adopt the following boundary value problem to model electric interactions in charge-free mixtures,

$$\nabla \cdot (\sigma(\mathbf{x})\nabla u) = 0, \qquad \mathbf{x} \in (\Omega_c \cup \Omega_e) \tag{4.6a}$$

with boundary conditions,

$$[\sigma(\mathbf{x})\partial_n u] = 0 \qquad \mathbf{x} \in \Gamma, \tag{4.6b}$$

$$C_m \partial_t [u] + S(t, [u])\,[u] = \sigma(\mathbf{x})\partial_n u \qquad \mathbf{x} \in \Gamma, \tag{4.6c}$$

$$u(t, \mathbf{x}) = g(t, \mathbf{x}) \qquad \mathbf{x} \in \partial\Omega, \tag{4.6d}$$

and homogeneous initial condition,

$$u(0, \mathbf{x}) = 0 \qquad \mathbf{x} \in \Omega \tag{4.6e}$$

where we used $[\boldsymbol{o}] = \boldsymbol{o}_e - \boldsymbol{o}_c$ to describe the jump operator across the interface Γ in the normal direction, σ_c, σ_e and σ_m are the conductivities of the cytoplasm, the extra-cellular medium and the cell membrane, respectively. Note that $\sigma_\mathrm{m} \equiv \mathrm{S_m h}$ and $\epsilon_0\epsilon_\mathrm{m} \equiv \mathrm{C_m h}$ are membrane conductivity and permittivity, respectively.

4.2.3 Direct numerical simulations

Numerical simulations can be used to directly investigate tissue-level properties of cell aggregates emerging from the set of equations 4.6a–4.6e along with (4.5), when considered

in a large heterogeneous environment. However, several computational challenges need to be addressed in order to obtain guaranteed accuracy and convergence of the numerical results, while simultaneously considering large enough number of cells. Particularly, imposing jump conditions on numerous irregular sharp interfaces requires efficient numerical discretization methods along with scalable parallel computing algorithms for mesh generation and storage as well as advanced linear system solvers and preconditioners.

In this vein, Guittet *et al.* (2016) [87] introduced the Voronoi Interface Method (VIM) to solve Elliptic problems with discontinuities across the interface of irregular domains. Basically, VIM utilizes an interface-fitted Voronoi mesh before applying the dimension-by-dimension Ghost Fluid Method [151]. Importantly, VIM produces a linear system that is symmetric positive definite with only its right-hand-side affected by the jump conditions. The solution and the solution's gradients are second-order accurate and first-order accurate, respectively, in the L_∞-norm. Later, Guittet *et al.* (2017) applied VIM to the case of cell electroporation [70] in a serial computing environment. Recently, Mistani *et al.* (2019) [2] extended these results to parallel computing environments and considered a large tumour spheroid composed of $\sim 30,000$ ellipsoidal cells. Figure 4.2 illustrates a snapshot of this simulation with the transmembrane potentials depicted over cell membranes. This simulation leveraged the suite of data structures and routines provided by the Portable, Extensible Toolkit for Scientific Computation (`PETSc`) [152, 153, 154] using the Bi-CGSTAB solver [155] over the linear system preconditioned by `hypre` [156] library. Creation and management of adaptive octree grids was handled by `p4est` software library [157] along with `voro++` [158] library for building an adaptive Voronoi tessellation from the underlying Octree grid.

To our knowledge, the direct numerical simulations employed in this work present the current state-of-the-art for large scale simulations of electric interactions at the level of cell aggregates. We believe the simulation results provide precise information about

electric response of cell aggregates. In this manuscript we leverage the insights drawn from this direct numerical simulation data to develop and corroborate a theory for the time-dependent evolution of the TMP in cell aggregates under arbitrary applied electric pulse.

4.2.4 Multiscale modeling strategy

Given the microscopic model of the electric interactions (4.6a)-(4.6e), we aim to infer effective theories at the multicellular level where tens of thousands of cells are present. In our work we focus on the effective properties of the aggregate using the *effective medium theory*, for example see [159], accompanied with a dynamical model for the transient response of the system to an external pulse using the *Fokker-Planck formalism* [160, 161]. Below, we briefly describe and justify each component of our modeling strategy.

• Effective medium theory: Maxwell (1873) [133] was the first to study effective transport properties of a stationary, random and homogeneous suspension of spherical particles dispersed in a background medium of uniform conductivity. Maxwell's assessment of effective conductivity was accurate to order $\mathcal{O}(\phi)$ (ϕ is the volume fraction of particles) and relied on his observation that changes in effective conductivity of a suspension of particles was due to the average dipole moment of particles. Exactly a century later, Jeffrey (1973) [162] expanded Maxwell's estimation to order $\mathcal{O}(\phi^2)$ using the general method of Batchelor (1972) [163, 164] by considering pairwise interactions between spherical particles. Batchelor's work was focused on studying the effects of hydrodynamic interactions between particles moving at low velocity through a fluid on the effective viscosity of a suspension of particles. A remarkable result of his work was finding the second order correction term to Einstein's result for the effective viscosity of a suspension of dilute particles by systematically considering pairwise hydrodynamic interactions between

freely-moving spheres in a linear flow field.

As part of the work presented here, we apply Batchelor's approach to the problem of conductive shelled spheres instead of the "homogenization" method that emerged in the 80's and is more commonly used in similar application domains, *e.g.* in cardiac electrophysiology [165, 166]. Our choice is motivated by several reasons: (i) as was pointed out by Hinch (2010) [167], homogenization techniques are limited to periodic microstructures, which makes them less applicable for modeling finite size multicellular systems like tumor spheroids, (ii) presenting this problem in Batchelor's formalism allows for application of several existing results such as the influence of the particles' shape and arrangement on the effective conductivity of cell aggregates (even at maximum packing fractions with touching spheres), the consideration of both near- and far-field interactions between particles, as well as the effects due to higher-order multipole moment interactions of particle polarizations on the overall conductivity; we refer the interested reader to Batchelor (1974) [168], Bonnecaze & Brady (1990) [169] and the references therein for more details. Lastly, (iii) Batchelor's method is based on ensemble averages of interactions among dispersed particles, that implicitly assumes indistinguishability of particles, which is in line with the Fokker-Planck formalism that we present next.

• Fokker-Planck formalism: Cells in an aggregate are heterogeneous in shapes and electrical properties. Therefore, under an applied electric field, the evolutionary path of a cell's polarization is different from that of other cells, necessitating a probabilistic description of the induced polarizations. To this end, we describe the state of the multicellular system with the probability density of induced dipole moments on membranes and cytoplasms. We then derive a Fokker-Planck equation (FPE) that describes the time evolution of the state-space probability density in response to an electric pulse, as well as the many non-thermal small disturbances that influence the states. Therefore, the Fokker-Planck equation not only provides the stationary state of the system, but also

predicts its dynamics far from equilibrium. The Fokker-Planck equation was first used by Fokker (1914) [160] and Planck (1917) [161] and have been used to describe numerous systems such as the statistics of laser lights, or the rotations of dipole moments under various potentials. The latter was carried out by Debye who derived a Fokker-Planck equation for the rotational dynamics of polarized molecules and is used to describe the γ-dispersion discussed in section 4.2.1. We refer to Risken (1984) [170] for a standard exposition of this topic, and to [171] for an overview of applications in sciences and engineering.

The basic idea of our treatment is to modify the boundary conditions on the cell membranes in order to add appropriate disturbances to the system parameters, which in turn provides a Langevin equation for the induced dipole moment. Then, we transform the Langevin equation to its corresponding Fokker-Planck partial differential equation. Finally, we reduce the governing FPE by using a moment-based approach and derive a simple set of ordinary differential equations (ODEs) that captures the evolution of the average and of the variance of induced polarizations. Importantly, the set of ODEs is simple enough that it can be used for real-time predictions and control of transmembrane potentials under arbitrary external electric stimulations and system parameters.

The plan of this manuscript follows: in section 4.3 we use Green's theorem to decompose cellular polarization into its different components and compute effective conductivity of the medium. In section 4.4 we use the continuity of flux across cell membranes to develop a Langevin equation for the evolution of membrane polarization, thereafter we perturb the physical parameters in this model and after standard averaging procedure we obtain the corresponding Fokker-Planck equation. We provide an analytic treatment of the governing FPE and leverage a moment based approach to compute the reduced order ODE system for the statistical moments of the induced polarization density. Also, we argue in favor of a fractional order for time derivative in the FPE. Finally, in section

4.5 we present numerical results of our model both in the time domain and frequency domain. We conclude our work in section 4.6.

4.3 Coarse-grained representation

Our strategy is to use a multipole generator scheme to represent the surface current density on individual cell membranes in terms of an equivalent set of dipole moments that reproduce an identical potential in a homogenized medium.

4.3.1 Cells as arrays of layer potentials

We denote by $\mathrm{u}(\mathbf{r})$, the electric potential at any point $\mathbf{r}$ within the aggregate; $\mathrm{u}(\mathbf{r})$ satisfies Laplace's equation. We treat this problem by viewing a membrane as a dipole layer (*cf.* see chapter 1 of [172] for more details) that is formed by two infinitesimally close surfaces with opposite charge densities, as depicted in figure 4.1. In this work we only consider a passive environment, *i.e.* that is free from current source or sink terms on cell membranes, and denote the passive current by $\mathbf{J}_{\mathrm{m}}$. In this case, we can relate the normal current density passing through the membrane by $\mathbf{J}_{\mathrm{m}}^{\pm} \cdot \mathbf{n}$ (where $\pm$ refers to the external and internal side of the membrane) to the potential jump across membrane by writing

$$-\mathbf{J}_m^{\pm} \cdot \mathbf{n} = \sigma_c \partial_{\mathbf{n}} u_c = \sigma_e \partial_{\mathbf{n}} u_e, \tag{4.7}$$

Similar to Geselowitz [173], we use Green's theorem to treat this problem in terms of source current densities and applied electric fields surrounding the domain. Consider two well-behaved functions ψ and ϕ defined inside and outside of cells and define the vector field $\mathbf{F} = \sigma\psi\nabla\phi$ such that it is a continuous function of position in enclosed

volumes between boundaries. Substituting $\mathbf{F}$ in Gauss's theorem and wrapping thin membranes with discontinuity in between two close surfaces, one obtains Green's theorem for non-homogeneous mixtures with discontinuity across internal boundaries (see page 53 of [174]),

$$\begin{aligned}
&\sum_{j=1}^{q} \int_{A_j} [\sigma_c(\psi_c \nabla \phi_c - \phi_c \nabla \psi_c) - \sigma_e(\psi_e \nabla \phi_e - \phi_e \nabla \psi_e)] \cdot d\mathbf{A}_j \\
&+ \sum_{j=1}^{p} \int_{A_j} \sigma(\psi \nabla \phi - \phi \nabla \psi) \cdot d\mathbf{A}_j \\
&= \int_V [\psi \nabla \cdot (\sigma \nabla \phi) - \phi \nabla \cdot (\sigma \nabla \psi)] dv
\end{aligned}$$

where q is the number of surfaces across which σ is discontinuous, p is the number of additional boundaries including macroscopic boundaries where electrodes are located, and V is the volume enclosed between Γ and all inner surfaces A_j excluding surfaces of discontinuity. Here we adopt a convention that $d\mathbf{A}_j$ is the measure of an area element of the surface A_j that always points into the extra-cellular matrix.

Geselowitz, in his case *I*, considers $\psi = 1/r$ and $\phi = u$ with r being the distance between surface or volume elements to any arbitrary point in the domain. Then it is straightforward to show that for any observation point $\mathbf{x}$ in the aggregate, we have

$$\begin{aligned}
4\pi u(\mathbf{x}) = &\sum_m \int_{A_m} (\sigma_e u_e - \sigma_c u_c) \nabla'(\frac{1}{r}) \cdot d\mathbf{A} \\
&+ \int_\Gamma \left(\frac{\mathbf{J}_b}{\sigma_e r} + u_b \nabla' \frac{1}{r} \right) \cdot d\mathbf{A},
\end{aligned}$$

where Γ is the surface of the electrodes, u_b is the electric potential applied at the electrodes, $\mathbf{J}_b = -\sigma_e \nabla u$, and A_m is the surface of membranes that points into the extra-cellular matrix. Moreover, as in case *II* of Geselowitz, we could let $\psi = 1/r$ and $\sigma\phi = u$

to show that for infinitesimally thin membranes the electric potential is given by:

$$4\pi u(\mathbf{x}) = \sum_m \int_{A_m} \left[\left(\frac{1}{\sigma_e} - \frac{1}{\sigma_c} \right) \frac{\mathbf{J}_m^{\pm}}{r} + [u] \nabla' (\frac{1}{r}) \right] \cdot d\mathbf{A} + \int_\Gamma \left(\frac{\mathbf{J}_b}{\sigma_e r} + u_b \nabla' \frac{1}{r} \right) \cdot d\mathbf{A}, \tag{4.8}$$

Hence, using the divergence theorem one can obtain the alternative formulation:

$$4\pi u(\mathbf{x}) = \sum_m \int_{A_m} [u] \nabla' (\frac{1}{r}) \cdot d\mathbf{A}_m + \sum_c \int_{V_c} \left(\frac{1}{\sigma_e} - \frac{1}{\sigma_c} \right) \mathbf{J} \cdot \nabla' (\frac{1}{r}) dV + \int_\Gamma \left(\frac{\mathbf{J}_b}{\sigma_e r} + u_b \nabla' \frac{1}{r} \right) \cdot d\mathbf{A}, \tag{4.9}$$

where $\mathbf{r} = |\mathbf{x} - \mathbf{x}'|$, $\nabla' = \partial / \partial \mathbf{x}'$ and the summation is over the membranes of the enclosed cells within Γ. The first term on the right-hand side describes the influence of the polarized membranes, the second term captures the contribution from the cytoplasms, and the last term represents the influence of electrodes. We also emphasize that if the electrodes are not in direct contact with the extra-cellular matrix (e.g. there is a gap with low conductivity between Γ and the outer surface of the aggregate), one has to also include the extra contribution from the outer surface ($\mathbf{A}_o$),

$$u_o(\mathbf{x}) = \frac{1}{4\pi} \int_{A_o} \frac{2\mathbf{E}_o}{r} \cdot d\mathbf{A}.$$

In addition to the contribution from the electrodes, equation (4.8) decomposes the electric potential at any point in the volume as a superposition of a monopole/single layer and a dipole layer on each membrane. Remarkably, the membrane integral over transmembrane

jump is analogous to the contribution from a surface current dipole density:

$$u_p(\mathbf{x}) = \sum_m \frac{1}{4\pi\sigma_e} \int_{\mathbf{A}_m} D(\mathbf{x}')\nabla'\left(\frac{1}{r}\right) \cdot d\mathbf{A}_m$$

where the current dipole surface density (*i.e.* current times distance between sources) is defined by:

$$D(\mathbf{x}) = \sigma_e[u]$$

Then, a point dipole on the membrane is expressed as $\delta\boldsymbol{P} = \sigma_e[u]d\mathbf{A}_m$ and one may model the induced transmembrane potential as a resultant current dipole on each cell.Thus, we approximate each membrane with surface A_i by a resultant dipole of strength

$$\mathbf{P}_i = \int_{A_i} \sigma_e[u]d\mathbf{A}, \tag{4.10}$$

and we call $\mathbf{P}$ the *dipolar polarization*.

Furthermore, we observe that the membrane integral over the transmembrane current density resembles the contribution from a *monopole current layer*,

$$\begin{aligned} u_s(\mathbf{x}) &= \sum_m \frac{1}{4\pi} \int_{\mathbf{A}_m} \left(\frac{1}{\sigma_e} - \frac{1}{\sigma_c}\right) \frac{\mathbf{J}_m^{\pm}}{r} \cdot d\mathbf{A}_m \\ &= \sum_m \frac{1}{4\pi\sigma_e} \int_{\mathbf{A}_m} (\sigma_c - \sigma_e) \frac{\mathbf{E}_c}{r} \cdot d\mathbf{A}_m \end{aligned}$$

where $\mathbf{E}_c$ refers to the electric field at the inner surface of the membrane. Here, we identify an induced polarization density of $(\sigma_c - \sigma_e)\mathbf{E}_c \cdot \mathbf{n}/(4\pi\sigma_e)$ over cell membranes.

Alternatively, this term in its volume integral form reads

$$u_s(\mathbf{x}) = \sum_c \frac{1}{4\pi\sigma_e} \int_{V_c} (\sigma_c - \sigma_e)\mathbf{E} \cdot \nabla'\big(\frac{1}{r}\big) dV,$$

which can be interpreted as an 'extra flux density', denoted by $\boldsymbol{\tau}$ and is zero everywhere in the extra-cellular matrix while in the cells is given by

$$\begin{aligned} \boldsymbol{\tau}(\mathbf{x}) &= (\sigma_c - \sigma_e)\mathbf{E} \\ &= \mathbf{J}(\mathbf{x}) + \sigma_e \nabla u(\mathbf{x}). \end{aligned}$$

Hence

$$u_s(\mathbf{x}) = \sum_c \frac{1}{4\pi\sigma_e} \int_{V_c} \boldsymbol{\tau}(\mathbf{x}') \cdot \nabla'\big(\frac{1}{r}\big) dV,$$

which again resembles the electric potential of a volume dipole density $\boldsymbol{\tau}$. Therefore, we define the *instantaneous polarization* ($\mathbf{S}$) to model the polarization of cell cytoplasms:

$$\mathbf{S}_i = \int_{V_i} \boldsymbol{\tau} dV,$$

or, equivalently, in terms of the potential in the cytoplasmic side of the membrane as

$$\mathbf{S}_i = (\sigma_e - \sigma_c) \int_{A_i} u_c \; d\mathbf{A}.$$

Then the net polarization can be defined by $\mathbf{M}_i$

$$\mathbf{M}_i = \mathbf{P}_i + \mathbf{S}_i = \int_{A_i} (\sigma_e u_e - \sigma_c u_c) \; d\mathbf{A}$$

We also note that this result could be directly inferred using Green's theorem by letting

$\phi = u$ and $\psi = 1/r$, *e.g.* see equation 29 of Geselowitz 1967. Furthermore one can relate the values of $\mathbf{P}$ and $\mathbf{S}$ through the equation:

$$\frac{\mathbf{P}}{\sigma_e} = \int_A u_e d\mathbf{A} + \frac{\mathbf{S}}{\sigma_c - \sigma_e} \tag{4.11}$$

We observe that in general the dipolar and instantaneous polarizations may have different orientations depending on the symmetries of the exterior potential. To assess this relation, we use Gauss' theorem for a closed surface Γ enclosing N internal closed surfaces (*cf.* see chapter III of Smythe, note the minus sign is due to our convention that the normal direction points into the extra-cellular matrix),

$$\sum_{j=1}^{N} \int_{A_j} u \; d\mathbf{A} + \int_{\Gamma} u \; d\mathbf{A} = - \int_{V_e} \nabla u \; dV, \tag{4.12}$$

where V_e is the volume of the extra-cellular matrix excluding cells. Therefore, for the cell aggregate

$$\frac{n < \mathbf{P} >}{\sigma_e} = \frac{\sum_{j=1}^{N} \int_{A_j} u \; d\mathbf{A}}{V} + \frac{n < \mathbf{S} >}{\sigma_c - \sigma_e}, \tag{4.13}$$

where,

$$n < \mathbf{P} >= \frac{\sum_{j=1}^{N} \mathbf{P}_j}{V} \quad \text{and} \quad n < \mathbf{S} >= \frac{\sum_{j=1}^{N} \mathbf{S}_j}{V},$$

with n the number density of cells in the mixture. Note that the volume fraction ϕ is related to the number density n via $\phi = nV_c$. Using Gauss law (4.12) with equation 4.13

we obtain

$$\frac{n < \mathbf{P} >}{\sigma_e} = \frac{n < \mathbf{S} >}{\sigma_c - \sigma_e} - \frac{1}{V}\int_{V_e} \nabla u \; dV - \frac{1}{V}\int_{\Gamma} u d\mathbf{A}.$$

Furthermore, we define the applied electric pulse on the boundary, $\mathbf{E}_{ext}$, as:

$$\mathbf{E}_{ext} \equiv \frac{1}{V}\int_{\Gamma} u d\mathbf{A}.$$

We also recall that $\mathbf{S}$ is related to the volume averaged electric field in cell cytoplasms by:

$$\phi \bar{\mathbf{E}}_c \equiv -\frac{1}{V}\sum_{j}^{cells}\int_{V_j} \nabla u \; dV = \frac{n < \mathbf{S} >}{\sigma_c - \sigma_e},$$

while the volume averaged external field is simply

$$\begin{aligned}(1-\phi)\bar{\mathbf{E}}_e &\equiv -\frac{1}{V}\int_{V_e} \nabla u \; dV \\ &= \mathbf{E}_{ext} + \frac{n < \mathbf{P} >}{\sigma_e} + \frac{n < \mathbf{S} >}{\sigma_e - \sigma_c}\end{aligned}$$

and the volume average electric field inside the membranes is related to the dipolar polarization by

$$\frac{1}{V}\sum_{j}^{cells}\int_{V_j'} \nabla u dV = \frac{1}{V}\sum_{j}^{cells}\int_{\Gamma_j} [u] d\mathbf{A} = \frac{n < \mathbf{P} >}{\sigma_e}.$$

Because the volume V is partitioned into three parts $V = V_e \cup V_c \cup V_c'$, where V_c' is the

volume occupied by cell membranes, we conclude that

$$\begin{aligned} - < \nabla u > &= \mathbf{E}_{ext} \\ &= \phi \bar{\mathbf{E}}_c + (1-\phi)\bar{\mathbf{E}}_e - \frac{n < \mathbf{P} >}{\sigma_e}. \end{aligned}$$

In particular, we note that $\phi V = \sum_j V_j$, and we define the dipolar polarization per cell volume as $\mathbf{p}_j = \frac{\mathbf{P}_j}{V_j}$ to obtain the effective dipole moment per cell volume,

$$\bar{\mathbf{p}} = \frac{\sum_j V_j \mathbf{p}_j}{\sum_j V_j},$$

and we can write

$$n < \mathbf{P} >= \phi \bar{\mathbf{p}}.$$

4.3.2 Frequency domain model for cell dipoles

We consider the analytical solution of a spherical cell of radius R_1 centered within a spherical domain of radius R_2 under a Dirichlet potential $E(t)R_2\cos\theta$ at the outer boundary (a *local* electric field $\mathbf{E} = -E\mathbf{k}$ is considered at the surface of a sphere of radius $r = R_2$ from center of the cell). In this case the membrane voltage satisfies

$$C_m \frac{\partial [u]}{\partial t} + (S_L - B)[u] = AE(t)R_2\cos\theta,$$

where

$$A = 3\sigma_c\sigma_e R_2^2 K \quad \text{and} \quad B = -\sigma_c\sigma_e(R_1^2 + 2\frac{R_2^3}{R_1})K,$$

with $K^{-1} = R_1^3(\sigma_e - \sigma_c) + R_2^3(2\sigma_e + \sigma_c)$ so the coefficients are:

$$A = \frac{3\sigma_c\sigma_e/R_2}{2\sigma_e + \sigma_c + \phi(\sigma_e - \sigma_c)},$$

and

$$B = -\frac{(2+\phi)\sigma_c\sigma_e/R_1}{2\sigma_e + \sigma_c + \phi(\sigma_e - \sigma_c)},$$

where the volume fraction of cells is given by $\phi = R_1^3/R_2^3$. Furthermore, we define three independent parameters that characterize the solution:

$$\begin{aligned}
\tilde{\sigma} &= 2\sigma_e + \sigma_c + \phi(\sigma_e - \sigma_c), \\
\eta &= 1 + \frac{S_L R_1 \tilde{\sigma}}{(2+\phi)\sigma_c\sigma_e}, \\
\tau &= \frac{\tilde{\sigma} R_1 C_m}{(2+\phi)\sigma_c\sigma_e}.
\end{aligned}$$

In the frequency domain the solutions are given by,

$$\begin{aligned}
[\tilde{u}] &= \frac{3R_1}{2+\phi} \cdot \frac{1}{\eta + j\omega\tau} \cdot \tilde{E}(\omega) \cdot \cos\theta \\
\tilde{u}_c &= \tilde{\alpha}_c \tilde{E}(\omega) \cdot r \cdot \cos\theta \\
\tilde{u}_e &= (\tilde{\alpha}_e r + \frac{\tilde{\beta}_e}{r^2}) \cdot \tilde{E}(\omega) \cdot \cos\theta
\end{aligned}$$

with

$$\begin{aligned}
\tilde{\alpha}_c &= \frac{3\sigma_e}{\tilde{\sigma}} \cdot \left(\frac{\eta - 1 + j\omega\tau}{\eta + j\omega\tau} \right) \\
\tilde{\alpha}_e &= \left(\frac{\sigma_c + 2\sigma_e}{\tilde{\sigma}} - \frac{3\sigma_c}{\tilde{\sigma}} \cdot \frac{\phi}{2+\phi} \cdot \frac{1}{\eta + j\omega\tau} \right) \\
\tilde{\beta}_e &= \left(\frac{\sigma_e - \sigma_c}{\tilde{\sigma}} + \frac{3\sigma_c}{\tilde{\sigma}} \cdot \frac{1}{2+\phi} \cdot \frac{1}{\eta + j\omega\tau} \right) \cdot R_1^3
\end{aligned}$$

The external and internal electric fields are computed given the electric potential ($\mathbf{r} = r\hat{r}$)

$$\tilde{\mathbf{E}}_e(\omega) = \tilde{\alpha}_e \tilde{\mathbf{E}}(\omega) - \frac{3(\tilde{\beta}_e \tilde{\mathbf{E}}(\omega) \cdot \hat{r})\hat{r} - \tilde{\beta}_e \tilde{\mathbf{E}}(\omega)}{r^3}, \tag{4.14}$$

and

$$\tilde{\mathbf{E}}_c(\omega) = \tilde{\alpha}_c \tilde{\mathbf{E}}(\omega), \tag{4.15}$$

which corresponds to a uniform external field superimposed by the electric field of a net dipole moment

$$\tilde{\mathbf{M}}(\omega) = -4\pi\sigma_e \tilde{\beta}_e \tilde{\mathbf{E}}(\omega). \tag{4.16}$$

It can be easily verified that indeed $u_e(R_2) = ER_2 \cos\theta$ as expected. We emphasize that we only impose the tangential component of electric field at $r = R_2$ and not its radial component, as evident by equation (4.14).

As we discussed before, we represent this solution by defining dipole moments over membranes and cytoplasms. It is straightforward to compute the dipole moments from the basic definitions of the previous section, which lead to

$$\frac{\tilde{\mathbf{P}}(\omega)}{V_c} = -\frac{3\sigma_e}{2+\phi} \cdot \frac{1}{\eta + j\omega\tau} \cdot \tilde{\mathbf{E}}(\omega) \tag{4.17}$$

and

$$\frac{\tilde{\mathbf{S}}(\omega)}{V_c} = -\frac{3\sigma_e(\sigma_e - \sigma_c)}{\tilde{\sigma}} \cdot \frac{\eta - 1 + j\omega\tau}{\eta + j\omega\tau} \cdot \tilde{\mathbf{E}}(\omega), \tag{4.18}$$

where V_c is the volume of a cell. One can verify that indeed we have $\tilde{\mathbf{P}} + \tilde{\mathbf{S}} \equiv \tilde{\mathbf{M}}$ from equation (4.16). Moreover, it is straightforward to verify that $\tilde{\mathbf{P}}$ and $\tilde{\mathbf{S}}$ are related through equation (4.11). We note the minus sign in dipole moments stems from our mathematical definition for jump in solution across membrane, that is the value of solution in the

exterior minus that of the cytoplasm, which is opposite the usual convention in biology. Therefore, in making the connection with other works, care must be taken in using consistent signs at this step. Note also that the influence of the membrane conductivity is captured in the parameter η. For example, for an insulating membrane where $\sigma_m \ll \sigma_c$, we have $\eta \approx 1$ and therefore the cell cytoplasm is effectively shielded from polarization in agreement with experiments, *i.e.* $\mathbf{S} = 0$.

Equations (4.17)–(4.18) enable the definition of the cellular polarizability coefficients $\mathbf{P} = \sigma_e \alpha_p \mathbf{E}$, $\mathbf{S} = \sigma_e \alpha_s \mathbf{E}$, and $\mathbf{M} = \sigma_e \alpha \mathbf{E}$ with

$$\alpha_p = -\frac{3}{2+\phi} \cdot \frac{1}{\eta + j\omega\tau},$$
$$\alpha_s = -\frac{3(\sigma_e - \sigma_c)}{\tilde{\sigma}} \cdot \frac{\eta - 1 + j\omega\tau}{\eta + j\omega\tau},$$

and

$$\alpha = \alpha_p + \alpha_s.$$

Also note that $\tilde{\alpha}_e$ is related to the electric polarizability α_p via

$$\tilde{\alpha}_e = \frac{2\sigma_e + (1 + \phi\alpha_p)\sigma_c}{\tilde{\sigma}}.$$

The average polarization of the whole aggregate is given by:

$$n < \tilde{\mathbf{P}} > = \phi \cdot \alpha_p \cdot \sigma_e \tilde{\mathbf{E}} \tag{4.19}$$

$$n < \tilde{\mathbf{S}} > = \phi \cdot \alpha_s \cdot \sigma_e \tilde{\mathbf{E}} \tag{4.20}$$

Importantly, $\tilde{\mathbf{E}}$ can be related to the applied pulse $\tilde{\mathbf{E}}_{ext}$ by averaging equation (4.14) within a spherical shell volume between the membrane and R_2. By integration, the dipolar contribution is zero, and we establish a relationship with the average external

electric field, $\bar{\mathbf{E}}_e$, $\tilde{\alpha}_e\tilde{\mathbf{E}} = (1-\phi)\bar{\mathbf{E}}_e$. We already showed that

$$(1-\phi)\bar{\mathbf{E}}_e = \tilde{\mathbf{E}}_{ext} + \frac{n < \tilde{\mathbf{P}} >}{\sigma_e} + \frac{n < \tilde{\mathbf{S}} >}{\sigma_e - \sigma_c},$$

therefore the local electric field is given by

$$\tilde{\mathbf{E}} = \kappa^{-1}\tilde{\mathbf{E}}_{ext}, \tag{4.21}$$

with

$$\kappa = \alpha_e - \phi\alpha_p - \phi\frac{\sigma_e\alpha_s}{\sigma_e - \sigma_c}, \tag{4.22}$$

which simplifies to

$$\kappa = \frac{(2+3\phi)\sigma_e + \sigma_c}{\tilde{\sigma}} - \frac{3\phi^2\sigma_c}{(2+\phi)\tilde{\sigma}(\eta + j\omega\tau)}. \tag{4.23}$$

For example figure 4.3 illustrates the magnitude of $\mathbf{E}$ for two different membrane conductivities.

At the aggregate level, we can define the membrane susceptibility, $n < \mathbf{P} >= \sigma_e\chi_p\mathbf{E}_{ext}$, the cytoplasm susceptibility, $n < \mathbf{S} >= \sigma_e\chi_s\mathbf{E}_{ext}$, as well as the overall cell susceptibility, $n < \mathbf{M} >= \sigma_e\chi\mathbf{E}_{ext}$, that relate the applied electric pulse to the induced polarization densities. Equation (4.21) allows us to relate the applied pulse to the induced polarizations, therefore we obtain the susceptibility coefficients

$$\chi_p = \frac{\phi\alpha_p}{\kappa} \quad \text{and} \quad \chi_s = \frac{\phi\alpha_s}{\kappa},$$

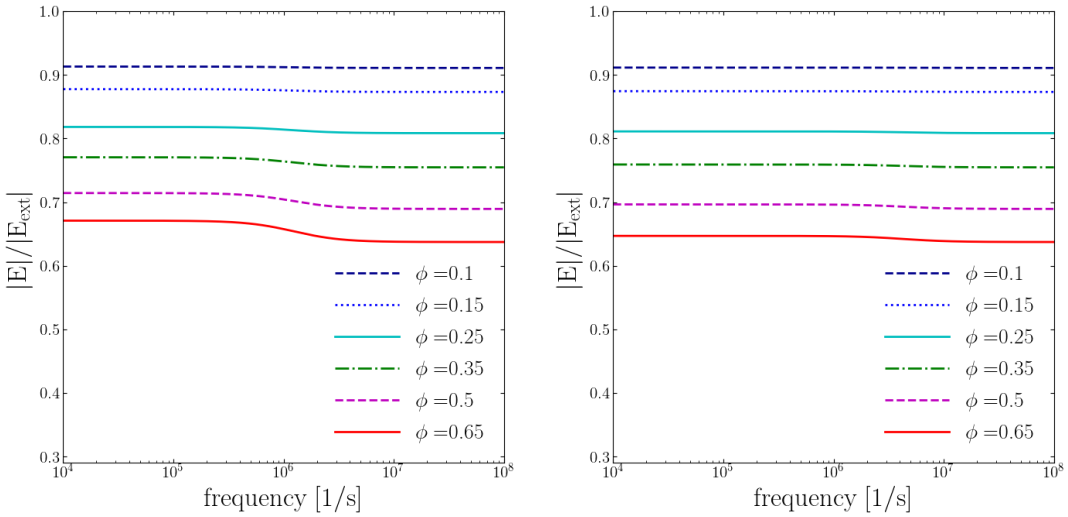

Figure 4.3: *The magnitude of the local electric field at different frequencies and volume fractions for* $(\sigma_e, \sigma_c) = (1.3, 0.6)$ $[S/m]$ *and* $S_L = 1.9$ $[S/m^2]$ *(left) and* $S_L = 1.9 \times 10^5$ $[S/m^2]$ *(right).*

which also imply that

$$\frac{(1-\phi)\bar{E}_e}{E_{ext}} = \frac{\alpha_e}{\kappa} \quad \text{and} \quad \frac{\phi\bar{E}_c}{E_{ext}} = \frac{\sigma_e\chi_s}{\sigma_c - \sigma_e}.$$

The time-domain version of $\mathbf{E}$ can be found by expressing the complex factor $\eta + j\omega\tau$ in equation (4.23) in terms of $< \mathbf{P} >$. By noting that

$$\eta + j\omega\tau = \frac{-3\phi\sigma_e\tilde{E}}{(2+\phi)n < P >},$$

we obtain that

$$\kappa = \frac{(2+3\phi)\sigma_e + \sigma_c}{\tilde{\sigma}} + \phi\frac{\sigma_c}{\tilde{\sigma}}\frac{n < \tilde{P} >}{\sigma_e\tilde{E}},$$

which, substituted into equation (4.21) leads to

$$\mathbf{E}(t) = \frac{\tilde{\sigma}\mathbf{E}_{ext}(t) - \nu\phi n < \mathbf{P}(t) >}{(2+3\phi)\sigma_e + \sigma_c}$$

where $\nu = \sigma_c/\sigma_e$. For the purpose of developing time-domain equations it is also useful to write the cytoplasm polarization in terms of the membrane polarization:

$$n < \mathbf{S} >= -3\phi\frac{\sigma_e - \sigma_c}{\tilde{\sigma}}\left(\sigma_e\mathbf{E} + \frac{2+\phi}{3\phi}n < \mathbf{P} > \right).$$

4.3.3 Effective conductivity

Maxwell (1873) [133] first considered the problem of calculating effective conductivity coefficients for dilute spherical inclusions. A century later, Jeffrey (1973) [162] included pairwise interactions into Maxwell's theory, for increasing the validity of the estimated effective conductivity for higher concentrations. Chiew and Glandt (1983) [175] considered a more realistic pair-correlation function to improve on the accuracy of Jeffrey's result. In parallel, Hasselman and Johnson 1987 [176] included the effect of interfacial resistance to Maxwell's theory, which was subsequently integrated with Jeffrey's theory by Chiew and Glandt [177]. In this section, we derive the effective conductivity based on the work of Batchelor for transport phenomena in two-phase media composed of an statistically homogeneous suspension of particles with random configurations (see *e.g.* [168, 178, 169]). We emphasize that for improved accuracy one has to modify this approach to include divergences of all higher order multipole moments; we refer the interested reader to [179, 180].

First, we define the average flux in a volume large enough to include many cells,

$$< \mathbf{J} >= \frac{1}{V}\int_V \mathbf{J}\ dV,$$

and we seek a linear relationship between the average flux and the potential gradient

$$< \mathbf{J} >= -\bar{\sigma} < \nabla u >, \tag{4.24}$$

where the proportionality coefficient defines the *effective conductivity*. We decompose $< \mathbf{J} >$ into three different regions,

$$\begin{aligned} < \mathbf{J} > &= \frac{1}{V}\int_{V-\sum_i V_i} \mathbf{J} dV + \frac{1}{V}\sum_i \int_{V_i \cup V_i'} \mathbf{J} dV \\ &= \frac{1}{V}\int_V -\sigma_e \nabla u\ dV + \frac{1}{V}\sum_i \int_{V_i \cup V_i'} \boldsymbol{\tau} dV \end{aligned}$$

where $\sum_i V_i$ is the volume occupied by cells. Last expression is obtained by replacing $\mathbf{J}_k = -\sigma_k \nabla u \equiv -\sigma_e \nabla u + \boldsymbol{\tau}_k$ such that $\tau_k = (\sigma_e - \sigma_k)\nabla u$. In the membrane we approximate $\nabla u = [u]\mathbf{n}/h$, therefore,

$$< \mathbf{J} > = -\sigma_e < \nabla u > + n < \mathbf{S} > + \big(1 - \frac{\sigma_m}{\sigma_e}\big) n < \mathbf{P} > \tag{4.25}$$

which in terms of the dipolar polarization and the external electric field is given by

$$\begin{aligned} <\mathbf{J} >= \sigma_e \mathbf{E}_{ext} &\left(\frac{2+\nu+3\phi\nu}{2+\nu+3\phi}\right) + \\ n < \mathbf{P} > &\left(1 - \frac{\sigma_m}{\sigma_e} - \frac{\sigma_e - \sigma_c}{\tilde{\sigma}}[2 + \phi - \frac{3\nu\phi^2}{2+3\phi+\nu}]\right). \end{aligned}$$

Moreover, using the definition of the effective conductivity (4.24) and the fact that $- <$

$\nabla u >= \mathbf{E}_{ext}$, we deduce that the parallel ($\|$) and the transverse ($\perp$) components of the effective conductivity are given by

$$\frac{\bar{\sigma}_{\|}}{\sigma_e} = \frac{< J_{\|} >}{\sigma_e E_{ext}} \quad \text{and} \quad \frac{\bar{\sigma}_{\perp}}{\sigma_e} = \frac{< J_{\perp} >}{\sigma_e E_{ext}}.$$

Particularly, in the frequency domain, the parallel component satisfies

$$\frac{\bar{\sigma}}{\sigma_e} = 1 + \chi_s + (1 - \frac{\sigma_m}{\sigma_e})\chi_p. \tag{4.26}$$

For infinitely conductive membranes, where $\eta \to \infty$, equation (4.26) can be simplified by noting that

$$\frac{\sigma_m}{\sigma_e} = \frac{h}{R_1} \cdot \frac{(2+\phi)\sigma_c}{\tilde{\sigma}} \cdot (\eta - 1) \tag{4.27}$$

and that the membrane polarization vanishes. In this case, equation (4.26) reduces to Maxwell's equation for the effective conductivity of a dilute suspension [181]:

$$\frac{\bar{\sigma}}{\sigma_e} \to 1 - 3\phi \frac{1 - \nu + \nu h/R_1}{2 + \nu + 3\phi} \tag{4.28}$$

and $h/R_1 \to 0$. Note that Maxwell's result is only a $\mathcal{O}(\phi)$ estimate of the effective conductivity, and that, to its limit of validity, equation (4.28) coincides with Maxwell's approximation (see *e.g.* [162]).

On the other hand, one could identify relative complex permittivity $\epsilon^* = \epsilon' - j\epsilon''$ through its definition, *i.e.* the current J is related to an alternating applied field E via

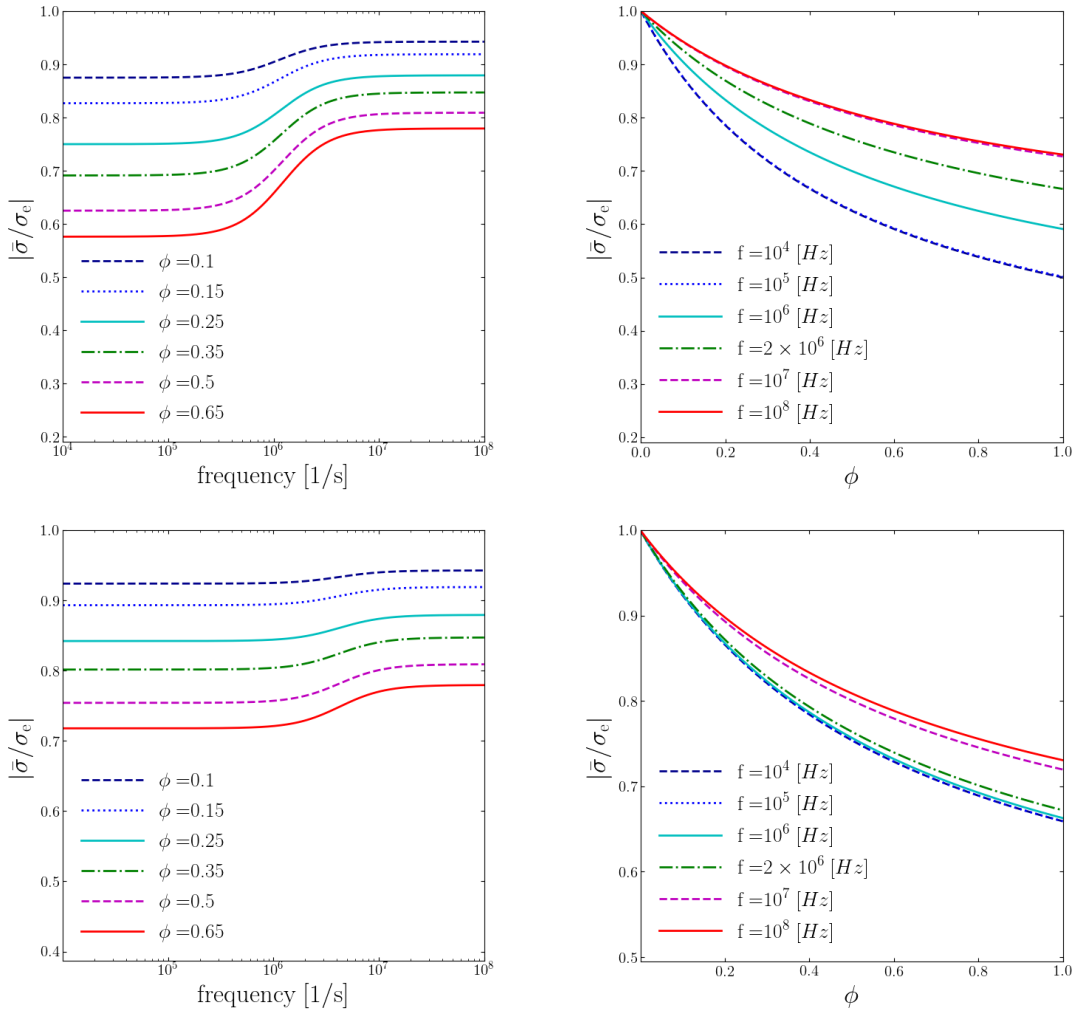

Figure 4.4: *Equation* (4.30) *for* $\nu = 0.46$ *with* $\sigma_e = 1.3$ $[S/m]$, $\sigma_c = 0.6$ $[S/m]$, *and the cell radius set to* 7 $[\mu m]$. *(a,b) Low membrane conductance* $S_L = 1.9$ $[S/m^2]$, *(c,d) high membrane conductance* $S_L = 1.9 \times 10^5$ $[S/m^2]$.

$J = \sigma_e E + j\omega\epsilon_0\epsilon^* E$. Comparing with equation (4.25), we can write

$$j\omega\epsilon_0\epsilon^* \mathbf{E}_{ext} = (1 - \frac{\sigma_m}{\sigma_e})n < \mathbf{P} > +n < \mathbf{S} >,$$

with

$$\epsilon^* = \frac{\sigma_e}{j\omega\epsilon_0} \cdot ((1 - \frac{\sigma_m}{\sigma_e})\chi_p + \chi_s) = \epsilon' - j\epsilon'',$$

where ϵ' is the dielectric constant, ϵ'' is the loss factor of the material and $\epsilon_0 = 8.854 \times 10^{-12}$ $[F/m]$ is the dielectric permittivity of free space. Furthermore, the complex admittance is given by $Y^* = (\sigma_e + j\omega\epsilon_0\epsilon^*)A_{el}/H$. The admittance being the inverse of the impedance, Z, we have:

$$\begin{aligned} Z &= \frac{H}{A_{el}} \cdot \frac{1}{\sigma_e + j\omega\epsilon_0\epsilon^*} \\ &= \frac{H}{A_{el}} \cdot \frac{\mathbf{E}_{ext} \cdot \mathbf{k}}{(\sigma_e \mathbf{E}_{ext} + (1 - \frac{\sigma_m}{\sigma_e})n < \mathbf{P} > +n < \mathbf{S} >) \cdot \mathbf{k}} \end{aligned} \tag{4.29}$$

where H is the distance between the electrodes and A_{el} is the surface area of one electrode. We designate $Z_e = H/(\sigma_e A_{el})$ to define the dimensionless impedance as

$$\begin{aligned} \frac{Z}{Z_e} &= \frac{\sigma_e \mathbf{E}_{ext} \cdot \mathbf{k}}{(\sigma_e \mathbf{E}_{ext} + (1 - \frac{\sigma_m}{\sigma_e})n < \mathbf{P} > +n < \mathbf{S} >) \cdot \mathbf{k}}. \\ &= \frac{1}{1 + (1 - \frac{\sigma_m}{\sigma_e})\chi_p + \chi_s} \end{aligned}$$

Lastly, the complex conductivity σ^* of the material is related to the admittance according to $Y^* = \sigma^* A_{el}/H = 1/Z$ which implies that:

$$\sigma^* = \sigma_e \cdot (1 + (1 - \frac{\sigma_m}{\sigma_e})\chi_p + \chi_s).$$

Therefore, the values for admittance and the effective conductivity coincide.

Effects of cellular pairwise interactions. Cell-cell interactions influence the effective conductivity of the aggregate, for example in the case of spherical particles Jeffrey (1973) [162] showed that pairwise interactions produce a correction term of order $\mathcal{O}(\phi^2)$ to the effective conductivity of a random dispersion of spherical particles. Importantly, Jeffrey used the *twin spherical harmonics* invented by Ross (1968) [182] to account for two-particle interactions. This method was later applied to coated spheres by Lu and Song (1996) [183]. [183] derived the general expression for the effective conductivity of a random suspension of coated spheres, that is accurate up to order $\mathcal{O}(\phi^2)$:

$$\frac{\bar{\sigma}}{\sigma_e} = 1 + 3\phi\theta_1 + \frac{3\phi^2\theta_1^2}{1-\phi\theta_1} + \frac{K_2^*\phi^2}{1-\phi\theta_1}, \tag{4.30}$$

where $3\phi\theta_1 \equiv \chi_s + (1 - \frac{\sigma_m}{\sigma_e})\chi_p$ is the polarizability factor. K_2^* accounts for higher order interactions due to detailed pair distribution of particles; here we neglect this last term as we are not considering detailed information about the microstructure of the aggregate (see Hasselman and Johnson (1987) [176] for a similar result). As shown by [183], this estimate stays within Hashin-Shtrikman bounds [184] up to high volume fractions of about $\phi \approx 0.6$. Figure 4.4 illustrates the dependence of the effective conductivity on the volume fraction and on the frequency predicted by equation (4.30) after setting $K_2^* = 0$.

4.4 Coarse-grained dynamics

In the present modeling approach, cell-level dipole moments are the resolved observables that relate cellular properties to multicellular features. In this section, we introduce *time-domain* governing equations for the dipole moments.

We consider a spherical cell of radius R immersed in a mean electric flux $< J >$,

$$C_m \frac{\partial [u]}{\partial t} + \left(S_m + \frac{(2+\phi)\sigma_e \sigma_c}{R\tilde{\sigma}} \right) [u] = \frac{3\sigma_c \sigma_e}{\tilde{\sigma}} E \cos\theta, \tag{4.31}$$

and we seek a governing equation for the membrane dipole by integrating equation (4.31) over cell membranes and multiplying by σ_e,

$$C_m \frac{d}{dt}\mathbf{P} + \left(S_m + \frac{(2+\phi)\sigma_e \sigma_c}{R\tilde{\sigma}} \right) \mathbf{P} = -\frac{\sigma_e^2 \sigma_c}{\tilde{\sigma}} A\mathbf{E}.$$

Here we assumed a uniform conductance over the cell membranes. We divide both sides with the cell volume and obtain:

$$C_m \frac{d}{dt}\mathbf{p} + \left(S_m + \frac{(2+\phi)\sigma_e \sigma_c}{R\tilde{\sigma}} \right) \mathbf{p} = -\frac{3\sigma_e^2 \sigma_c}{R\tilde{\sigma}} \mathbf{E}$$

Due to this mean-field approximation, each cell evolves ostensibly independently from each other. Therefore, we define the coarse grained electrodynamics of an individual cell with

$$\dot{\mathbf{p}} = -\gamma \mathbf{p} - \alpha \mathbf{u}(t), \tag{4.32}$$

where we represent the time-dependent model for the electric flux with $\mathbf{u}(t)$ and define

$$\alpha = \frac{3\sigma_e \sigma_c}{C_m R\tilde{\sigma}} \qquad\qquad \gamma = \frac{S_m}{C_m} + \frac{\sigma_e \sigma_c}{R C_m \tilde{\sigma}}(2+\phi)$$

and the stimulating field is that of the mean electric field in the matrix at any given time

t,

$$\mathbf{u}(t) \equiv \sigma_e \mathbf{E}(t) = \sigma_e \kappa^{-1} \mathbf{E}_{ext}(t).$$

Note that $\mathbf{u}(t)$ is the mean field approximation for the external electric current that each cell feels.

Starting from the microscopic equation (4.32) we shall derive a mesoscopic model for an ensemble of cells. The basic idea is to view an ensemble of dipoles as random variables, and subsequently treat equation (4.32) as a Langevin equation for the dynamical evolution of the random variables. In 1908, Langevin introduced the concept of equation of motion of a random variable [185] and through his formulation of the dynamical theory of Brownian motion, he initiated the subject of stochastic differential equations [186].

To bridge the microscale to the mesoscale, we are interested to know the probability distribution of dipole moments in an aggregate. In stochastic systems (*e.g.* in many condensed matter systems that are in contact with a heat bath) a successful strategy is to start from a Langevin equation describing the evolution of a single particle. Then, through appropriate averaging procedures, one arrives at a Fokker-Planck equation describing the evolution of the probability distribution of that particle. Eventually, the independence assumption implied in the mean field approximation allows to define the total probability distribution $W(\{p_k\}, t)$ as the product of that of individual particles $W(\{p_k\}, t) = \Pi_i W_i(p_i, t)$.

Unfortunately, this procedure fails in the system of cell aggregates due to the deterministic nature of the electrodynamics of cells. Through direct numerical simulations we know that the evolutionary trajectory of cell dipoles is not a stochastic process; in fact equation (4.32) already suggests that polarizations are given by a deterministic equation. In the next subsection, we solve this problem by considering the randomness in cell

parameters (see figure 4.5) and devise a stochastic interpretation. We also mention the interesting work of Takayasu *et al.* (1997) [187] who took a similar strategy to analyze the conditions for the emergence of power-law distributions in specific discrete Langevin models of the form $x(t+1) = b(t)x(t) + f(t)$ where both $b(t)$ and $f(t)$, are random variables.

4.4.1 The indistinguishable stochastic replica

The main source of randomness in the dielectric response of multicellular systems is the diversity of cell parameters, *i.e.* namely α and γ. Here we exercise an alternative viewpoint to replace a diverse ensemble of deterministic cells with an indistinguishable ensemble of stochastic elements. In particular we consider a *fiducial* random-walk process in cell parameters such that the empirical probability density of cells matches that of actual ones at any timestep. This is achieved by defining two random processes $A(t)$ and $B(t)$ for each cell such that

$$\alpha_i = \bar{\alpha} + A_i(t),$$
$$\gamma_i = \bar{\gamma} + B_i(t),$$

and

$$\bar{\gamma} =< \gamma >, \qquad \bar{\alpha} =< \alpha > .$$

Figure 4.5 illustrates the distribution of these parameters. It is evident that around their mean values the distributions follow an exponential profile (note that the central part of this figure is linear and the y-axis is in logarithmic scale), however as a first step we

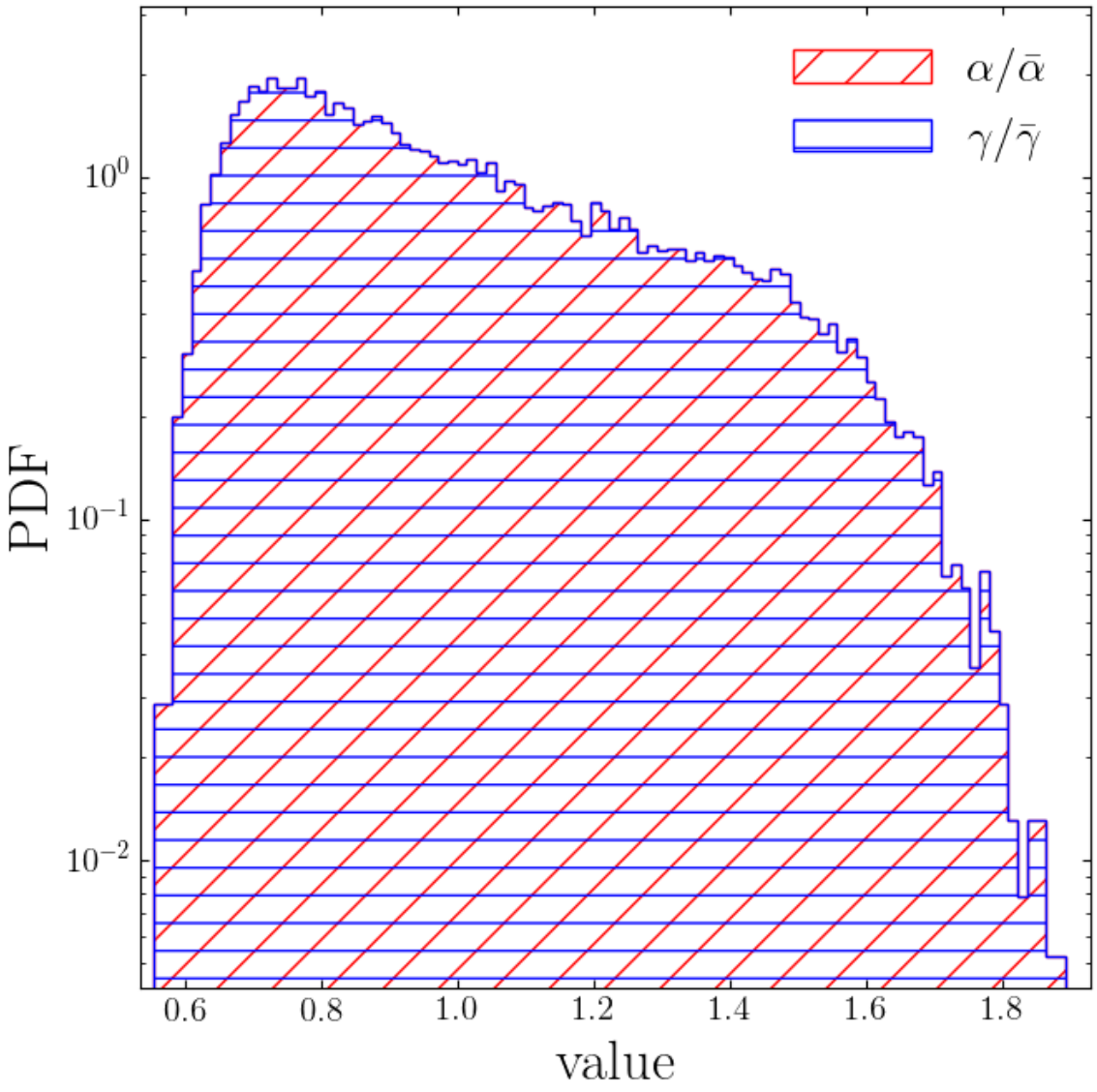

Figure 4.5: *Distribution of α and γ parameters used in numerical simulation. The densities follow exponential profile in the middle range.*

approximate these random processes with Gaussian white noise

$$\begin{aligned} < B_i(t) > &= 0 \\ < A_i(t) > &= 0 \\ < A_i(t)A_j(t') > &= \alpha'^2\delta_{ij}\delta(t-t') \\ < B_i(t)B_j(t') > &= \gamma'^2\delta_{ij}\delta(t-t') \\ < A_i(t)B_j(t') > &= \epsilon\alpha'\gamma'\delta_{ij}\delta(t-t') \end{aligned}$$

where $|\epsilon| \leq 1$ models the degree of cross-correlation between the two noise terms. Substituting in equation 4.32 yields

$$\dot{\mathbf{p}}_i = -\bar{\gamma}\mathbf{p}_i - \bar{\alpha}\mathbf{u}(t) - \mathbf{p}_i B_i(t) - \mathbf{u}(t)A_i(t). \tag{4.33}$$

Equation (4.33) is a Langevin model with both additive and multiplicative noise terms. In analogy, the additive noise term models a *heat bath* acting on the dipole and the multiplicative noise term models effects of a fluctuating barrier. Interestingly, such hybrid models of arithmetic and geometric Brownian motions have many applications in Physics [188, 189], Biology [190] and finance [191].

We take equation (4.33) along each spatial dimension as an independent stochastic differential equation in the random variable $X_t \equiv p_k$, then we combine the two Brownian motions into a single Brownian motion to arrive at the stochastic differential equation

$$\begin{aligned} dX_t =& (-\bar{\alpha}u - \bar{\gamma}X_t)dt \\ &+ \sqrt{\alpha'^2u^2 + 2\epsilon\gamma'\alpha'uX_t + \gamma'^2X_t^2}dW_t \end{aligned} \tag{4.34}$$

where W_t is a Wiener process. This is in fact a member of *Pearson diffusions* that were

extensively considered by Forman and Sørenson [192].

Here we emphasize that the replica stochastic aggregate must render a similar distribution of polarizations as in the actual system, therefore in general the processes $A(t)$ and $B(t)$ are not Markov processes with Delta autocorrelation in time. In fact the specificities of these random processes must be tuned to match the actual distribution. In the next section we simply consider white noise as a first approximation in this direction.

4.4.2 The Fokker-Planck equation

Equation (4.34) constitutes the Stratonovich vector stochastic differential equations of a Langevin equation with a multiplicative noise term. The generic form of the coupled stochastic differential equation in terms of stochastic variables ξ_i's reads

$$\frac{d\{\xi\}_i}{dt} = h_i(\xi_1, \xi_2, \xi_3, t) + g_{ij}(\xi_1, \xi_2, \xi_3, t)\lambda_j(t)$$

with $g_{ij}\lambda_j$ are multiplicative noise terms that produce the noise-induced drift and diffusion components. $\boldsymbol{\lambda}$ has the following property,

$$< \lambda_i(t) >= 0, \qquad\qquad < \lambda_i(t)\lambda_j(t+\tau) >= \delta_{ij}\delta(\tau)$$

Then these equations can be treated as the starting point for deriving the corresponding Fokker-Planck equation. To this end, let $\xi_1 = p_x$, $\xi_2 = p_y$, and $\xi_3 = p_z$ and $W(\xi_1, \xi_2, \xi_3, t)d\xi_1 d\xi_2 d\xi_3$ be the probability of finding a dipole in $d\xi_1 d\xi_2 d\xi_3$ at time t, then the Fokker-Planck equation reads

$$\frac{\partial W}{\partial t} = -\frac{\partial}{\partial \xi_i}(D_i W) + \frac{1}{2}\frac{\partial^2}{\partial \xi_i \partial \xi_j}(D_{ij} W)$$

where the Einstein's summation rule is implied. By use of the Langevin equations, one can evaluate the statistical averages $< \cdot >$ in order to get the following set of equations for the drift and the diffusion coefficients [193]:

$$D_i = h_i(\{\xi\}, t) + \frac{1}{2} g_{kj}(\{\xi\}, t) \frac{\partial}{\partial \xi_k} g_{ij}(\{\xi\}, t),$$
$$D_{ij} = g_{ik}(\{\xi\}, t) g_{jk}(\{\xi\}, t).$$

Hasegawa (2008) [194, 195] considered solutions to the Fokker-Planck equations associated with Langevin equation (4.33) in the Stratonovich stochastic calculus; furthermore, Mortensen (1979) [196] derived the Fokker-Planck equation associated to SDE 4.34 according to Ito stochastic calculus. Fortunately this system is separable and we can treat it one dimension at a time for our analysis, *i.e.* the other two dimensions can be identically treated. The governing FPE for the variable $x \equiv p_k$ with the Stratonovich interpretation reads:

$$\begin{aligned} \frac{\partial}{\partial t} W(x,t) = & \\ & \frac{\partial}{\partial x} \left[\bar{\gamma} x + \bar{\alpha} u(t) - \frac{\chi}{2} (\gamma'^2 x + \epsilon \gamma' \alpha' u(t)) \right] W(x,t) \\ & + \frac{1}{2} \frac{\partial^2}{\partial x^2} \left[\gamma'^2 x^2 + 2\epsilon \gamma' \alpha' u(t) x + \alpha'^2 u^2(t) \right] W(x,t) \end{aligned} \tag{4.35}$$

where $\chi = 0, 1$ corresponds to the Ito or the Stratonovich interpretations of the stochastic calculus respectively.

4.4.3 Analytical Treatment

The invariant probability distribution has a density that satisfies:

$$\frac{d}{dx}W(x) = -\frac{(\bar{\gamma} + \frac{\chi}{2}\gamma'^2)x + (\bar{\alpha} + \frac{\chi}{2}\epsilon\alpha'\gamma')u}{\frac{1}{2}\gamma'^2x^2 + \epsilon\alpha'\gamma'ux + \frac{1}{2}\alpha'^2u^2}\ W(x) \tag{4.36}$$

Equation (4.36) resembles the invariant density of *Pearson diffusion* processes that are characterized with a linear drift and quadratic diffusion coefficients. Therefore, we find that the Fokker-Planck equation (4.35) falls in the category of Pearson diffusion processes [197], whose stationary probability density is invariant under translation and scale transformations. Statistical properties of this class of models have been analyzed by Forman and Sørenson [192] (for a brief summary see section 1.13.12 of [198]). Fundamentally, Pearson diffusions are viewed as the solutions to the following stochastic differential equation in the canonical parameterization:

$$dX_t = -\theta(X_t - \hat{\mu})dt + \sqrt{2\theta(\mathtt{a}X_t^2 + \mathtt{b}X_t + \mathtt{c})}dW_t,$$

with $\theta > 0$ being a scaling of time that determines how fast the distribution evolves, $\mathtt{a}, \mathtt{b}, \mathtt{c}$ are shape parameters such that the diffusion coefficient is well defined, and W_t is a Wiener process.

Pearson processes can lead to a variety of distributions depending on the parameters of the drift and the diffusion coefficients such as heavy or light tailed and symmetric or skewed profiles [192]. We briefly report six basic subfamilies from [192, 198] that are determined using criteria on the degree of the diffusion polynomial in the denominator of equation (4.36) denoted here by `deg`, the sign of the leading coefficient (that in our case is strictly positive), and the discriminant $\Delta = \mathtt{b}^2 - 4\mathtt{ac}$:

1. *if* $\mathtt{deg} = 0$*:* A Ornstein-Uhlenbeck process with a normal invariant density.

2. *if* $\texttt{deg} = 1$*:* If $0 < \hat{\mu} \leq 1$ we obtain a Cox-Ingersoll-Ross process while for $\hat{\mu} > 1$, we obtain a gamma invariant density.

3. *if* $\texttt{deg} = 2$ *and* $\Delta > 0$ *and* $\texttt{a} < 0$*:* A Jacobi diffusion with a Beta invariant density.

4. *if* $\texttt{deg} = 2$ *and* $\Delta > 0$ *and* $\texttt{a} > 0$*:* A Fisher-Snedecor process with a Fisher-Snedecor invariant density.

5. *if* $\texttt{deg} = 2$ *and* $\Delta = 0$*:* A Reciprocal gamma process with an inverse gamma invariant density.

6. *if* $\texttt{deg} = 2$ *and* $\Delta < 0$*:* for $\hat{\mu} \neq 0$ we obtain a Student diffusion with a skewed t invariant density, while for $\hat{\mu} = 0$ we obtain a scaled t-distribution.

In the current case, and under a non-zero applied pulse, we can establish that the discriminant is always negative

$$\Delta = -4\big(\alpha'\gamma' u\big)^2(1-\epsilon^2) < 0.$$

Therefore, we expect that the probability density of the dipole moments along the z-axis (parallel to the applied pulse) is best described by a *skewed Student* distribution (also known as Pearson type IV distribution). Even though in the transverse direction the mean electric pulse is negligible based on our mean field model, we can not totally neglect the influence of the electric fluctuations. To first order approximation we treat the transverse direction by setting $\hat{\mu} = 0$ while preserving the same diffusion term as in the parallel direction. This also ensures a symmetric probability density for positive or negative values. Therefore, we conclude that the distribution in the transverse direction must follow a scaled t-distribution (also known as Pearson type VII distribution).

Stationary Probability Density

In the direction parallel to the applied pulse. We can directly integrate equation (4.36) to identify the invariant distribution

$$W_s(x;\nu,c,a,\lambda) = K\frac{\exp\left\{2c\tan^{-1}\left(\frac{x-\lambda}{a}\right)\right\}}{\left(1+\left(\frac{x-\lambda}{a}\right)^2\right)^{\nu}}, \tag{4.37}$$

where

$$a = \frac{\alpha' u}{\gamma'}\sqrt{1-\epsilon^2}, \quad \lambda = -\frac{\epsilon\alpha' u}{\gamma'},$$
$$\nu = \frac{\chi}{2} + \frac{\bar{\gamma}}{\gamma'^2}, \quad c = \frac{\epsilon\alpha'\bar{\gamma} - \bar{\alpha}\gamma'}{\alpha'\gamma'^2\sqrt{1-\epsilon^2}},$$

and

$$K = \frac{\left|\Gamma(\nu+ic)\right|^2}{a\sqrt{\pi}\Gamma(\nu)\Gamma(\nu-1/2)}.$$

Equation (4.37) provides the average and the variance of the polarizations in the stationary state (*cf.* original work of [199], and [200] for a useful guide):

$$\mu \equiv \mathbb{E}(X_t) = \frac{ac}{\nu-1} + \lambda = \frac{\epsilon\alpha'\gamma' u - \bar{\alpha}u}{\bar{\gamma}-\gamma'^2}, \tag{4.38}$$

$$\sigma^2 \equiv \mathbb{E}(X_t^2) - \mathbb{E}(X_t)^2 = \frac{a^2[(\nu-1)^2+c^2]}{(\nu-1)^2(2\nu-3)}$$
$$= \frac{\gamma'^2\mu^2 + 2\epsilon\gamma'\alpha' u\mu + \alpha'^2 u^2}{2(\bar{\gamma}-\gamma'^2)}, \tag{4.39}$$

where we have let $\chi = 1$ to obtain the last equalities. Equation (4.37) can be independently verified by comparing it to model B of Hasegawa [195] via the change of notations $\lambda_H \equiv \bar{\gamma}$, $I_H \equiv -\bar{\alpha}u$, $\alpha_H \equiv \gamma'$, $c_H \equiv c$, $b_H \equiv \nu$, $f_H \equiv -\lambda$ and $\beta_H \equiv \alpha' u$ (the H subscript indicates Hasegawa's notation). Moreover, Hasegawa [195] derived approximate equations for the evolution of the average and the variance in this model that we report

here for completeness:

$$\frac{d\mu}{dt} = -\bar{\gamma}\mu(t) - \bar{\alpha}u + \gamma'^2\mu(t) + \epsilon\gamma'\alpha' u, \tag{4.40}$$

$$\frac{d\sigma^2}{dt} = -2(\bar{\gamma} - \gamma'^2)\sigma(t)^2 + \gamma'^2\mu(t)^2 + 2\epsilon\gamma'\alpha' u\mu(t) + \alpha'^2 u^2, \tag{4.41}$$

which provide the analytical formula for the evolution of the probability density throughout the polarization process when replacing the static values ν and c in equation (4.37) by their dynamic counterparts:

$$\nu(t) = \frac{a^2 + (\mu(t) - \lambda)^2 + 3\sigma(t)^2}{2\sigma(t)^2},$$
$$c(t) = \left(\frac{a^2 + (\mu(t) - \lambda)^2 + \sigma(t)^2}{2a\sigma(t)^2}\right)(\mu(t) - \lambda).$$

Figure 4.9 gives a comparison between the results obtained with model (4.41) and the direct numerical simulation of Mistani *et al.* [2]. A few remarks follow: (i) Hasegawa's moment equations are valid approximations up to order $\mathcal{O}((\delta x)^2)$ about the mean value of dipolar polarization per cell volume, and (ii) in the current model, the dynamics for $\mu(t)$ appears to be decoupled from σ^2, which is merely the result of assuming a linear dependence for the conductance term $F(x) \equiv -\bar{\gamma}x$, as well as a linear assumption for the multiplicative noise factor $G(x) \equiv x$. Breaking either of these assumptions introduces extra contributions from the variance to the mean dynamics. However, such modifications would alter the stationary distribution of polarizations, which the current model captures well. Therefore we expect that the observed discrepancies in the temporal evolution between the model prediction and the direct numerical simulation most likely stem from the nature of the noise term. This could be alleviated by introducing fractional-order temporal derivatives. Indeed, figure 4.9 actually proves that the transient dynamics of dipolar moments does not simply follow an exponential function.

In the direction perpendicular to the applied pulse. In the transverse direction, the stationary density follows a symmetric t-distribution, which is obtained by setting the skewness parameter to zero in the skewed t-distribution (4.37), *i.e.* set $c = 0$ and all previous equations are valid. This indicates that the following identity regulates the transverse diffusion,

$$\epsilon_{\perp} \frac{\alpha'_{\perp}}{\bar{\alpha}} = \frac{\gamma'_{\perp}}{\bar{\gamma}}$$

Statistical moments

In the type IV Pearson diffusions considered in this work, for $n \geq 2$ the n^{th} statistical moment can be computed using the recurrence formula [200]:

$$\begin{aligned} \mu_n =& \frac{a(n-1)}{(\nu-1)^2[2(\nu-1)-(n-1)]} \\ & \times \left\{ c(\nu-1)\mu_{n-1} + a((\nu-1)^2 + c^2)\mu_{n-2} \right\} \end{aligned} \tag{4.42}$$

where by definition $\mu_0 = 1$ and $\mu_1 = 0$. It is straightforward to check the consistency between equations (4.42) and (4.39).

An important notion is the regime of existence for each of the moments. The first moment exists for $\nu > 1$, otherwise $< x >= \pm\infty$. The variance exists for $\nu > 3/2$, otherwise it increases arbitrarily fast. The third moment exists if $\nu > 2$ and the fourth moment exists for $\nu > 5/2$.

Fitting statistical moments

We use the simple moment fitting approach introduced by Karl Pearson [199] (also see Heinrich's excellent guide [200]) to infer the four model parameters (ν, c, a, λ), which

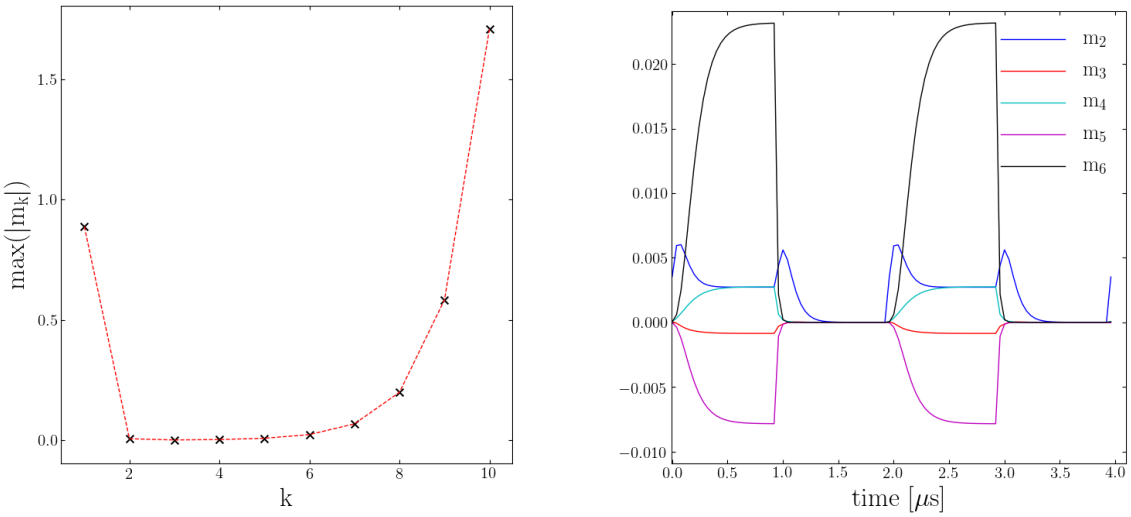

Figure 4.6: *Left: the maximum values of the statistical moments diverge for larger k. Right: the evolution of the second to the sixth statistical moments of* $\mathrm{p_z}$ $[\mathrm{A/mm^2}]$ *in direct numerical simulations, i.e.* $m_k =< (p_z - < p_z >)^k >$.

characterize the stationary probability density (4.37). Given simulation data, we can directly measure the first four statistical moments using the recurrence relation in equation (4.42), *i.e.* we directly calculate $< x >$, μ_2, μ_3 and μ_4. Afterwards, we can infer the unknown parameters using mean, variance and some intermediate quantities defined via the third and fourth moments:

$$\sqrt{\beta_1} \equiv \frac{\mu_3}{\mu_2^{3/2}} = \frac{2c}{\nu - 2}\sqrt{\frac{2\nu - 3}{(\nu-1)^2 + c^2}}$$
$$\beta_2 \equiv \frac{\mu_4}{\mu_2^2} = \frac{3(2\nu-3)[(\nu+2)((\nu-1)^2 + c^2) - 4(\nu-1)^2]}{(\nu-2)(2\nu-5)}$$

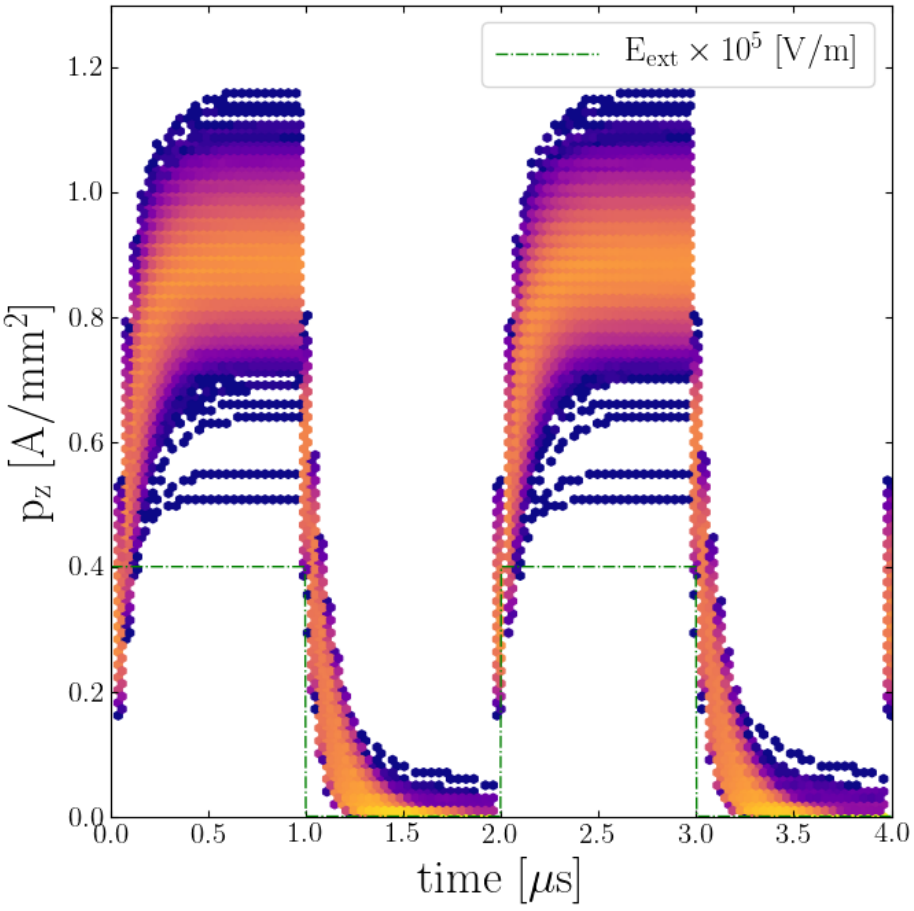

Figure 4.7: *Evolution of dipole moments using direct numerical simulation.*

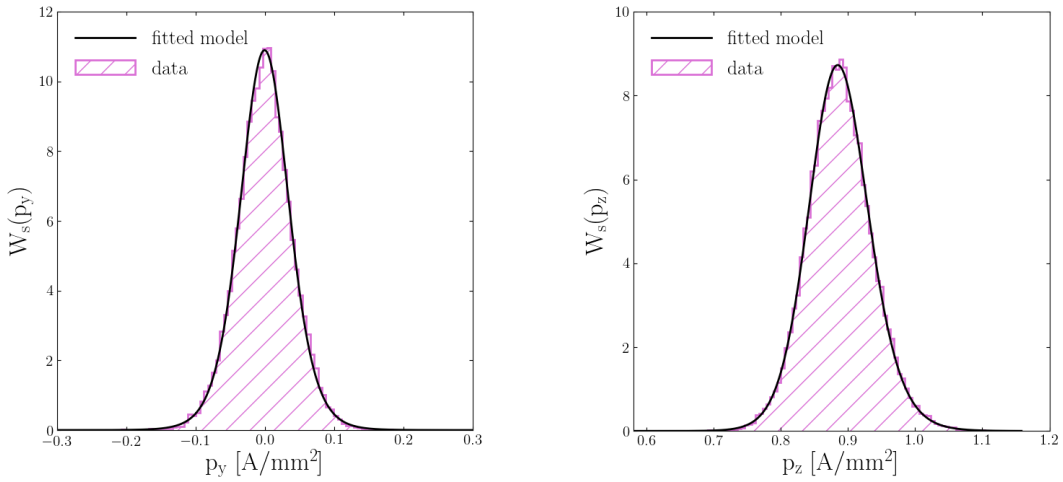

Figure 4.8: *The distribution of dipole moments in direct numerical simulation in comparison to model predictions. Measurements are made after* 1 $[\mu s]$ *of a step electric pulse (when stationarity is almost achieved). Distributions follow (left) a symmetric t-distribution in the transverse direction (along the y-axis) with model parameters* $(\nu, c, a, \lambda) \approx (5.054, 0.000, 0.108\ [A/mm^2], 0.000\ [A/mm^2])$*, while (right) in the direction parallel to the applied pulse (along the z-axis), we observe a skewed t-distribution with model parameters* $(\nu, c, a, \lambda) \approx (7.246, 0.888, 0.164\ [A/mm^2], -0.864\ [A/mm^2])$*. Note that the x-axes is the absolute value of the polarization.*

Thereafter, we compute the missing parameters according to

$$\begin{aligned}
\nu &= \frac{5\beta_2 - 6\beta_1 - 9}{2\beta_2 - 3\beta_1 - 6}, \\
c &= \frac{(\nu-1)(\nu-2)\sqrt{\beta_1}}{\sqrt{4(2\nu-3) - \beta_1(\nu-2)^2}}, \\
a &= \sqrt{\mu_2[(2\nu-3) - \frac{\beta_1}{4}(\nu-2)^2]}, \\
\lambda &= < x > - \frac{\sqrt{\mu_2\beta_1}(\nu-2)}{2}.
\end{aligned}$$

Figure 4.8 illustrates the fitted model and its parameters. We observe that the model given in (4.37) perfectly describes the results provided by our direct numerical simulation. We compare the predictions of our model with the dynamics of the average and of the

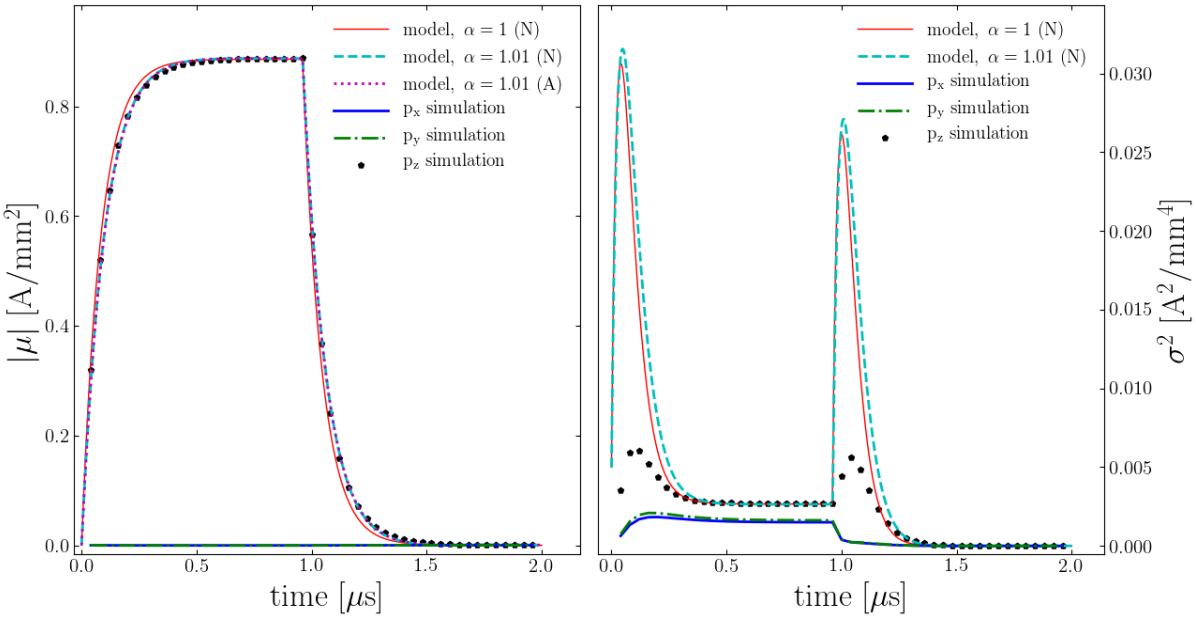

Figure 4.9: *The evolution of average and variance of dipole moments in direct numerical simulations. We chose* $R = 7$ $[\mu m]$ *and* $\phi = 0.13 \times 0.00563$ *to account for the free space surrounding the spherical tumor, i.e. a box of* 4 $[mm]$ *on each side. The dotted magenta line in the left figure illustrates the analytical solution* (4.45)*. Letter N denotes numerical solution of FPE model while A indicates analytical solution of the FPE model.*

variance of dipole moments from our direct numerical simulations in figures 4.9–4.10. A few observations regarding the results of the direct numerical simulation can be drawn: (i) first, the decay of the average polarization does not follow an exponential decay; in fact it decays slightly slower than an exponential function, (ii) second, under a constant applied pulse, the variance increases initially but then decreases to reach a plateau, and after switching off the pulse, variance exhibits an uptick before decaying to zero. The observed uptick in the variance is a unique feature that is captured in our proposed model.

We also solve for the model parameters in terms of the observed distribution param-

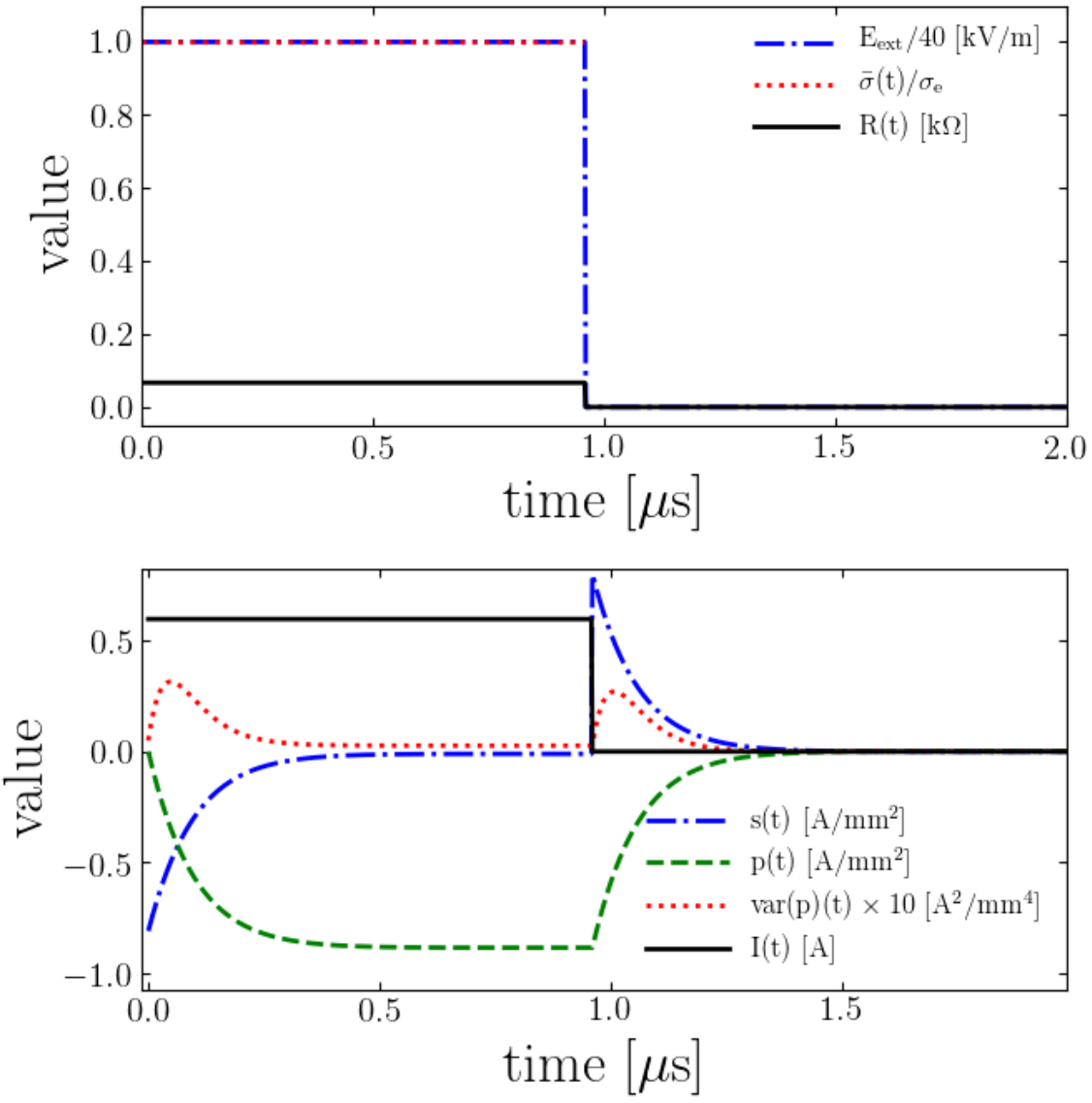

Figure 4.10: *Other time-domain properties based on our model for the case considered in figure 4.9. Immediately after switching off the applied pulse a reverse current is observed.*

eters,

$$\gamma' = \sqrt{\frac{\bar{\gamma}}{\nu - \frac{\chi}{2}}}, \qquad \epsilon = \frac{1}{\sqrt{1 + \frac{a^2}{\lambda^2}}},$$
$$\alpha' = \frac{\bar{\alpha}\gamma'}{\epsilon\bar{\gamma} - c\gamma'^2\sqrt{1-\epsilon^2}}, \qquad u = -\frac{\lambda\gamma'}{\epsilon\alpha'}.$$

The fitted values in figure 4.8 yield

$$(\alpha', \gamma', \epsilon, \mathrm{u}) = (2242.08\ [\sqrt{\mathrm{S/F}}],\ 1446.9\ [\sqrt{\mathrm{S/F}}],\ 0.983,\ 0.568\ [\mathrm{A/mm^2}])$$

while $\bar{\gamma} = 1.41 \times 10^7\ [S/F]$ and $\bar{\alpha} = 2.10 \times 10^7\ [S/F]$. Figure 4.9 depicts the comparison between our Fokker-Planck model and direct numerical simulations. We find that our model perfectly captures the qualitative trends observed in the distribution of the polarizations, while it is in good quantitative agreement. Also, it is important to develop numerical methods for the FPE in three spatial dimensions in order to faithfully compare these results, however the current one dimensional analytic treatment provides very encouraging results for the polarization component parallel to the applied pulse. We will investigate numerical solutions to the full FPE in future works.

Fractional order evolution

In the case of Pearson diffusion, the statistical moments up to order $n < \mathtt{a}^{-1} + 1$ exist. In particular, for $n \geq 2$, the autocorrelation decays exponentially [201]:

$$corr(X_s, X_{s+t}) = e^{-\theta t}.$$

In the current case, statistical moments exist up to order

$$n < 1 + 2\frac{\bar{\gamma}}{\gamma'^2}.$$

Therefore, this analysis suggests that the autocorrelation of dipole moments is given by an exponential decay when

$$\gamma'^2 < 2\bar{\gamma}.$$

This result provides a critical threshold for the diversity measure $\gamma'_c = \sqrt{2\bar{\gamma}}$ that regulates the autocorrelation function, *i.e.* for $\gamma' < \gamma'_c$, we predict anomalous relaxation. Therefore, in our model, the observed anomalous relaxation in cell aggregate electroporation is associated with the diversity in the cellular structural parameters that is modeled through the parameter γ. In this case, the time derivative should be replaced with a fractional order derivative through $\frac{d}{dt} = \tau_1^{\alpha-1}\frac{d^\alpha}{dt^\alpha}$, *i.e.* τ_1 is an arbitrary factor that has dimension of time. Here we assume $\tau_1 = 1$ and the governing equations read:

$$\frac{d^\alpha \mu}{dt^\alpha} = -\bar{\gamma}\mu(t) - \bar{\alpha}u + \gamma'^2\mu(t) + \epsilon\gamma'\alpha' u, \tag{4.43}$$

$$\frac{d^\alpha \sigma^2}{dt^\alpha} = -2(\bar{\gamma} - \gamma'^2)\sigma(t)^2 + \gamma'^2\mu(t)^2 + 2\epsilon\gamma'\alpha' u\mu(t) + \alpha'^2 u^2. \tag{4.44}$$

In order to preserve the type of initial conditions appropriate in classical phenomena, *i.e.* so that no extra initial conditions be needed, we adopt Caputo fractional derivative with $m-1 < \alpha \leq m$ (m is an integer number) [202, 203], which is defined by

$${}_a^C D_t^\alpha f(t) = \frac{1}{\Gamma(m-\alpha)}\int_a^t \frac{f^{(m)}(s)}{(t-s)^{\alpha-m+1}}\, ds.$$

Furthermore, defining fractional derivatives in the Caputo sense permits the application of the Laplace transform as a simple method of solution, see [204] for more details. In this case, the Laplace transform of Caputo derivatives reads:

$$\mathcal{L}[{}_0^C D_t^\alpha f(t)] = s^\alpha f(s) - \sum_{k=0}^{m-1} f^{(k)}(0^+) s^{\alpha-k-1}.$$

Applying the Laplace transform to the set of equations (4.44) and assuming $\mu(0^+) = 0$ and $\mu'(0^+) = 0$ yields the transfer function $H(s)$ (or impulse response) for the average polarization:

$$\mu(s) = H(s)\ u(s), \text{ with } H(s) = \frac{\epsilon\alpha'\gamma' - \bar{\alpha}}{s^\alpha + \bar{\gamma} - \gamma'^2}.$$

Then the impulse response function is given by:

$$H(t) = (\epsilon\alpha'\gamma' - \bar{\alpha}) t^{\alpha-1} E_{\alpha,\alpha}[-(\bar{\gamma} - \gamma'^2) t^\alpha],$$

where $E_{\alpha,\alpha}$ is the Mittag-Leffler function that is generally defined as:

$$E_{\alpha,\beta}[x] = \sum_{k=0}^{\infty} \frac{x^k}{\Gamma(k\alpha + \beta)}, \qquad \alpha, \beta > 0.$$

Note that for $\alpha = \beta = 1$, it is equivalent to the exponential function. Therefore the general solution to the average polarization is given by:

$$\frac{\mu(t)}{\epsilon\alpha'\gamma' - \bar{\alpha}} = \int_0^t \frac{E_{\alpha,\alpha}[-(\bar{\gamma} - \gamma'^2)(t-\tau)^\alpha]}{(t-\tau)^{1-\alpha}} u(\tau) d\tau.$$

Particularly, the step response waveform (in response to $u(t) = u(0^+)\sum_{k=0}^{\infty}(-1)^k H(t - t_k)$, where $H(t)$ is the Heaviside function) reads:

$$\mu(t) = u(0^+)\frac{\epsilon\alpha'\gamma' - \bar{\alpha}}{\bar{\gamma} - \gamma'^2} \times \sum_{k=0}^{\infty}(-1)^k\Big(1 - E_{\alpha,1}[-(\bar{\gamma} - \gamma'^2)(t - t_k)^{\alpha}]\Big). \tag{4.45}$$

We found that a fractional order of $\alpha = 1.01$ successfully describes the results obtained via direct numerical simulations, see figure 4.9. Alternatively, we could numerically evaluate equation (4.44) using a finite difference numerical scheme [205, 204] which is basically to discretize Caputo derivative of order $0 < \alpha < 1$ using,

$${}_0^C D_t^{\alpha} f(t_{n+1}) \approx \frac{(\Delta t)^{-\alpha}}{\Gamma(2-\alpha)}\sum_{j=0}^{n} a_j\big(f_{n+1-j} - f_{n-j}\big),$$

where $a_j = (j+1)^{1-\alpha} - j^{1-\alpha}$ and $f_j = f(t_j)$. Also, for $1 < \alpha < 2$ the discretization reads (*c.f.* see equation 1.5 of Sun and Wu (2006) [206]):

$${}_0^C D_t^{\alpha} f(t_{n+1}) \approx \frac{(\Delta t)^{-\alpha}}{\Gamma(3-\alpha)}\Bigg[f_{n+1} - f_n - b_{n-1}f'(0)\Delta t - \sum_{j=1}^{n-1}(b_{n-j-1} - b_{n-j})(f_j - f_{j-1})\Bigg],$$

where $b_j = (j+1)^{2-\alpha} - j^{2-\alpha}$ (see figure 4.9 for comparison).

4.5 Predictions & Discussions

In this section we perform eight experiments based on the proposed model with the specifications given in tables 4.1–4.2. In each experiment, we apply a Gaussian electric

pulse given by:

$$E_{ext}(t) = E_0 \exp\left(-6\frac{(t - t_f/3)^2}{t_f^2}\right),$$

where $E_0 = 40\ [kV/m]$ for a duration of $t_f = 20\ [\mu s]$ to resolve electric response at smaller frequencies; note that the biggest frequency is determined by the maximum time-step size of integration, which we limit to 1 $[ns]$, while the smallest frequency is inversely proportional to duration of integration. Then impedance can be computed by equation 4.29.

We performed numerical integrations of the integer order system of ordinary differential equations 4.41 with the publicly available package `Scipy` [207] with adaptive time stepping. In particular, we used `LSODA` algorithm, which automatically detects stiffness and switches between the non-stiff Adam and stiff BDF integration methods [208]. The fractional order ODEs 4.44 are solved by implementing the discretization schemes discussed in subsection 4.4.3. The source code to solve the set of equations proposed in this manuscript and to reproduce the results of this section can be found at https://github.com/pourion/CAEP.

4.5.1 Time-domain response

Figure 4.11 illustrates the evolution of the instantaneous effective conductivity, current, resistance, and average value of the membrane and the cytoplasm polarizations during the application of the external Gaussian pulse. To make these predictions, we considered an integer order time derivative, *i.e.* $\alpha = 1$.

At low membrane conductance (configurations I and II), we find that even though the magnitude of the cytoplasm polarization is negligible with respect to the membrane

Table 4.1: *List of theoretical experiments based on the proposed framework. We consider a cell aggregate confined in a cubic box with side length* 1 $[mm]$.

#	$\sigma_c\ [S/m]$	$\sigma_e\ [S/m]$	$S_L\ [S/m^2]$	ϕ	α
I	1.3	0.6	1.9	0.3	1
II	0.6	1.3	1.9	0.3	1
III	1.3	0.6	1.9×10^5	0.3	1
IV	1.3	0.6	1.9×10^5	0.6	1

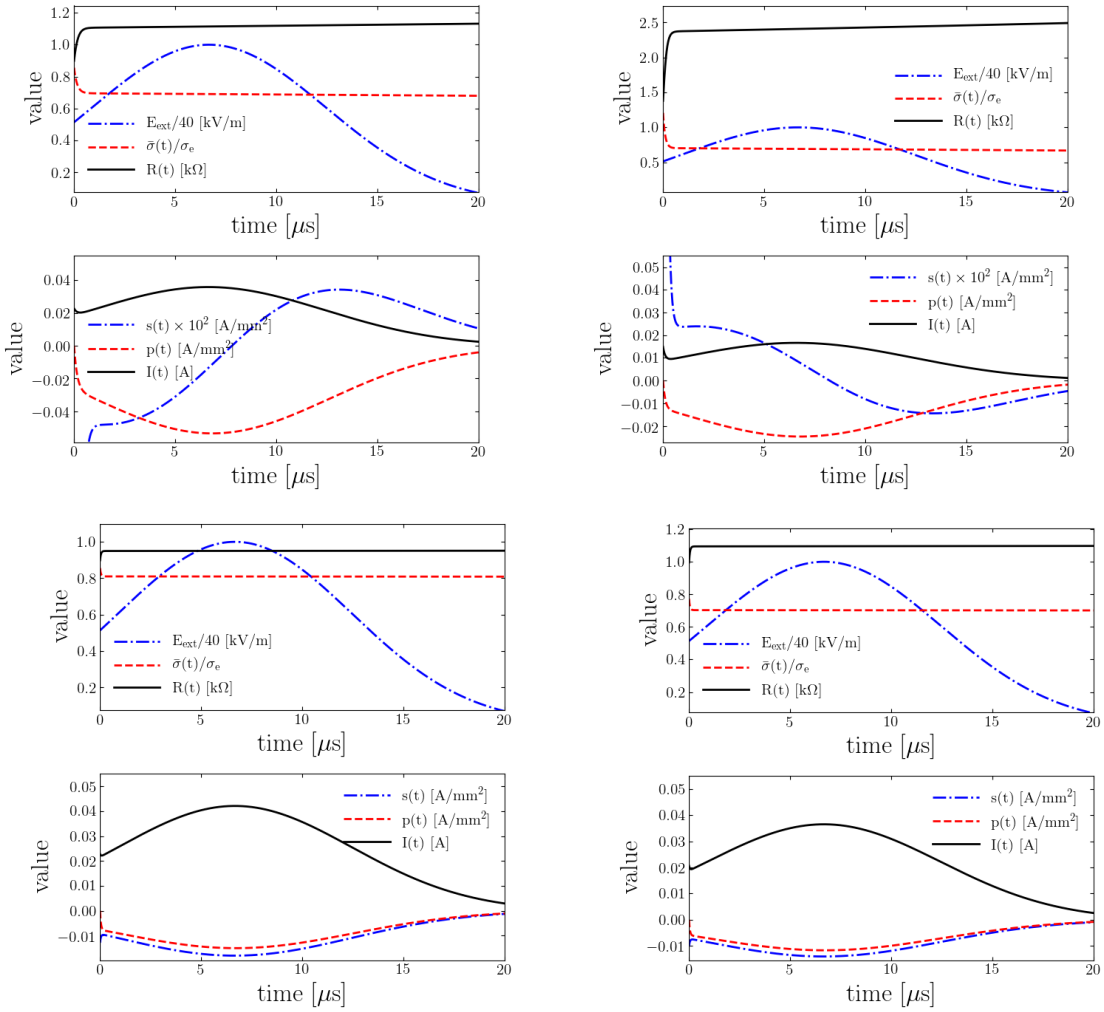

Figure 4.11: *Top left: configuration I. Top right: configuration II. Bottom left: configuration III. Bottom right: configuration IV. Experiments in the time domain.*

Table 4.2: *List of theoretical experiments based on the proposed framework. We consider a cell aggregate confined in a cubic box with side length* 1 $[mm]$*. In each case we chose* 10 *different values for the varying parameter.*

#	σ_c $[S/m]$	σ_e $[S/m]$	S_L $[S/m^2]$	ϕ	α
V	0.6	1.3	1.9	$[0.01, 0.8]$	1
VI	1.0	$[0.5, 1.5]$	1.9	0.3	1
VII	0.6	1.3	$[1.9, 1.9 \times 10^5]$	0.3	1
VIII	0.6	1.3	1.9	0.3	$[0.9, 1.1]$

polarization, over time the cytoplasm dipole moment changes direction from anti-parallel to parallel with respect to the external field, which leads to a slowly increasing resistance felt at the electrodes. However, increasing the membrane conductance (configurations III and IV) has the effect of increasing the cytoplasm polarization at the expense of reducing the membrane polarization while both dipole moments remain anti-parallel to the external field. Increasing the membrane conductance enhances the overall current density and reduces the overall electric resistance of the aggregate.

We have shown how to compute the impedance directly from the time-domain FPE, which paves the way for more detailed studies of cell aggregates with nonlinear membrane processes such as the case of electroporation.

4.5.2 Impedance spectroscopy

The purpose of this section is to understand the impedance as a function of frequency within cell aggregates. This analysis is important because it enables the resolution of the polarization processes and to relate them to their relaxation timescales, *cf.* see the review by Asami (2002) [115]. For example impedance spectroscopy is widely used as a technique to characterize ionic conductors, electroceramics, solid electrolytes, dielectric

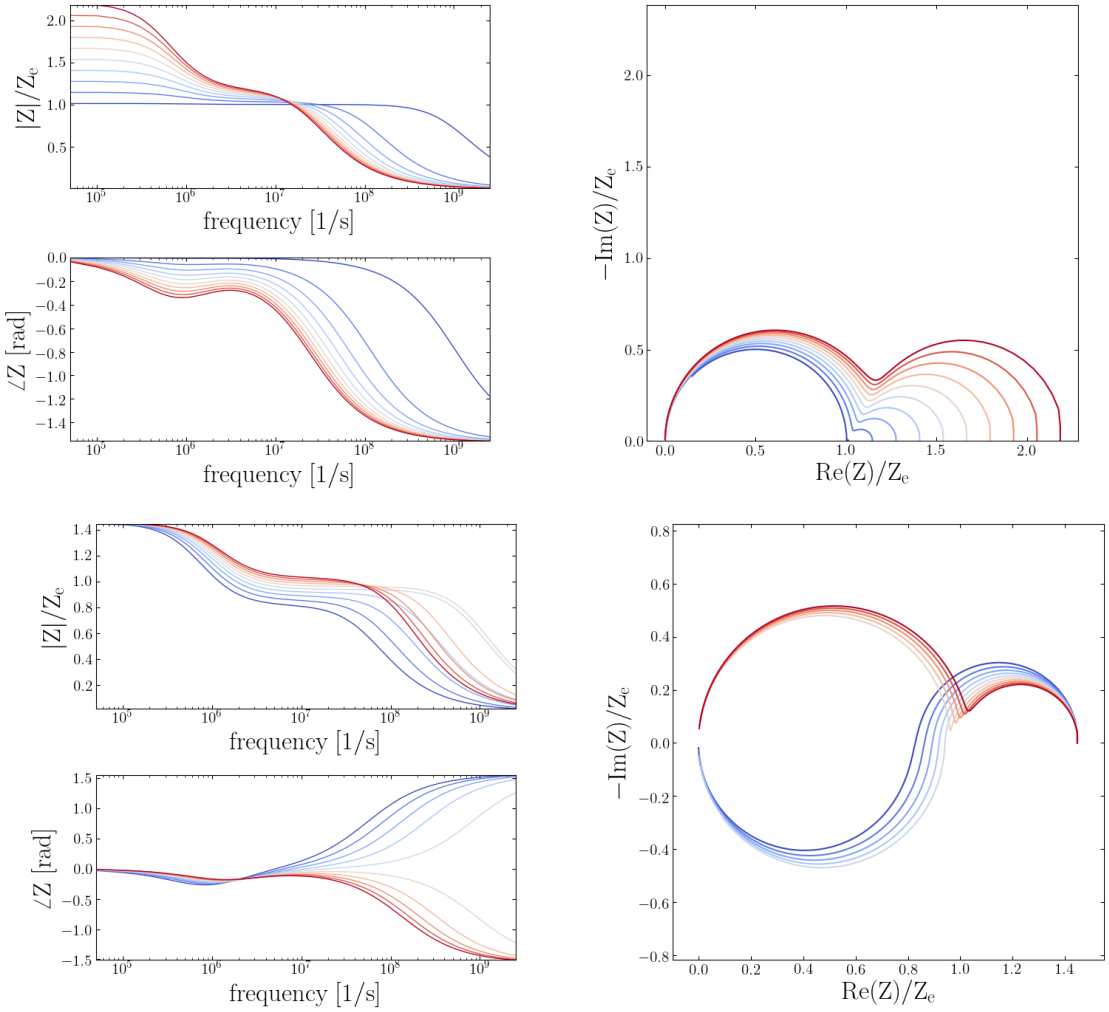

Figure 4.12: *Top panel: configuration V - varying the volume fraction. Bottom panel: configuration VI - varying the extra-cellular matrix conductivity. Experiments in the frequency domain, in all figures warmer colors indicate higher values. Figure (a,b) show the effect of increasing volume fraction from* $\phi = 0.01$ *to* $\phi = 0.8$. *Figures (c,d) illustrate effects of increasing matrix conductivity in the range* $\sigma_e = 0.5$ $[S/m]$ *to* $\sigma_e = 1.5$ $[S/m]$ *while cytoplasm conductivity is fixed at* $\sigma_c = 1$ $[S/m]$. *Red colors correspond to the case of* $\sigma_e > \sigma_c$ *while blue colors correspond to* $\sigma_e < \sigma_c$.

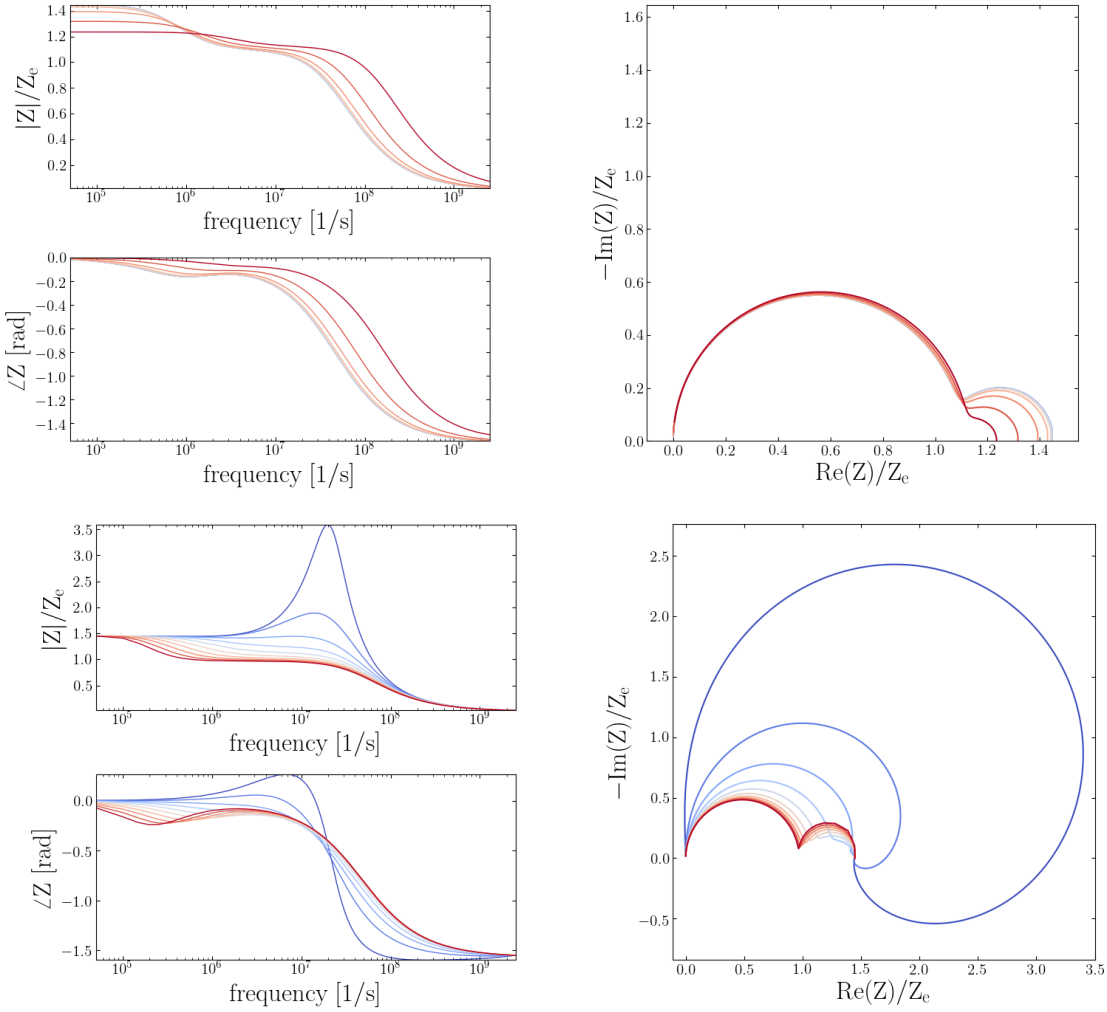

Figure 4.13: *Top panel: configuration VII - varying the membrane conductance. Bottom panel: configuration VIII - varying the fractional order. Experiments in the time domain, in all figures warmer colors correspond to higher values. Figures (a,b) capture the effect of increasing the membrane conductance from* $S_L = 1.9$ $[S/m^2]$ *(bluer colors) to* $S_L = 1.9 \times 10^5$ $[S/m^2]$ *(redder colors). Figures (c,d) illustrate the effects of increasing the fractional order from* $\alpha = 0.9$ *to* $\alpha = 1.1$. *Note that the curves for* $\alpha < 1$ *are shown in blue, while for* $\alpha > 1$ *red colors are used.*

materials such as polymers and glasses as well as fuel cells and batteries [209, 210, 211].

Figures 4.12–4.13 show the Bode and Cole diagrams calculated by equation (4.29) for 4 different configurations and illustrate the effects caused by varying the volume fraction, the matrix conductivity, the membrane conductance and the order of the fractional derivative.

In top panel of figure 4.12, we gradually increase the volume fraction from $\phi = 1\%$ to 80% that increases the impedance at lower frequencies and reduces it at higher frequencies. More importantly, increasing the volume fraction appears to amplify a low-frequency semi-circle in the Cole diagram originating from cell membranes.

In bottom panel of figure 4.12, we change the matrix conductivity while keeping the other parameters fixed. We find that when the matrix is more conductive than the cytoplasm, the dielectric response of the cytoplasm lags behind that of the applied pulse. However for a cytoplasm more conductive than the matrix, we find that the cytoplam dielectric response leads the applied pulse. The latter behavior resembles the dielectric response of an inductive element that appears at high frequencies.

In top panel of figure 4.13, we gradually increase the membrane conductance and find that the semi-circle arc at low frequency gradually shrinks. The characteristic behavior of the present model is that the membrane determines the low frequency arc while the cytoplasm determines the high frequency arc.

In bottom panel of figure 4.13, we vary the order of the fractional derivative. For $0 < \alpha < 1$, we observe a *low frequency hook* effect, where an apparently inductive loop appears at low frequencies, *i.e.* where the imaginary part of impedance becomes positive. In particular, we observe that our model predicts that, by increasing α towards 1, the low frequency hook gradually shrinks, and the low frequency semi-circle becomes depressed. Interestingly, Cole and Baker (1941) [212] reported an inductive response in their experiments with squid axons. Cole and Baker argued that inductive effects

originated from the membrane of axons, which they modeled by an equivalent circuit composed of a resistor in series with an inductor that are connected in parallel with a capacitor. For a detailed discussion on the possible origins of inductive hooks we refer to Klotz (2019) [213]. In fact, low frequency inductive impedance is ubiquitously found in impedance spectroscopy experiments with various systems such as Lithium ion batteries [214], proton exchange membrane fuel cells [215], organic light emitting diodes (LEDs) [216], Perovskite solar cells [217], thin films on conductive substrates [218], and corrosion of Chromium [219]. It is well known that tissue impedance follows a depressed Cole (1940) equation,

$$Z(\omega) = R + \frac{R_0 - R_\infty}{1 + (j\omega/\omega_0)^\alpha},$$

where ω_0 is the angular turnover frequency and α is a dimensionless number between zero and one [220, 122, 221]. It is generally established that it is the diversity of relaxation timescales that is responsible for the observed anomalous electric response of tissue environments [222], which is the source of fractional order evolution in our model as well.

4.6 Conclusion

We have developed a theoretical framework based on a dipole decomposition of cell polarization into two parts: the membrane polarization, and the cytoplasm polarization. Based on this decomposition, we were able to evaluate effective properties of the aggregate environment such as effective conductivity and impedance. We also derived a time-domain governing Fokker-Planck equation that explains distributions of cellular polarizations in different volume fractions and at different frequencies. We showed that the effects of cell interactions can be easily included in the model. Our theory is

generally applicable to triphasic structures that are ubiquitously found in nature, for example in modeling suspensions of biological cells and subcellular organella such as yeasts [223, 224], E. coli [225], synaptosomes [226], and mitochondria [227]. The current work can be extended in several ways:

- In plants and micro-organisms, cells are covered by a cell wall that adds another layer to the dielectric structure; for details see Carstensen (1960) [228]. Hanai *et al.* [229, 230] showed the number of interfaces corresponds to the number of relaxations in the dielectric response of a heterogeneous system, which could explain how diversity in the dielectric properties of cells leads to anomalous relaxation. Therefore an extension of the current theory for multishell structures would be to develop N-phase interfacial polarization theories.

- Coupling the bulk relaxation processes in tissue environments, such as counterion polarization effects, with the interfacial polarization. In particular it was argued [132] that counterion polarization effects contribute to the observed anomalous relaxation; thus it will be useful to examine such influences on the distribution of induced transmembrane potentials.

- Under strong electric fields, nonlinear cellular phenomena occur. A well known example is the membrane breakdown that occurs under transmembrane potentials of about $\mathrm{V_{ep}} = 0.2$ [V], in a process referred to as electroporation [106, 125]. Other phenomena include mechanical effects such as the alignment of non-spherical cells with an applied field, or the swelling effects due to water uptake caused by an increase in the membrane permeability.

- Another interesting extension would be to consider the effects of gap junctions on the induced transmembrane potentials. Gap junctions are electrical connections

between neighboring cells that provide direct pathways for ion transport in multicellular systems. Gap junctions are key regulators for embryonic development due to their ability to regulate transmembrane voltages; therefore understanding their interplay with an external electric stimulation poses new opportunities to control embryonic development and a new pathway to understand and control patterning in biological organisms.

Acknowledgement

Part of this research was funded by ARO W911NF-16-1-0136. The direct numerical simulations performed in this work used the Extreme Science and Engineering Discovery Environment (XSEDE), which is supported by National Science Foundation grant number ACI-1053575 and ASC-150002. The authors acknowledge the Texas Advanced Computing Center (TACC) at The University of Texas at Austin for providing HPC and visualization resources that have contributed to the research results reported within this paper.

Bibliography

[1] P. Mistani, A. Guittet, D. Bochkov, J. Schneider, D. Margetis, C. Ratsch, and F. Gibou, *The island dynamics model on parallel quadtree grids*, *Journal of Computational Physics* (2017).

[2] P. Mistani, A. Guittet, C. Poignard, and F. Gibou, *A parallel voronoi-based approach for mesoscale simulations of cell aggregate electropermeabilization*, *Journal of Computational Physics* **380** (2019) 48–64.

[3] P. Mistani, S. Pakravan, and F. Gibou, *A fractional stochastic theory for nonlinear electroporation of cell aggregates*, *in preparation*.

[4] S. Pakravan, P. A. Mistani, M. A. Aragon-Calvo, and F. Gibou, *Solving inverse-pde problems with physics-aware neural networks*, *arXiv preprint arXiv:2001.03608* (2020).

[5] P. Mistani, S. Pakravan, and F. Gibou, *Towards a tensor network representation of complex systems*, in *Sustainable Interdependent Networks II*, pp. 23–39. Springer, 2019.

[6] P. Mistani, S. Pakravan, and F. Gibou, *Tensor network renormalization as an ultra-calculus for complex systems dynamics*, in *Sustainable Interdependent Networks II*, pp. 40–57. Springer, 2019.

[7] H.-C. Jeong and E. D. Williams, *Steps on surfaces: experiment and theory*, *Surf. Sci. Rep* **34** (1999) 171–294.

[8] A. Pimpinelli and J. Villain, *Physics of Crystal Growth*. Cambridge University Press, Cambridge, UK, 1999.

[9] J. Krug, P. Politi, and T. Michely, *Island nucleation in the presence of step-edge barriers: Theory and applications*, *Phys. Rev. B* **61** (2000) 14037.

[10] W. Barvosa-Carter Private communication.

[11] R. Caflisch, M. Gyure, B. Merriman, S. Osher, C. Ratsch, D. Vvedensky, and J. Zinck, *Island dynamics and the level set method for epitaxial growth*, *Applied Mathematics Letters* **12** (1999) 13.

[12] C. Ratsch, M. F. Gyure, R. E. Caflisch, F. Gibou, M. Petersen, M. Kang, J. Garcia, and D. D. Vvedensky, *Level-set method for island dynamics in epitaxial growth*, *Phys. Rev. B* **65** (2002) 195403.

[13] W. K. Burton, N. Cabrera, and F. C. Frank, *The growth of crystals and the equilibrium structure of their surfaces*, *Philos. Trans. R. Soc. London Ser. A* **243** (1951) 299–358.

[14] M. Mirzadeh, A. Guittet, C. Burstedde, and F. Gibou, *Parallel level-set methods on adaptive tree-based grids*, *J. Comput. Phys.* **322** (2016) 345–364.

[15] C. Min and F. Gibou, *A second order accurate level set method on non-graded adaptive Cartesian grids*, *J. Comput. Phys.* **225** (2007) 300–321.

[16] C. Burstedde, L. C. Wilcox, and O. Ghattas, *`p4est`: Scalable algorithms for parallel adaptive mesh refinement on forests of octrees*, *SIAM Journal on Scientific Computing* **33** (2011), no. 3 1103–1133.

[17] H.-J. Ernst, F. Fabre, R. Folkerts, and J. Lapujoulade, *Observation of a growth instability during low temperature molecular beam epitaxy* , *Phys. Rev. Lett.* **72** (1994) 112–115.

[18] J.-K. Zuo and J. F. Wendelken, *Evolution of mound morphology in reversible homoepitaxy on Cu(100)*, *Phys. Rev. Lett.* **78** (1997) 2791–2794.

[19] J. A. Stroscio, D. T. Pierce, M. D. Stiles, A. Zangwill, and L. M. Sander, *Coarsening of unstable surface features during Fe(001) homoepitaxy*, *Phys. Rev. Lett.* **75** (1995) 4246–4249.

[20] J. Wollschläger, E. Z. Luo, and M. Henzler, *Diffraction characterization of rough films formed under stable and unstable growth conditions*, *Phys. Rev. B* **57** (1998) 15541–15552.

[21] M. Bott, T. Michely, and G. Comsa, *The homoepitaxial growth of Pt on Pt(111) studied with STM*, *Surf. Sci.* **272** (1992) 161–166.

[22] G. Ehrlich and F. Hudda, *Atomic view of surface self-diffusion: Tungsten on tungsten*, *J. Chem. Phys.* **44** (1966) 1039.

[23] R. L. Schwoebel and E. J. Shipsey, *Step motion on crystal surfaces*, *J. Appl. Phys.* **37** (1966) 3682–3686.

[24] D. Vanderbilt and L. K. Wickham, *Evolution of thin film and surface microstructure.*, in *MRS, Pittsburgh* (J. Y. T. Thompson and D. J. Srolovitz, eds.), p. 155. 1991.

[25] A. D. Yoffe, *Low-dimensional systems: quantum size effects and electronic properties of semiconductor microcrystallites (zero-dimensional systems) and some quasi-two-dimensional systems*, *Adv. Phys.* **42** (1993) 173–262.

[26] J. Langer, *Instability and pattern formation in crystal growth*, *Rev. of Mod. Phys.* **52** (1980) 1–28.

[27] in *Multiscale Modeling in Epitaxial Growth* (A. Voigt, ed.). Birkhäuser Verlag, Basel, 2004.

[28] T. Michely and J. Krug, *Islands, Mounds and Atoms: Patterns and Processes in Crystal Growth Far from Equilibrium*. Springer-Verlag, 2004.

[29] R. E. Caflisch, *Growth, structure and pattern formation for thin films*, *J. Sci. Comput.* **37** (2008) 3–17.

[30] S. Chen, M. Kang, B. Merriman, R. Caflisch, C. Ratsch, R. Fedkiw, M. Gyure, and S. Osher, *Level set method for thin film epitaxial growth*, *Journ. Comp. Phys.* **167** (2001) 475.

[31] C. Ratsch, M. Gyure, S. Chen, M. Kang, and D. Vvedensky, *Fluctuation and Scaling in Aggregation Phenomena*, *Phys. Rev. B* **61** (2000) R10598.

[32] X. Niu, R. Vardavas, R. Caflisch, and C. Ratsch, *A Level Set Simulation of Directed Self-Assembly during Epitaxial Growth* , *Phys. Rev. B* **74** (2006) 193403.

[33] F. Gibou, C. Ratsch, S. Chen, M. Gyure, and R. Caflisch, *Rate Equations and Capture Numbers with Implicit Island Correlations*, *Phys. Rev. B.* **63** (2001) 115401.

[34] D. Vvedensky, C. Ratsch, F. Gibou, and R. Vardavas, *Singularities and spatial fluctuations in submonolayer epitaxy*, *Phys. Rev. Lett.* **90** (2003) 189601.

[35] A. A. Chernov, *The spiral growth of crystals*, *Soviet Phys. Uspekhi* **4** (1961) 116–148.

[36] G. S. Bales and D. C. Chrzan, *Dynamics of irreversible island growth during submonolayer epitaxy*, *Phys. Rev. B* **50** (1994) 6057–6067.

[37] F. Gibou, C. Ratsch, and R. Caflisch, *Capture numbers in rate equations and scaling laws for epitaxial growth*, *Phys. Rev. B.* **67** (2003) 155403.

[38] J. Villain, *Continuum models of crystal growth from atomic beams with and without desorption*, *J. Phys. (France) I* **1** (1991) 19–42.

[39] J. Lu, J.-G. Liu, and D. Margetis, *Emergence of step flow from an atomistic scheme of epitaxial growth in 1 + 1 dimensions*, *Phys. Rev. E* **91** (2015) 032403.

[40] P. Šmilauer and D. D. Vvedensky, *Coarsening and slope evolution during unstable epitaxial growth*, *Phys. Rev. B* **52** (1995) 14263–14272.

[41] R. E. Caflisch, W. E, M. F. Gyure, B. Merriman, and C. Ratch, *Kinetic model for a step edge in epitaxial growth*, *Phys. Rev. E* **59** (1999) 6879–6887.

[42] J. Papac, F. Gibou, and C. Ratsch, *Efficient symmetric discretization for the Poisson, heat and Stefan-type problems with Robin boundary conditions*, *J. Comput. Phys.* **229** (2010) 875–889.

[43] S. Paulin, F. Gillet, O. Pierre-Louis, and C. Misbah, *Unstable step meandering with elastic interactions*, *Phys. Rev. Lett.* **86** (2001) 5538–5541.

[44] S. Osher and J. A. Sethian, *Fronts propagating with curvature dependent speed: algorithms based on Hamilton-Jacobi formulations*, *J. Comput. Phys.* **79** (1988), no. 1 12–49.

[45] M. Sussman, P. Smereka, and S. Osher, *A level set approach for computing solutions to incompressible two-phase flow*, *J. Comp. Phys.* **114** (1994) 146–159.

[46] G. Russo and P. Smereka, *A remark on computing distance functions*, *J. Comput. Phys.* **163** (2000) 51–67.

[47] H. Chen, C. Min, and F. Gibou, *A supra-convergent finite difference scheme for the Poisson and heat equations on irregular domains and non-graded adaptive Cartesian grids*, *J. Sci. Comput.* **31** (2007) 19–60.

[48] H. Chen, C. Min, and F. Gibou, *A numerical scheme for the Stefan problem on adaptive Cartesian grids with supralinear convergence rate*, *J. Comput. Phys.* **228** (2009), no. 16 5803–5818.

[49] A. Helgadóttir and F. Gibou, *A Poisson-Boltzmann solver on irregular domains with Neumann or Robin boundary conditions on non-graded adaptive grid*, *J. Comput. Phys.* **230** (2011) 3830–3848.

[50] J. Papac, A. Helgadottir, C. Ratsch, and F. Gibou, *A level set approach for diffusion and stefan-type problems with Robin boundary conditions on quadtree/octree adaptive cartesian grids*, *J. Comput. Phys.* **233** (2013) 241–261.

[51] H. Samet, *The Design and Analysis of Spatial Data Structures*. Addison-Wesley, New York, 1989.

[52] H. Samet, *Applications of Spatial Data Structures: Computer Graphics, Image Processing and GIS*. Addison-Wesley, New York, 1990.

[53] C. Min, F. Gibou, and H. Ceniceros, *A supra-convergent finite difference scheme for the variable coefficient Poisson equation on non-graded grids*, *J. Comput. Phys.* **218** (2006) 123–140.

[54] C. Min and F. Gibou, *Geometric integration over irregular domains with application to level set methods*, *J. Comput. Phys.* **226** (2007) 1432–1443.

[55] H. Chen, C. Min, and F. Gibou, *A second-order accurate FDM for the heat equation on irregular domains and adaptive grids*, in *Proceedings of the Materials Research Society Symposium, San Francisco, CA, USA*, vol. 910, pp. 907–910, 2006.

[56] F. Gibou, R. Fedkiw, L.-T. Cheng, and M. Kang, *A second-order accurate symmetric discretization of the Poisson equation on irregular domains*, *J. Comput. Phys.* **176** (2002) 205–227.

[57] G. H. Shortley and R. Weller, *Numerical solution of Laplace's equation*, *J. Appl. Phys.* **9** (1938) 334–348.

[58] C.-W. Shu and S. Osher, *Efficient implementation of essentially non-oscillatory shock capturing schemes II*, *J. Comput. Phys.* **83** (1989) 32–78.

[59] X.-D. Liu, S. Osher, and T. Chan, *Weighted essentially non-oscillatory schemes*, *J. Comput. Phys.* **126** (1996) 202–212.

[60] P. Šmilauer and D. D. Vvedensky, *Coarsening and slope evolution during unstable spitaxial growth*, *Phys. Rev. B* **52** (1995) 14263–14272.

[61] M. C. Bartelt and J. W. Evans, *Transition to multilayer kinetic roughening for metal (100) homoepitaxy*, *Phys. Rev. Lett.* **75** (Dec, 1995) 4250–4253.

[62] J. J. Belehradek, S. Orlowski, L. H. Ramirez, G. Pron, B. Poddevin, and L. M. Mir, *Electropermeabilization of cells in tissues assessed by the qualitative and quantitative electroloading of bleomycin*, *Biochimica et Biophysica Acta (BBA)-Biomembranes* **1190** (1994), no. 1 155–163.

[63] J. McMahon, E. Signori, K. Wells, V. Fazio, and D. Wells, *Optimisation of electrotransfer of plasmid into skeletal muscle by pretreatment with hyaluronidase-increased expression with reduced muscle damage*, *Gene therapy* **8** (2001), no. 16 1264.

[64] K. A. DeBruin and W. Krassowska, *Modeling electroporation in a single cell. i. effects of field strength and rest potential*, *Biophysical Journal* **77** (1999), no. 3 1213 – 1224.

[65] W. Krassowska and P. D. Filev, *Modeling electroporation in a single cell*, *Biophysical Journal* **92** (2007), no. 2 404 – 417.

[66] J. Li and H. Lin, *Numerical simulation of molecular uptake via electroporation*, *Bioelectrochemistry* **82** (2011), no. 1 10 – 21.

[67] J. Langus, M. Kranjc, B. Kos, T. Šuštar, and D. Miklavčič, *Dynamic finite-element model for efficient modelling of electric currents in electroporated tissue*, .

[68] M. Leguèbe, A. Silve, L. Mir, and C. Poignard, *Conducting and permeable states of cell membrane submitted to high voltage pulses: Mathematical and numerical studies validated by the experiments*, *Journal of Theoretical Biology* (2014).

[69] D. Voyer, A. Silve, L. M. Mir, R. Scorretti, and C. Poignard, *Dynamical modeling of tissue electroporation*, *Bioelectrochemistry* **119** (2018) 98 – 110.

[70] A. Guittet, C. Poignard, and F. Gibou, *A voronoi interface approach to cell aggregate electropermeabilization*, *Journal of Computational Physics* **332** (2017) 143–159.

[71] R. P. Fedkiw, T. Aslam, B. Merriman, and S. Osher, *A non-oscillatory eulerian approach to interfaces in multimaterial flows (the ghost fluid method)*, *Journal of Computational Physics* **152** (1999), no. 2 457 – 492.

[72] M. Kang, R. P. Fedkiw, and X.-D. Liu, *A boundary condition capturing method for multiphase incompressible flow*, *Journal of Scientific Computing* **15** (Sep, 2000) 323–360.

[73] X.-D. Liu and T. Sideris, *Convergence of the ghost fluid method for elliptic equations with interfaces*, *Mathematics of computation* **72** (2003), no. 244 1731–1746.

[74] R. E. English, L. Qiu, Y. Yu, and R. Fedkiw, *An adaptive discretization of incompressible flow using a multitude of moving cartesian grids*, *Journal of Computational Physics* **254** (2013) 107–154.

[75] S. Osher and J. A. Sethian, *Fronts propagating with curvature-dependent speed: Algorithms based on hamilton-jacobi formulations*, *Journal of Computational Physics* **79** (1988), no. 1 12 – 49.

[76] F. Gibou, R. Fedkiw, and S. Osher, *A review of level-set methods and some recent applications*, *Journal of Computational Physics* **353** (2018), no. Supplement C 82 – 109.

[77] R. A. Finkel and J. L. Bentley, *Quad trees a data structure for retrieval on composite keys*, *Acta Informatica* **4** (Mar, 1974) 1–9.

[78] D. Meagher, *Geometric modeling using octree encoding*, *Computer Graphics and Image Processing* **19** (1982), no. 2 129 – 147.

[79] J. Strain, *Tree methods for moving interfaces*, *Journal of Computational Physics* **151** (1999), no. 2 616–648.

[80] C. Min, *Local level set method in high dimension and codimension*, *Journal of computational physics* **200** (2004), no. 1 368–382.

[81] M. Mirzadeh, A. Guittet, C. Burstedde, and F. Gibou, *Parallel level-set methods on adaptive tree-based grids*, *Journal of Computational Physics* **322** (2016) 345 – 364.

[82] C. Burstedde, L. C. Wilcox, and O. Ghattas, *p4est: Scalable algorithms for parallel adaptive mesh refinement on forests of octrees*, *SIAM Journal on Scientific Computing* **33** (2011), no. 3 1103–1133.

[83] G. Levy, *An introduction to quasi-random numbers*, *Numerical Algorithms Group Ltd.* (2002).

[84] J. H. Halton, *On the efficiency of certain quasi-random sequences of points in evaluating multi-dimensional integrals*, *Numerische Mathematik* **2** (Dec, 1960) 84–90.

[85] E. Braaten and G. Weller, *An improved low-discrepancy sequence for multidimensional quasi-monte carlo integration*, *Journal of Computational Physics* **33** (1979), no. 2 249 – 258.

[86] W. H. Press, S. A. Teukolsky, W. T. Vetterling, and B. P. Flannery, *Numerical Recipes in FORTRAN; The Art of Scientific Computing*. Cambridge University Press, New York, NY, USA, 2nd ed., 1993.

[87] A. Guittet, M. Lepilliez, S. Tanguy, and F. Gibou, *Solving elliptic problems with discontinuities on irregular domains – the voronoi interface method*, *Journal of Computational Physics* **298** (2015) 747 – 765.

[88] C. H. Rycroft, *Voro++: A three-dimensional voronoi cell library in C++*, *Chaos: An Interdisciplinary Journal of Nonlinear Science* **19** (2009), no. 4 041111.

[89] E. Nagel, *The structure of science*, .

[90] J. Butterfield, *Less is different: Emergence and reduction reconciled*, *Foundations of Physics* **41** (2011), no. 6 1065–1135.

[91] J. Butterfield, *Emergence, reduction and supervenience: a varied landscape*, *Foundations of Physics* **41** (2011), no. 6 920–959.

[92] L. P. Kadanoff, *Relating theories via renormalization*, *Studies in History and Philosophy of Science Part B: Studies in History and Philosophy of Modern Physics* **44** (2013), no. 1 22–39.

[93] J. Butterfield and N. Bouatta, *Renormalization for philosophers*, *Metaphysics in Contemporary Physics* **104** (2015) 437–485.

[94] M. Bedau, *Downward causation and the autonomy of weak emergence*, *Principia* **6** (2002), no. 1 5.

[95] C. A. Fulmer and C. Ostroff, *Convergence and emergence in organizations: An integrative framework and review*, *Journal of Organizational Behavior* **37** (2016), no. S1.

[96] L. Wasungu, J.-M. Escoffre, A. Valette, J. Teissie, and M.-P. Rols, *A 3d in vitro spheroid model as a way to study the mechanisms of electroporation*, *International Journal of Pharmaceutics* **379** (2009), no. 2 278 – 284. Challenges for Nanotechnology in Delivery Imaging.

[97] G. Pucihar, T. Kotnik, J. Teissié, and D. Miklavčič, *Electropermeabilization of dense cell suspensions*, *European Biophysics Journal* **36** (2007), no. 3 173–185.

[98] U. Zimmermann, *Electric field-mediated fusion and related electrical phenomena*, *Biochimica et Biophysica Acta (BBA)-Reviews on Biomembranes* **694** (1982), no. 3 227–277.

[99] C. A. Jordan, E. Neumann, and A. E. Sowers, *Electroporation and electrofusion in cell biology*. Springer Science & Business Media, 2013.

[100] W. Arnold and U. Zimmermann, *Electric field-induced fusion and rotation of cells*, *Biological membranes* **5** (1984) 389–454.

[101] G. Fuhr, R. Glaser, and R. Hagedorn, *Rotation of dielectrics in a rotating electric high-frequency field. model experiments and theoretical explanation of the rotation effect of living cells*, *Biophysical journal* **49** (1986), no. 2 395–402.

[102] H. A. Pohl and J. S. Crane, *Dielectrophoresis of cells*, *Biophysical journal* **11** (1971), no. 9 711–727.

[103] F. A. Sauer, *Forces on suspended particles in the electromagnetic field*, in *Coherent excitations in biological systems*, pp. 134–144. Springer, 1983.

[104] F. F. Becker, X.-B. Wang, Y. Huang, R. Pethig, J. Vykoukal, and P. Gascoyne, *Separation of human breast cancer cells from blood by differential dielectric affinity*, *Proceedings of the National Academy of Sciences* **92** (1995), no. 3 860–864.

[105] P. R. Gascoyne and J. Vykoukal, *Particle separation by dielectrophoresis*, *Electrophoresis* **23** (2002), no. 13 1973.

[106] E. Neumann and K. Rosenheck, *Permeability changes induced by electric impulses in vesicular membranes*, *The Journal of membrane biology* **10** (1972), no. 1 279–290.

[107] K. Kaler and T. Jones, *Dielectrophoretic spectra of single cells determined by feedback-controlled levitation.*, *Biophysical journal* **57** (1990), no. 2 173.

[108] G. Bryant and J. Wolfe, *Electromechanical stresses produced in the plasma membranes of suspended cells by applied electric fields*, *The Journal of membrane biology* **96** (1987), no. 2 129–139.

[109] G. H. Markx and C. L. Davey, *The dielectric properties of biological cells at radiofrequencies: applications in biotechnology*, *Enzyme and Microbial Technology* **25** (1999), no. 3-5 161–171.

[110] M. Levin, G. Pezzulo, and J. M. Finkelstein, *Endogenous bioelectric signaling networks: exploiting voltage gradients for control of growth and form*, *Annual review of biomedical engineering* **19** (2017) 353–387.

[111] W. Roux, *Uber die* morphologische˜ polarisation yon eiern und embryonen durch den elektrischen strom, scwie fiber die wirkung des elektrischen stromes auf die richtung der ersten teilung des eies*, *Sitzungsber. der kk Akad. d. Wiss. Wien math. nat. K* **1** 27.

[112] K. B. Hotary and K. R. Robinson, *Evidence of a role for endogenous electrical fields in chick embryo development*, *Development* **114** (1992), no. 4 985–996.

[113] C. E. Pullar, *The physiology of bioelectricity in development, tissue regeneration and cancer*. CRC Press, 2016.

[114] B. Reid and M. Zhao, *The electrical response to injury: molecular mechanisms and wound healing*, *Advances in wound care* **3** (2014), no. 2 184–201.

[115] K. Asami, *Characterization of heterogeneous systems by dielectric spectroscopy*, *Progress in polymer science* **27** (2002), no. 8 1617–1659.

[116] J. Cervera, M. Levin, and S. Mafe, *Bioelectrical coupling of single-cell states in multicellular systems*, *The Journal of Physical Chemistry Letters* **11** (2020), no. 9 3234–3241.

[117] H. P. Schwan, *Electrical properties of tissue and cell suspensions*, in *Advances in biological and medical physics*, vol. 5, pp. 147–209. Elsevier, 1957.

[118] M. Stuchly and S. Stuchly, *Dielectric properties of biological substances?tabulated*, *Journal of Microwave power* **15** (1980), no. 1 19–25.

[119] R. Pethig, *Dielectric properties of biological materials: Biophysical and medical applications*, *IEEE Transactions on Electrical Insulation* (1984), no. 5 453–474.

[120] R. Pethig and D. B. Kell, *The passive electrical properties of biological systems: their significance in physiology, biophysics and biotechnology*, *Physics in Medicine & Biology* **32** (1987), no. 8 933.

[121] K. R. Foster, H. P. Schwan, *et. al.*, *Dielectric properties of tissues*, *CRC handbook of biological effects of electromagnetic fields* 27–96.

[122] E. McAdams and J. Jossinet, *Tissue impedance: a historical overview*, *Physiological measurement* **16** (1995), no. 3A A1.

[123] C. Gabriel, S. Gabriel, and y. E. Corthout, *The dielectric properties of biological tissues: I. literature survey*, *Physics in medicine & biology* **41** (1996), no. 11 2231.

[124] W. Kuang and S. Nelson, *Low-frequency dielectric properties of biological tissues: a review with some new insights*, .

[125] T. Kotnik, L. Rems, M. Tarek, and D. Miklavčič, *Membrane electroporation and electropermeabilization: mechanisms and models*, *Annual review of biophysics* **48** (2019) 63–91.

[126] H. Schwan, G. Schwarz, J. Maczuk, and H. Pauly, *On the low-frequency dielectric dispersion of colloidal particles in electrolyte solution1*, *The Journal of Physical Chemistry* **66** (1962), no. 12 2626–2635.

[127] G. Schwarz, *A theory of the low-frequency dielectric dispersion of colloidal particles in electrolyte solution1, 2*, *The Journal of Physical Chemistry* **66** (1962), no. 12 2636–2642.

[128] C. W. Einolf Jr and E. L. Carstensen, *Low-frequency dielectric dispersion in suspensions of ion-exchange resins*, *The Journal of Physical Chemistry* **75** (1971), no. 8 1091–1099.

[129] C. W. Einolf Jr and E. L. Carstensen, *Passive electrical properties of microorganisms: V. low-frequency dielectric dispersion of bacteria*, *Biophysical journal* **13** (1973), no. 1 8–13.

[130] S. S. Dukhin, V. N. Shilov, and J. Bikerman, *Dielectric phenomena and double layer in disperse systems and polyelectrolytes*, *Journal of the Electrochemical Society* **121** (1974), no. 4 154C.

[131] M. Mandel and T. Odijk, *Dielectric properties of polyelectrolyte solutions*, *Annual Review of Physical Chemistry* **35** (1984), no. 1 75–108.

[132] C. Grosse and K. R. Foster, *Permittivity of a suspension of charged spherical particles in electrolyte solution*, *Journal of Physical Chemistry* **91** (1987), no. 11 3073–3076.

[133] J. C. Maxwell, *A treatise on electricity and magnetism*, vol. 1. Oxford: Clarendon Press, 1873.

[134] K. W. Wagner, *Erklärung der dielektrischen nachwirkungsvorgänge auf grund maxwellscher vorstellungen*, *Archiv für Elektrotechnik* **2** (1914), no. 9 371–387.

[135] H. Fricke, *A mathematical treatment of the electric conductivity and capacity of disperse systems ii. the capacity of a suspension of conducting spheroids surrounded by a non-conducting membrane for a current of low frequency*, *Physical Review* **26** (1925), no. 5 678.

[136] H. Fricke, *The electric permittivity of a dilute suspension of membrane-covered ellipsoids*, *Journal of Applied Physics* **24** (1953), no. 5 644–646.

[137] T. Hanai, *Theory of the dielectric dispersion due to the interfacial polarization and its application to emulsions*, *Kolloid-Zeitschrift* **171** (1960), no. 1 23–31.

[138] T. Hanai, K. Asami, and N. Koizumi, *Dielectric theory of concentrated suspensions of shell-spheres in particular reference to the analysis of biological cell suspensions*, .

[139] H. Zhang, K. Sekine, T. Hanai, and N. Koizumi, *Dielectric observations on polystyrene microcapsules and the theoretical analysis with reference to interfacial polarization*, *Colloid and Polymer Science* **261** (1983), no. 5 381–389.

[140] H. Zhang, K. Sekine, T. Hanai, and N. Koizumi, *Dielectric approach to polystyrene microcapsule analysis and the application to the capsule permeability to potassium chloride*, *Colloid and polymer science* **262** (1984), no. 7 513–520.

[141] T. Hanai, K. Zhao, K. Asaka, and K. Asami, *Theoretical approach and the practice to the evaluation of structural parameters characterizing concentration polarization alongside ion-exchange membranes by means of dielectric measurement*, *Colloid and Polymer Science* **271** (1993), no. 8 766–773.

[142] P. J. W. Debye, *Polar molecules*. Chemical Catalog Company, Incorporated, 1929.

[143] J. Miles Jr and H. Robertson, *The dielectric behavior of colloidal particles with an electric double-layer*, *Physical Review* **40** (1932), no. 4 583.

[144] T. Kotnik, F. Bobanovič, and D. Miklavčič, *Sensitivity of transmembrane voltage induced by applied electric fields – a theoretical analysis*, *Bioelectrochemistry and bioenergetics* **43** (1997), no. 2 285–291.

[145] D. Gross, *Electromobile surface charge alters membrane potential changes induced by applied electric fields*, *Biophysical journal* **54** (1988), no. 5 879–884.

[146] E. Neumann, *The Relaxation Hysteresis of Membrane Electroporation*, pp. 61–82. Springer US, Boston, MA, 1989.

[147] S. Ho and G. Mittal, *Electroporation of cell membranes: a review*, *Critical reviews in biotechnology* **16** (1996), no. 4 349–362.

[148] T. Geng and C. Lu, *Microfluidic electroporation for cellular analysis and delivery*, *Lab on a Chip* **13** (2013), no. 19 3803–3821.

[149] T. Kotnik and D. Miklavčič, *Analytical description of transmembrane voltage induced by electric fields on spheroidal cells*, *Biophysical Journal* **79** (2000), no. 2 670–679.

[150] J. Teissie and M.-P. Rols, *An experimental evaluation of the critical potential difference inducing cell membrane electropermeabilization*, *Biophysical journal* **65** (1993), no. 1 409–413.

[151] R. P. Fedkiw, T. Aslam, B. Merriman, S. Osher, *et. al.*, *A non-oscillatory eulerian approach to interfaces in multimaterial flows (the ghost fluid method)*, .

[152] S. Balay, S. Abhyankar, M. F. Adams, J. Brown, P. Brune, K. Buschelman, L. Dalcin, A. Dener, V. Eijkhout, W. D. Gropp, D. Karpeyev, D. Kaushik, M. G. Knepley, D. A. May, L. C. McInnes, R. T. Mills, T. Munson, K. Rupp, P. Sanan, B. F. Smith, S. Zampini, H. Zhang, and H. Zhang, "PETSc Web page." `https://www.mcs.anl.gov/petsc`, 2019.

[153] S. Balay, S. Abhyankar, M. F. Adams, J. Brown, P. Brune, K. Buschelman, L. Dalcin, A. Dener, V. Eijkhout, W. D. Gropp, D. Karpeyev, D. Kaushik, M. G. Knepley, D. A. May, L. C. McInnes, R. T. Mills, T. Munson, K. Rupp, P. Sanan, B. F. Smith, S. Zampini, H. Zhang, and H. Zhang, *PETSc users manual*, Tech. Rep. ANL-95/11 - Revision 3.13, Argonne National Laboratory, 2020.

[154] S. Balay, W. D. Gropp, L. C. McInnes, and B. F. Smith, *Efficient management of parallelism in object oriented numerical software libraries*, in *Modern Software Tools in Scientific Computing* (E. Arge, A. M. Bruaset, and H. P. Langtangen, eds.), pp. 163–202, Birkhäuser Press, 1997.

[155] H. A. Van der Vorst, *Bi-cgstab: A fast and smoothly converging variant of bi-cg for the solution of nonsymmetric linear systems*, *SIAM Journal on scientific and Statistical Computing* **13** (1992), no. 2 631–644.

[156] R. D. Falgout and U. M. Yang, *hypre: A library of high performance preconditioners*, in *International Conference on Computational Science*, pp. 632–641, Springer, 2002.

[157] C. Burstedde, L. C. Wilcox, and O. Ghattas, *p4est: Scalable algorithms for parallel adaptive mesh refinement on forests of octrees*, *SIAM Journal on Scientific Computing* **33** (2011), no. 3 1103–1133.

[158] C. Rycroft, *Voro++: A three-dimensional voronoi cell library in c++*, tech. rep., Lawrence Berkeley National Lab.(LBNL), Berkeley, CA (United States), 2009.

[159] T. C. Choy, *Effective medium theory: principles and applications*, vol. 165. Oxford University Press, 2015.

[160] A. D. Fokker, *Die mittlere energie rotierender elektrischer dipole im strahlungsfeld*, *Annalen der Physik* **348** (1914), no. 5 810–820.

[161] M. Planck, *Uber einen satz der statistischen dynamik und seine erweiterung in der quantentheorie*, .

[162] D. J. Jeffrey, *Conduction through a random suspension of spheres*, *Proceedings of the Royal Society of London. A. Mathematical and Physical Sciences* **335** (1973), no. 1602 355–367.

[163] G. Batchelor, *Sedimentation in a dilute dispersion of spheres*, *Journal of fluid mechanics* **52** (1972), no. 2 245–268.

[164] G. Batchelor and J.-T. Green, *The hydrodynamic interaction of two small freely-moving spheres in a linear flow field*, *Journal of Fluid Mechanics* **56** (1972), no. 2 375–400.

[165] P. C. Franzone and G. Savaré, *Degenerate evolution systems modeling the cardiac electric field at micro-and macroscopic level*, in *Evolution equations, semigroups and functional analysis*, pp. 49–78. Springer, 2002.

[166] A. Collin and S. Imperiale, *Mathematical analysis and 2-scale convergence of a heterogeneous microscopic bidomain model*, *Mathematical Models and Methods in Applied Sciences* **28** (2018), no. 05 979–1035.

[167] J. Hinch, *A perspective of batchelor's research in micro-hydrodynamics*, *Journal of Fluid Mechanics* **663** (2010) 8–17.

[168] G. Batchelor, *Transport properties of two-phase materials with random structure*, *Annual Review of Fluid Mechanics* **6** (1974), no. 1 227–255.

[169] R. Bonnecaze and J. Brady, *A method for determining the effective conductivity of dispersions of particles*, *Proceedings of the Royal Society of London. Series A: Mathematical and Physical Sciences* **430** (1990), no. 1879 285–313.

[170] H. Risken, *The fokker-planck equation: methods of solution and applications*, .

[171] W. Coffey and Y. P. Kalmykov, *The Langevin equation: with applications to stochastic problems in physics, chemistry and electrical engineering*, vol. 27. World Scientific, 2012.

[172] J. D. Jackson, *Classical electrodynamics*, 1999.

[173] D. B. Geselowitz, *On bioelectric potentials in an inhomogeneous volume conductor*, *Biophysical journal* **7** (1967), no. 1 1–11.

[174] W. R. Smythe, *Static and dynamic electricity*. International series in pure and applied physics. McGraw-Hill, New York, 3d ed. ed., 1967.

[175] Y. Chiew and E. Glandt, *The effect of structure on the conductivity of a dispersion*, *Journal of colloid and interface science* **94** (1983), no. 1 90–104.

[176] D. Hasselman and L. F. Johnson, *Effective thermal conductivity of composites with interfacial thermal barrier resistance*, *Journal of composite materials* **21** (1987), no. 6 508–515.

[177] Y. C. Chiew and E. D. Glandt, *Effective conductivity of dispersions: the effect of resistance at the particle surfaces*, *Chemical engineering science* **42** (1987), no. 11 2677–2685.

[178] R. O'brien, *A method for the calculation of the effective transport properties of suspensions of interacting particles*, *Journal of Fluid Mechanics* **91** (1979), no. 1 17–39.

[179] J. Dahler and L. Scriven, *Theory of structured continua i. general consideration of angular momentum and polarization*, *Proceedings of the Royal Society of London. Series A. Mathematical and Physical Sciences* **275** (1963), no. 1363 504–527.

[180] G. Russakoff, *A derivation of the macroscopic maxwell equations*, *American Journal of Physics* **38** (1970), no. 10 1188–1195.

[181] J. C. Maxwell, *A treatise on electricity and magnetism*, vol. 1. Clarendon press, 1881.

[182] D. Ross, *The potential due to two point charges each at the centre of a spherical cavity and embedded in a dielectric medium*, *Australian Journal of Physics* **21** (1968), no. 6 817–822.

[183] S.-Y. Lu and J.-L. Song, *Effective conductivity of composites with spherical inclusions: Effect of coating and detachment*, *Journal of applied physics* **79** (1996), no. 2 609–618.

[184] Z. Hashin and S. Shtrikman, *A variational approach to the theory of the effective magnetic permeability of multiphase materials*, *Journal of applied Physics* **33** (1962), no. 10 3125–3131.

[185] P. Langevin, *Sur la théorie du mouvement brownien*, *Compt. Rendus* **146** (1908) 530–533.

[186] E. Nelson, *Dynamical theories of Brownian motion*, vol. 3. Princeton university press, 1967.

[187] H. Takayasu, A.-H. Sato, and M. Takayasu, *Stable infinite variance fluctuations in randomly amplified langevin systems*, *Physical Review Letters* **79** (1997), no. 6 966.

[188] G. Steinbrecher and B. Weyssow, *Extreme anomalous particle transport at the plasma edge*, *Univ. of Craiova/Univ Libre de Bruxells working paper* (2007).

[189] A. Schenzle and H. Brand, *Multiplicative stochastic processes in statistical physics*, *Physical Review A* **20** (1979), no. 4 1628.

[190] R. M. May, S. A. Levin, and G. Sugihara, *Ecology for bankers*, *Nature* **451** (2008), no. 7181 893–894.

[191] W. T. Shaw and M. Schofield, *A model of returns for the post-credit-crunch reality: hybrid brownian motion with price feedback*, *Quantitative Finance* **15** (2015), no. 6 975–998.

[192] J. L. Forman and M. Sørensen, *The pearson diffusions: A class of statistically tractable diffusion processes*, *Scandinavian Journal of Statistics* **35** (2008), no. 3 438–465.

[193] H. Risken, *Fokker-Planck Equation*, pp. 63–95. Springer Berlin Heidelberg, Berlin, Heidelberg, 1996.

[194] H. Hasegawa, *Stationary and dynamical properties of information entropies in nonextensive systems*, *Physical Review E* **77** (2008), no. 3 031133.

[195] H. Hasegawa, *A moment approach to analytic time-dependent solutions of the fokker-planck equation with additive and multiplicative noise*, *arXiv preprint arXiv:0810.0839* (2008).

[196] R. E. Mortensen, *Mathematical problems of modeling stochastic nonlinear dynamic systems*, *Journal of Statistical Physics* **1** (1969), no. 2 271–296.

[197] K. Pearson, *Tables for statisticians and biometricians*. University press, 1914.

[198] S. M. Iacus, *Simulation and inference for stochastic differential equations: with R examples*. Springer Science & Business Media, 2009.

[199] K. Pearson, *X. contributions to the mathematical theory of evolution.?ii. skew variation in homogeneous material*, *Philosophical Transactions of the Royal Society of London.(A.)* (1895), no. 186 343–414.

[200] J. Heinrich, *A guide to the pearson type iv distribution*, .

[201] B. M. Bibby, I. M. Skovgaard, M. Sørensen, *et. al.*, *Diffusion-type models with given marginal distribution and autocorrelation function*, *Bernoulli* **11** (2005), no. 2 191–220.

[202] M. Caputo, *Linear models of dissipation whose q is almost frequency independent?ii*, *Geophysical Journal International* **13** (1967), no. 5 529–539.

[203] R. Gorenflo and F. Mainardi, *Fractional calculus: integral and differential equations of fractional order*, *arXiv preprint arXiv:0805.3823* (2008).

[204] M. A. Matlob and Y. Jamali, *The concepts and applications of fractional order differential calculus in modeling of viscoelastic systems: A primer*, *Critical Reviews? in Biomedical Engineering* **47** (2019), no. 4.

[205] C. Li and F. Zeng, *Finite difference methods for fractional differential equations*, *International Journal of Bifurcation and Chaos* **22** (2012), no. 04 1230014.

[206] Z.-z. Sun and X. Wu, *A fully discrete difference scheme for a diffusion-wave system*, *Applied Numerical Mathematics* **56** (2006), no. 2 193–209.

[207] P. Virtanen, R. Gommers, T. E. Oliphant, M. Haberland, T. Reddy, D. Cournapeau, E. Burovski, P. Peterson, W. Weckesser, J. Bright, S. J. van der Walt, M. Brett, J. Wilson, K. Jarrod Millman, N. Mayorov, A. R. J. Nelson, E. Jones, R. Kern, E. Larson, C. Carey, İ. Polat, Y. Feng, E. W. Moore, J. Vand erPlas, D. Laxalde, J. Perktold, R. Cimrman, I. Henriksen, E. A. Quintero, C. R. Harris, A. M. Archibald, A. H. Ribeiro, F. Pedregosa, P. van Mulbregt, and S. . . Contributors, *SciPy 1.0: Fundamental Algorithms for Scientific Computing in Python*, *Nature Methods* **17** (2020) 261–272.

[208] L. Petzold, *Automatic selection of methods for solving stiff and nonstiff systems of ordinary differential equations*, *SIAM journal on scientific and statistical computing* **4** (1983), no. 1 136–148.

[209] J. R. Macdonald and E. Barsoukov, *Impedance spectroscopy: theory, experiment, and applications*, *History* **1** (2005), no. 8 1–13.

[210] M. E. Orazem and B. Tribollet, *Electrochemical impedance spectroscopy*, *New Jersey* (2008).

[211] N. Bonanos, P. Pissis, and J. R. Macdonald, *Impedance spectroscopy of dielectrics and electronic conductors*, *Characterization of materials* (2002) 1–14.

[212] K. S. Cole and R. F. Baker, *Longitudinal impedance of the squid giant axon*, *The Journal of general physiology* **24** (1941), no. 6 771–788.

[213] D. Klotz, *Negative capacitance or inductive loop?–a general assessment of a common low frequency impedance feature*, *Electrochemistry Communications* **98** (2019) 58–62.

[214] H. Brandstätter, I. Hanzu, and M. Wilkening, *Myth and reality about the origin of inductive loops in impedance spectra of lithium-ion electrodes?a critical experimental approach*, *Electrochimica acta* **207** (2016) 218–223.

[215] S. K. Roy, M. E. Orazem, and B. Tribollet, *Interpretation of low-frequency inductive loops in pem fuel cells*, *Journal of The Electrochemical Society* **154** (2007), no. 12 B1378.

[216] J. Bisquert, G. Garcia-Belmonte, Á. Pitarch, and H. J. Bolink, *Negative capacitance caused by electron injection through interfacial states in organic light-emitting diodes*, *Chemical Physics Letters* **422** (2006), no. 1-3 184–191.

[217] E. Ghahremanirad, A. Bou, S. Olyaee, and J. Bisquert, *Inductive loop in the impedance response of perovskite solar cells explained by surface polarization model*, *The journal of physical chemistry letters* **8** (2017), no. 7 1402–1406.

[218] S. Taibl, G. Fafilek, and J. Fleig, *Impedance spectra of fe-doped srtio 3 thin films upon bias voltage: inductive loops as a trace of ion motion*, *Nanoscale* **8** (2016), no. 29 13954–13966.

[219] J. Dobbelaar and J. De Wit, *Impedance measurements and analysis of the corrosion of chromium*, *Journal of The Electrochemical Society* **137** (1990), no. 7 2038.

[220] K. S. Cole and R. H. Cole, *Dispersion and absorption in dielectrics i. alternating current characteristics*, *The Journal of chemical physics* **9** (1941), no. 4 341–351.

[221] S. Smye, C. Evans, M. Robinson, and B. Sleeman, *Modelling the electrical properties of tissue as a porous medium*, *Physics in Medicine & Biology* **52** (2007), no. 23 7007.

[222] R. Zorn, *Logarithmic moments of relaxation time distributions*, *The Journal of chemical physics* **116** (2002), no. 8 3204–3209.

[223] Y. SUGIURA, S. KOGA, and H. AKABORI, *Dielectric behavior of yeast cells in suspension*, *The Journal of General and Applied Microbiology* **10** (1964), no. 2 163–174.

[224] K. Asami, T. Hanai, and N. Koizumi, *Dielectric properties of yeast cells*, *The Journal of membrane biology* **28** (1976), no. 1 169–180.

[225] H. Fricke, H. P. Schwan, K. Li, and V. Bryson, *A dielectric study of the low-conductance surface membrane in e. coli*, *Nature* **177** (1956), no. 4499 134–135.

[226] A. Irimajiri, T. Hanai, and A. Inouye, *Dielectric properties of synaptosomes isolated from rat brain cortex*, *Biophysics of structure and mechanism* **1** (1975), no. 4 273–283.

[227] H. Pauly, L. Packer, and H. Schwan, *Electrical properties of mitochondrial membranes*, *The Journal of biophysical and biochemical cytology* **7** (1960), no. 4 589.

[228] E. Carstensen and R. Marquis, *Passive electrical properties of microorganisms: Iii. conductivity of isolated bacterial cell walls*, *Biophysical journal* **8** (1968), no. 5 536–548.

[229] T. Hanai and K. Sekine, *Theory of dielectric relaxations due to the interfacial polarization for two-component suspensions of spheres*, *Colloid and Polymer Science* **264** (1986), no. 10 888–895.

[230] T. Hanai, H. Zhang, K. Sekine, K. Asaka, and K. Asami, *The number of interfaces and the associated dielectric relaxations in heterogeneous systems*, *Ferroelectrics* **86** (1988), no. 1 191–204.